MICROSTRUCTURE-SENSITIVE PLASTICITY AND FATIGUE OF THREE TITANIUM ALLOY MICROSTRUCTURES

A Thesis
Presented to
The Academic Faculty

by

Benjamin Daniel Smith

In Partial Fulfillment
of the Requirements for the Degree
Master of Science in the
School of Mechanical Engineering

Georgia Institute of Technology
August 2013

MICROSTRUCTURE-SENSITIVE PLASTICITY AND FATIGUE OF THREE TITANIUM ALLOY MICROSTRUCTURES

Approved by:

Dr. David L. McDowell, Advisor
School of Mechanical Engineering
Georgia Institute of Technology

Dr. Richard Neu
School of Mechanical Engineering
Georgia Institute of Technology

Dr. Olivier Pierron
School of Mechanical Engineering
Georgia Institute of Technology

Dr. Donald Shih
Boeing Research & Technology
The Boeing Company

Date Approved: 6/10/13

"Of all the knowledge that we can ever obtain, the knowledge of God, and the knowledge of ourselves, are the most important."
Jonathon Edwards, 1762

ACKNOWLEDGEMENTS

I would like to begin by expressing my deepest gratitude to my graduate advisor, Dr. David McDowell, for his patience and guidance during the completion of this work. His expertise has proved invaluable in numerous situations throughout this research. I would also like to extend thanks to my reading committee, Dr. Richard Neu, Dr. Olivier Pierron, and Dr. Donald Shih.

I am extremely grateful for the direction and support of Dr. Donald Shih, who was very generous in facilitating assistantship funding from the Boeing Company. Dr. Shih's excitement for materials modeling and development is inspiring. I would also like to thank the Carter N. Paden Chair in Metals Processing at Georgia Tech for providing additional funding support.

I am heavily indebted to my companions within the McDowell research group, who served as both mentors and friends throughout my time here. My daily interactions with Matthew Priddy, Jeff Lloyd, Brett Ellis, Bill Musinski, Anirban Patra, Shuozhi Xu, and Dr. Jagan Padbidri were vital to the progress and success of this work. I have been very fortunate to have worked with such talented colleagues and I will miss their company. In addition, I am obliged to Michael Kirka for his patience and training on the experimental testing equipment, as well as Jin Song for providing instruction on crystal plasticity model calibration.

Finally, I would like to thank my family; especially my father, Daniel, and mother, Debbie, as well as my brothers (Caleb, Aaron, and Seth), sisters (Hannah and Miriam), and extended family (Perstropes and Smiths) for their love, patience, support,

and prayer. Of all these things, I am most thankful for their prayers. I recognize that I have been given a unique opportunity, particularly as a master's student, to work on an exciting project with a brilliant advisor while benefiting from the support of an assistantship and very helpful friends. The alignment of such things is completely out of my control and I believe that it is largely on account of my family's prayers that this time at Georgia Tech has worked for my good.

TABLE OF CONTENTS

LIST OF TABLES

Page

LIST OF FIGURES

Page

SUMMARY

Titanium alloys are employed in many advanced engineering applications due to their exceptional properties, i.e., a high strength-to-weight ratio, corrosion resistance, and high temperature strength. The performance of titanium alloys is known to be strongly affected by its inherent microstructure, which forms as a result of thermo-mechanical processing. Depending on the alloying composition and processing route, the produced microstructure can exhibit a combination of extremely diverse morphologies. These variant microstructures produce compromise relationships between beneficial and detrimental effects on the alloy's performance. To study these structure-property relationships, two distinct crystal plasticity algorithms have been calibrated to data acquired from cyclic deformation experiments performed on three distinct titanium microstructures. The calibrated models were then utilized to simulate fatigue loading behavior of variant microstructures of each material to investigate the influence of mean grain size, crystallographic texture, and phase volume fraction. Fatigue damage has been quantified through the calculation of fatigue indicator parameters (FIPs) and radial correlation functions are employed to study the spatial correlation between favorably oriented slip systems and the extreme value FIP locations. The computed results are fit to extreme value statistical distributions to observe trends in the fatigue performance associated with alterations to key microstructural attributes.

CHAPTER 1

INTRODUCTION

Introduction

The performance of titanium alloys is known to be highly dependent on its microstructure induced by thermo-mechanical processing. This structure-dependence leads to a wide range of potential properties caused by any combination of very diverse microstructure morphologies. This span of achievable properties warrants their optimization to individual situations. It is possible to identify an ideal microstructure for a specific application through extensive experimental investigation, however, the time and costs associated with these studies can be prohibitively large, particularly when characterizing fatigue properties. To reduce the time and expense of alloy development, it is possible to employ crystal plasticity finite element simulations to analyze the structure-property trends of the material. These simulations are not intended to replace experimental work, rather they provide additional insight into the physical mechanisms leading to property generation which will inform the material design process and effectively reduce the required number of experiments necessary to identify an ideal microstructure and processing route. The objective of this current research is to calibrate titanium crystal plasticity constitutive frameworks to cyclic deformation experimental results and then utilize the calibrated models to study the microstructure-sensitive fatigue performance trends related to variant microstructures of two different alloys: Ti-6Al-4V and Ti-18. The simulated finite element geometries aim to incorporate the effects of grain size, crystallographic texture, and phase distribution.

Scope of Thesis

This thesis is an extension of previous work on crystal plasticity modeling of titanium alloys within McDowell's research group (Mayeur and McDowell, 2007; Przybyla, 2010; Przybyla and McDowell, 2011; Zhang, 2008). The current work primarily builds off of the efforts of Przybyla (2010), who utilized the crystal plasticity model developed by Mayeur (2004) to study the fatigue performance trends of duplex alpha-beta titanium microstructures possessing differing grain sizes and phase volume fractions. During this previous research, Przybyla laid the ground work for studying simulated fatigue of titanium with the creation of his microstructure generation suite as well as his utilization of extreme value fatigue statistics to describe the simulated distributions of maximum fatigue indicator parameters. This current thesis extends these previously generated tools for application to the fully lamellar, a.k.a. Widmanstätten, microstructures of beta-annealed titanium alloys. A new crystal plasticity framework coded by Britt et al. (2011) is employed in this study in conjunction with the previously created crystal plasticity model. The material parameters in both models have been estimated to gain agreement with experimental stress-strain data generated for the beta-annealed structures. Simulated fatigue studies were also advanced to include texture effects as well as the calculation of additional FIPs.

Thesis Outline

A general background of metal fatigue is presented In Chapter 2. Initially, the history of research advances in fatigue is briefly discussed, followed by a description of the physical mechanisms leading to fatigue crack initiation and growth. Afterward, widely employed engineering models for fatigue life estimation are described. Critical plane approaches are then introduced and commonly utilized damage parameters and fatigue indicator parameters are discussed.

In Chapter 3, the calibration of the crystal plasticity frameworks is described. Characterization of the selected materials is presented along with the experimental procedures and results utilized as a basis of calibration. The kinematics and kinetics of the crystal plasticity models are outlined and the parameters of both models are estimated to gain good agreement with the experimental results for each of the microstructures. An explanation of the individual microstructure representations as well as the calibration process is also discussed.

Chapter 4 includes the simulated fatigue study of the two fully lamellar microstructures investigated. The computed fatigue indicator parameters are introduced, followed by a brief description of the Gumbel extreme value distribution and radial correlation function. Statistical volume generation methods for fitting mean grain size, crystallographic texture, phase volume fraction, and disorientation distribution are outlined. The generated extreme value FIP distributions and radial correlation results are then discussed.

The simulated fatigue study of the Ti-18 STA (duplex) structure is discussed in Chapter 5. A brief review of observed microtextured regions in titanium alloys is presented, which is then followed by a description of the fatigue indicator parameters calculated. The methodology behind finite element geometry instantiation is presented and the simulation results for fatigue dependence on texture band orientation are then discussed.

Finally, the outcomes of the present work are summarized in Chapter 6. These concluding remarks are supplemented with recommendations for future work to gain more accurate estimation of material parameters and perform additional experiments.

CHAPTER 2

FATIGUE OF METALS

Introduction

Fatigue is a process of mechanical failure originating from repeated loading. This recurring load is typically well below the material yield strength and can lead to failures as trivial as broken door handles or as catastrophic as an airplane crash. Fatigue has been estimated to be the source of 50 - 90% of all mechanical failures (Stephens et al., 2000) and the total cost of these failures has been projected to be as large as 4% of the United States GDP by previous researchers (Reed et al., 1983). With such substantial consequences in costs and public safety, it is imperative that design engineers employ established methods to account for fatigue life of critical components to avoid potentially disastrous events. This chapter presents a brief overview of the history of fatigue, physical mechanisms leading to fatigue failure, as well as engineering models and methods utilized to inform fatigue design.

History of Fatigue

The term "fatigue" is often attributed to Poncelet (1839), who described metals as becoming "tired" during their use. In the middle of the 19^{th} century, many unexpected failures of steel structures were observed, particularly in train axels and bridges. These unexplained events led to an increasing interest in the root cause of fatigue failures with hopes of explaining their source and preventing their future repetition. Wöhler (1860) performed the first methodical fatigue experiments while he was investigating the fracture behavior of train axels for a railway company. He cyclically loaded his material at various stress amplitudes and observed that the number of cycles that the material

could sustain would decrease with rising stresses amplitudes. This significant finding shaped the concept of the stress-life (S-N) curve as a design tool, which is still often utilized today for engineering applications. Wöhler also noted during his studies that there appeared to be a stress amplitude threshold below which fracture would not occur. This threshold stress amplitude was identified to be the fatigue endurance limit where the typical life was in excess of over one million cycles, i.e., "infinite" cycle life. Afterward, Gerber (1874) and Goodman (1899) extended Wöhler's work to incorporate mean stress effects into the fatigue endurance limit calculation. Basquin (1910) later determined that the stress-life data within the finite life regime could be approximated by a linear relationship on a log-log scale, i.e., a power law relation between stress amplitude and cycle life. This model allowed for the estimation of cycle lives associated with stress amplitudes exceeding the fatigue endurance limit.

At the end of the 19th century, engineers were aware of fatigue failures and had developed stress-based phenomenological models to inform their designs; however, the mechanism inducing these failures remained a mystery. Ewing and Humfrey (1903) were the first to utilize an optical microscope to observe the source of fatigue crack nucleation. They stressed iron bars in reversed bending and interrupted the experiments after increments in the number of cycles to study the microstructure evolution. Ewing and Humfrey found that localized slip lines appeared in the structure and would eventually grow to form a crack, despite the applied stress being considerably smaller than the Young's modulus. This result was crucial for guiding future research in crack formation and modeling. In accordance with these observations, Coffin (1954) and Manson (1954) independently proposed that fatigue life models should be related to the plastic strain amplitude in a similar form as the Basquin equation. This Coffin-Manson relationship has been widely utilized in industry to relate the strain amplitude and cycle life (Suresh, 1992).

Advances in the study of fracture mechanics began when Griffith (1921) proposed an energy criterion for crack initiation and growth during his work with brittle solids. He suggested that cracks can form or experience further propagation iff the energy of the system is either decreasing or held constant in the event of crack nucleation or incremental extension. In his framework, Griffith recruited the mathematical forms of Inglis (1913) to determine the strain energy associated with an elliptical vacancy within a plate to determine the stresses necessary to extend a crack. The derived results were found to be accurate for brittle materials, yet they underestimate the strength of metals which experience additional energy dissipation through plasticity.

Research in fracture mechanics saw dramatic growth after the events of World War II. WWII marked a time of rapid manufacturing of ships, tanks, and airplanes experiencing very short product lives. The creation of these vehicles required designs tailored for simple fabrication processes and utilized relatively inexpensive materials. On occasion, these designs were found to contain serious flaws that led to catastrophic failures. A well-known example of an inferior fracture-resistant design is that of the Liberty ships (Williams and Ellinger, 1953). The innovative welding design of the Liberty hulls allowed for their swift production, however, the welds were positioned in such a way that cracks could propagate across large portions of the ship's hull with very little resistance. In addition, these welds were performed at relatively high speeds which would frequently produce large crack-like defects. This calamitous combination resulted in significantly increased failure rates of the manufactured Liberty ships with many of them splitting completely into two parts. The performance of the Liberty ships highlighted the importance of incorporating fracture resiliency into engineering designs.

Shortly after the war, Irwin (1948) and Orowan (1948) simultaneously modified the Griffith energy theory to include both elastic and plastic strain energy, which extended the theory to application of metals. Irwin (1956) employed the modified Griffith theory to create the notion of the "energy release rate". This energy release rate is defined

as the calculated change in the potential energy with respect to a corresponding increment of crack growth. When the energy release rate is greater than some critical value, the crack can be expected to extend. Irwin (1957) then applied stress field calculations from Westergaard (1939) and showed that the stresses near the crack tip can be described with the "stress intensity factor", which is related to the energy release rate. These theories developed by Irwin are at the core of linear elastic fracture mechanics (LEFM) and have proven to be effective for many engineering applications.

Though LEFM is extremely useful, its validity breaks down when the material exhibits a sizeable plastic zone at the crack tip. To account for larger plastic zones, Rice (1968) derived a nonlinear energy release rate calculation through his idea of the path-independent J-integral, which now forms the basis of elastic-plastic fracture mechanics (EPFM). The nonlinear energy release rate, J, is a generalized measure of the energy release rate, G, and it accounts for the added plastic strain energy dissipated into the material during crack extension. The J-integral was initially validated by Begley and Landes (1972) when they showed that J_{IC} was accurate in describing the fracture behavior of tough pressure vessel steels used in the nuclear industry. Begley and Landes also determined that J closely agreed with G for linear elastic materials, as the theory of the J-integral suggests. Since then, EPFM has been widely employed in industry to characterize the fracture mechanics of materials exhibiting too much plasticity for LEFM analysis.

Fatigue Crack Nucleation

Fatigue crack initiation is induced by a process of damage accumulation accrued through inelastic deformation. Both the formation of cracks and microstructurally short crack growth are dominated by similar physical mechanisms. This early stage of fatigue has been labeled "stage 1" crack growth by Forsyth (1962) and it is governed by the activity of localized crystallographic slip. Ever since the metallographic work of Ewing

and Humfrey (1903), it has been well known that cracks often occur along slip planes that experience severe plasticity. These slip planes are frequently found to move in bands of parallel motion dubbed “persistent slip bands” by Thompson et al. (1956). The plastic slip at the surface of the material is of utmost importance as it is typically the site of crack nucleation. Forsyth (1953) was the first to discover that plasticity produced a roughening effect at the metal’s surface. The roughened surface was found to possess extrusions of slip planes which protrude from the fatigued specimen’s surface as well as intrusions of receding slip planes creating small valleys or pits (Cottrell and Hull, 1957; Forsyth and Stubbington, 1955). The jagged surface created by the intrusions and extrusions replicates multiple micro-notch features and induces stress intensification. The combination of localized stress and strain cooperatively works to damage the metal and initiate a crack. A schematic of how a fatigue crack can nucleate at an inclusion-extrusion roughened surface can be seen in Figure 2.1. Impressive scanning electron microscopy of surface cracks at persistent slip bands can be referenced in Ma and Laird's (1989) work. The fatigue cracking sensitivity to surface discontinuities suggests that smooth, polished faces are ideal for extending fatigue life. The significance of the surface finish has been summarized in the machine design text of Juvinall and Marshek (1991), which shows that the fatigue strength of steels is reduced by at least 20% for un-polished specimens when compared to ideal mirror-polished specimens.

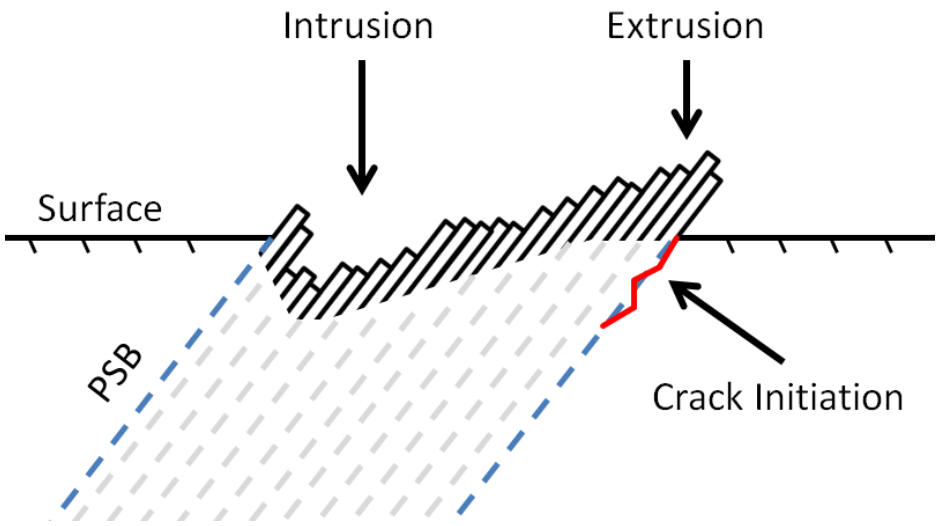

Figure 2.1. Schematic of persistent slip band (PSB) induced crack initiation of a fatigued metal.

In many engineering materials, defects introduced during the thermo-mechanical processing are the primary source of crack formation. Common flaws include voids, impurities, and inclusions. When one of these is present, it creates a discontinuity in the material matrix and acts as a stress concentrator which will compete with the surface for the crack initiation site. The mechanism of crack formation associated with inclusions is strongly dependent on the slip behavior of the matrix, the strength of the matrix-inclusion interface, and the relative strengths of the matrix and inclusion. In high strength steels, a frequent form of cracking is a consequence of decohesion between a non-metallic inclusion and the matrix (Lankford and Kusenberger, 1973). During fatigue loading, the softer steel matrix begins to deform and pull on the inclusion. Due to the relatively weak adhesive strength, the inclusions begin to debond from the matrix creating an interfacial crack which eventually propagates through the matrix to a critical size. It is also possible for the inclusion debonding to form clusters of voids which swell and coalesce to form larger cracks. In addition to debonding, cracks can form as a result of slip impinging upon the inclusions or defects, which was observed in a fatigued 2024-T4 Al alloy by Kung and Fine (1979). In some circumstances, the inclusions themselves have been

found to crack. In these instances, the bonding strength of the matrix-inclusion boundary has higher strength than the embedded inclusion. For example, inclusion cracking has been frequently observed in particle-reinforced metal-matrix composites, e.g., SiC particle fracture in a reinforced 6061 aluminum alloy (Lloyd, 1991). In all possible cases of inclusion or defect induced failures, the size and amount of the flaws are critical in limiting fatigue life with larger sizes leading to lower cycle lives. A summary of inclusion failure modes is provided in Figure 2.2.

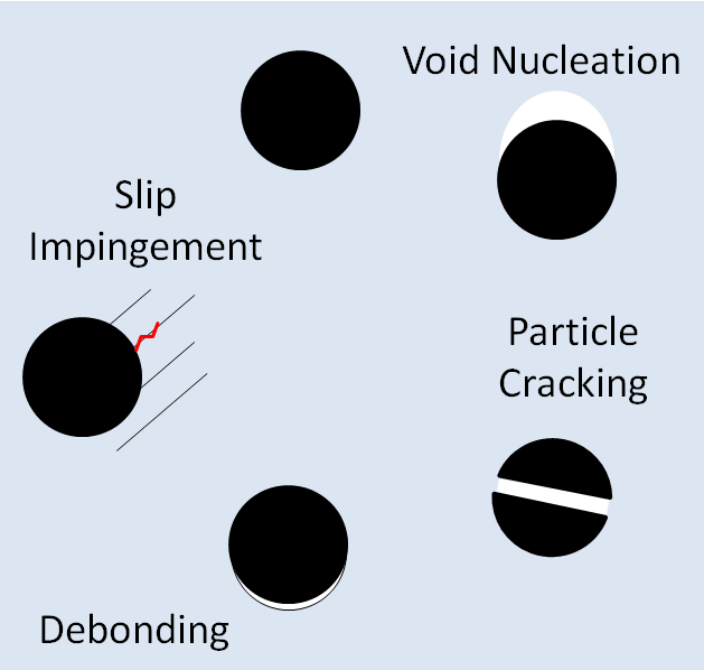

Figure 2.2. Summary of inclusion crack initiation mechanisms

Fatigue Crack Growth

After the fatigue crack has been initiated, the initial stages of propagation are directed by local shear slip planes. This later process of stage 1 growth is very sensitive to the microstructure with crack extension being strongly affected by the grain boundaries (Tanaka and Akiniwa, 1989). Eventually, the cracks grow longer than the characteristic scale of the microstructure and begin to propagate normal to the maximum applied stress. This regime of stable crack growth is less sensitive to the microstructural features (Miller, 1993) and has been termed “stage II” crack growth (Forsyth, 1962), see Figure 2.3. It is

in this period of crack extension that several materials exhibit fatigue's signature striation marks, discovered by Zapffe and Worden (1951). The striation marks present themselves on the fracture surface and appear similar to waves rippling out from the crack initiation site. Each of the striation waves is correlated with a single loading cycle. Forsyth and Ryder (1960) showed that the spacing between the individual striations was directly related to the average observed crack growth rate. Laird (1967) proposed a crack-tip blunting model to describe the process of striation formation. In this concept, the source of striation generation is the repeated activity of crack tip plastic blunting followed by crack-tip sharpening upon loading reversal. This blunting model is applicable to a wide set of materials. The primary exception is the striation formation in ductile single crystals, which have been observed to be produced by an alternating slip plane mechanism (Neumann, 1969).

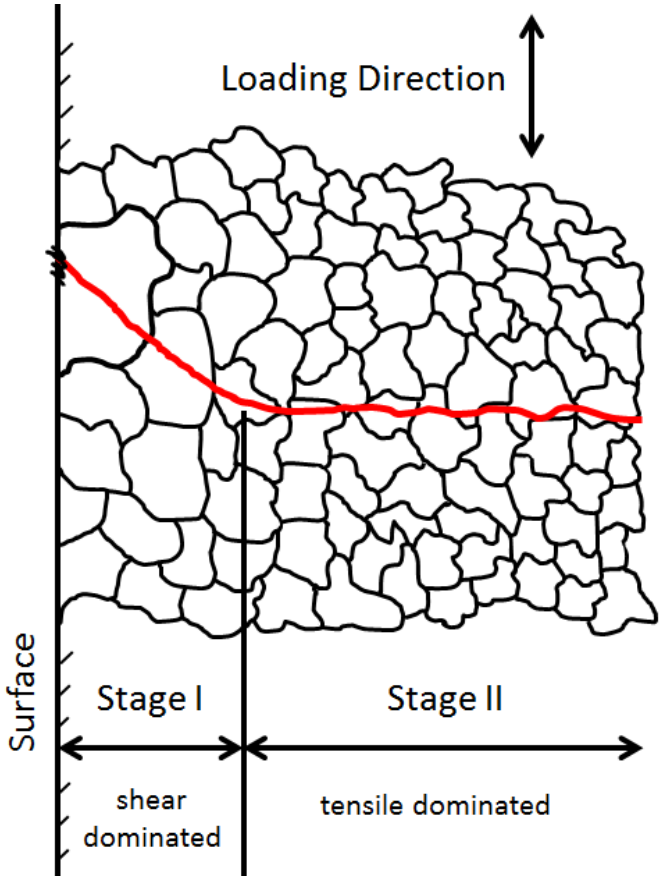

Figure 2.3. Two stage approach to fatigue crack growth (Forsyth, 1962). Adapted from (Stephens et al., 2000).

Paris et al. (1961) utilized Irwin's (1957) stress intensity factor $\left(K = Y\sigma\sqrt{\pi a}\right)$ for static crack growth and extended the concept to describe crack extension caused by cyclic loading. They postulated that the incremental crack growth rate should be a function of the stress intensity factor range determined from the calculation of the stress intensity factor at the minimum and maximum loads of the cycle. Shortly thereafter, Paris and Erdogan (1963) investigated fatigue crack propagation data for a broad range of airframe material and determined that the crack growth rate and stress intensity factor range followed a power law relation, i.e.,

$$\frac{da}{dN} = C\left(\Delta K\right)^m. \tag{2.1}$$

where da/dN is the crack growth rate, ΔK is the stress intensity factor range, and both C and m are constants. This "Paris Law" is an extremely useful model for estimating the remaining fatigue life of a cracked component. It has been successfully exploited on a wide variety of materials and industrial applications on account of its simplicity and accuracy.

Phenomenological Models for Cycle Life Estimation

A key objective in studying fatigue is to gain a reliable method of cycle life estimation. Accurate cycle life forecasting is critical for the design of engineering systems to ensure both safety and reduction of unnecessary replacement costs. The initial empirical models developed for projecting fatigue life were based on stress. Wöhler (1860) established the use of the stress-life (S-N) diagram as an initial tool in life estimation. The S-N curve is constructed by performing numerous fatigue experiments at various fully-reversed stress amplitudes and recording the number of cycles to failure. Wöhler observed a "knee" in the S-N curve for which steel materials sustained over a million cycles and seemed to possess an infinite cycle life. This minimum stress

amplitude became known as the fatigue endurance limit. Gerber (1874) and Goodman (1899) advanced the concept of the fatigue endurance limit to applications incorporating mean stress effects. The Gerber and Goodman formulations are displayed in Equations 2.2 and 2.3, respectively.

$$\frac{\sigma_a}{\sigma_f}+\left(\frac{\sigma_m}{\sigma_u}\right)^2=1 \tag{2.2}$$

$$\frac{\sigma_a}{\sigma_f}+\frac{\sigma_m}{\sigma_u}=1 \tag{2.3}$$

Here σ_a is the stress amplitude, σ_f is the fatigue endurance limit for fully-reversed loading, σ_u is the ultimate tensile strength, and σ_m is the mean stress. These formulations could be used to estimate possible mean stress and stress amplitude for infinite lives, yet they do not provide any estimation of the cycle life associated with applied stresses that exceed the endurance limit. Basquin (1910) extended these models for applicability to reduced cycle lives by approximating the S-N curve as a power law relation within the finite life region, i.e.,

$$\sigma_{N_f}=A\left(N_f\right)^B. \tag{2.4}$$

here σ_{N_f} represents the finite cycle life strength, N_f is the number of cycles to failure, and both A and B are constants determined from σ_f and σ_u. The finite cycle life strength simply replaces the fatigue endurance limit in Equations 2.2 and 2.3 to use them for the desired cycle life.

Strain-based phenomenological models began to be used after Coffin (1954) and Manson (1954) observed a linear relationship between the plastic strain amplitude

($\Delta\varepsilon_p / 2$) and number of load reversals ($2N_f$) on a log-log plot. The decay shaped strain-life curve was then assumed to be composed of the sum of two linear lines so that both the plastic strain amplitude and elastic strain amplitude could be written as power law relations with the number of load reversals. The total strain amplitude is then related to the number of load reversals through the following expression:

$$\frac{\Delta\varepsilon}{2} = \frac{\sigma_f^{'}}{E}\left(2N_f\right)^b + \varepsilon_f^{'}\left(2N_f\right)^c \ . \tag{2.5}$$

Here, $\sigma_f^{'}$ and b are the fatigue strength coefficient and strength exponent; $\varepsilon_f^{'}$ and c are the ductility coefficient and ductility exponent; E is the modulus of elasticity; and $2N_f$ is the number of load reversals. The left and right terms on the right-hand side of the equation represent the elastic and plastic strain amplitudes, respectively. The constants in Equation 2.5 can be determined by generating a strain-life curve from numerous experimental results.

Fatigue Indicator Parameters

The previously outlined phenomenological models have proven extremely valuable for cycle life estimation within the low cycle fatigue (LCF) regime, where $N_f < 10^6$ cycles. In contrast, their direct application to the lower stress amplitudes of high cycle fatigue (HCF) and very high cycle fatigue (VHCF) have not been as successful (McDowell, 1996). Phenomenological model inaccuracy in these regimes is rooted in their insensitivity to the mechanisms associated with the process of crack nucleation and micro-crack growth, i.e., stage I growth (Forsyth, 1962), which consumes an overwhelming majority of the HCF cycle life. A key indicator of their imprecision is the relatively large amounts of scatter typically present in HCF data. The source of this scatter has been suggested to be from microstructural effects which cause localized

damage extremities and lead to fatigue cracking (McDowell, 1996). This supposition is justified since stage I growth is induced by highly heterogeneous cyclic plasticity, which is highly sensitive to the microstructure morphology. Therefore, it is imperative for HCF models to incorporate the damage mechanisms affecting stage I growth to more accurately predict cycle lives.

Several life prediction models have been proposed in an attempt to more accurately capture the micro-crack initiation and early growth phases. These frameworks can be categorized by their basis on three different approaches: stress, energy, and critical planes. The first models, based on stress, were essentially extensions of classical yield criteria, i.e., Tresca's maximum shear stress theory and von Mises' octahedral shear theory. These concepts were utilized with marginal success, yet they have been largely abandoned due to their insensitivity to hydrostatic stresses in addition to their failure to predict fatigue lives associated with complex loading. Energy based methods have also been suggested to forecast crack initiation, e.g., utilizing plastic work calculations. However, Fatemi and Socie (1988) contend that energy parameters are inadequate for describing crack formation since they are scalar in nature and are thus unable to quantify directional damage features. Finally, critical plane approaches have been developed which investigate the stress-strain state on potential cracking planes. These critical plane models appear to be the most promising for predicting trends in fatigue life.

The critical plane models consist of damage parameters (DP) which quantify the damage imposed onto critical planes. The plane possessing the maximum calculated parameter is assumed to be the initial cracking plane. These parameters can be determined from either a stress-based or strain-based method. An example stress-based damage parameter is the Findley parameter (Findley, 1959):

$$DP_F = \frac{\Delta\tau_{\max}}{2} + k\sigma_{\max}^{n} \tag{2.6}$$

Here, $\Delta\tau_{\max}/2$ is the maximum shear stress amplitude, k is a constant denoting sensitivity to the normal stress, and $\sigma^{n}_{\max}$ is the stress normal to the max shear stress amplitude plane. Strain-based critical plane approaches are utilized more often since it is well known that fatigue crack initiation is associated with plastic strain. An early strain-based measure of fatigue damage is the Smith-Watson-Topper parameter (SWT) (Smith et al., 1970):

$$DP_{SWT} = \frac{\Delta\varepsilon^{p}_{\max}}{2}\sigma^{n}_{\max} \tag{2.7}$$

In the SWT parameter, $\Delta\varepsilon^{p}_{\max}/2$ represents the maximum plastic strain range and $\sigma^{n}_{\max}$ is the stress normal to this plane. Later, Brown and Miller (1973) altered Findley's parameter so that the calculated value was solely based on strain, i.e.,

$$DP_{MB} = \frac{\Delta\gamma_{\max}}{2} + s\Delta\varepsilon^{n}_{\max} \tag{2.8}$$

Where $\Delta\gamma_{\max}/2$ is the maximum shear strain amplitude, s is a constant, and $\Delta\varepsilon^{n}_{\max}$ is the maximum normal strain range on the investigated plane. Fatemi and Socie (1988) investigated the effectiveness of the Miller-Brown (MB) parameter for predicting the fatigue life of 1045 steel. They concluded that the Miller-Brown parameter was acceptably accurate for the life prediction of in-phase biaxial loading, yet was not conservative enough when calculating fatigue lives for non-proportional loading scenarios. This over-estimation of the cycle life for out-of-phase loading was believed to be caused by the MB parameter's insensitivity to the stress, which exhibited additional hardening for non-proportional loading. Fatemi and Socie then proposed a modified Miller-Brown parameter which incorporated the stress effects: the Fatemi-Socie parameter (FSP) (Fatemi and Kurath, 1988; Fatemi and Socie, 1988).

$$DP_{FS} = \frac{\Delta\gamma^{p}_{\max}}{2}\left(1 + K\frac{\sigma^{n}_{\max}}{\sigma_{y}}\right). \tag{2.9}$$

Here, $\Delta\gamma^{p}_{\max}/2$ is the maximum plastic shear strain range, K is a material parameter describing stress sensitivity, $\sigma^{n}_{\max}$ is the normal stress to the $\Delta\gamma^{p}_{\max}$ plane at maximum load, and σ_{y} is the yield strength. The Fatemi-Socie parameter is one of the most widely utilized critical plane approach models. McDowell and Berard (1992) studied the accuracy of critical plane models in predicting the cycle life for Inconel 718 and 1045 steel. They determined that the Fatemi-Socie method produced reasonable results for predicting fatigue life, particularly in the LCF regime. Park and Nelson (2000) research included both the Findley and the Fatemi-Socie parameters. They found that the Findley parameter expressed good correlation with HCF data acquired for numerous steels in diverse loading configurations; the Fatemi-Socie parameter was revealed to possess excellent agreement with fatigue life results in low cycle fatigue for a wide range of steels experiencing complex loading. Gallagher et al. (2004) conducted HCF experiments on Nickel-base superalloy single crystals (PWA 1484) and employed several critical plane approach models to relate to the fatigue life, including the Fatemi-Socie and Findley methods. All of these models were found to express significantly improved correlations for the fatigue life when compared to the classical stress-life (S-N) curve prediction.

It is important to note that these damage parameter studies were originally employed on data collected at a macroscopic scale. However, the damage processes leading to crack formation and HCF life variation are extremely sensitive to the microstructure (micro-scale); therefore, the damage parameters should ideally be determined over non-local averaging volumes at the scale of key microstructural features, e.g., grain sizes. When the damage parameters are applied at the microstructural level,

they are labeled “Fatigue Indicator Parameters” (FIPs, shown as P). While it is experimentally impractical to calculate micro-scale damage parameters, finite element simulations (FEM) coupled with crystal plasticity algorithms display promising potential for the evaluation of structure-property trends (McDowell and Olson, 2008; McDowell, 2007; Przybyla et al., 2012). The scale of the FIP calculations allows for new or modified parameters to be created that incorporate the local damage physics. On account of the Fatemi-Socie parameter’s success in forecasting fatigue life in a macroscopic sense, it has also been directly applied as a FIP:

$$P_{FS} = \frac{\Delta\gamma^{p*}_{\max}}{2}\left(1 + K\frac{\sigma^{n*}_{\max}}{\sigma_y}\right), \tag{2.10}$$

where $\Delta\gamma^{p*}_{\max}/2$ is the maximum plastic shear strain range averaged over a finite volume (as denoted with an asterisk) and $\sigma^{n*}_{\max}$ is the stress normal to the $\Delta\gamma^{p*}_{\max}$ plane for the same volume. This FIP has been utilized by Przybyla and McDowell (2011) to simulate the fatigue life dependence on the grain size and phase volume fraction of a duplex Ti-6Al-4V microstructure. A modification to the Fatemi-Socie FIP has been proposed by McDowell (2007) to model the crack formation induced by the progressive pile-up of dislocations at a grain boundary interface, i.e., a Zener mechanism (Hollomon and Zener, 1946). In this study, the FIP is termed the grain boundary impingement FIP:

$$P_{IMP} = \gamma^{p*}_{net}\left(1 + K\frac{\sigma^{n*}_{GB}}{\sigma_y}\right). \tag{2.11}$$

Here, γ^{p*}_{net} is the maximum net plastic shear strain on a plane impinging on a grain boundary and σ^{n*}_{GB} is the stress normal to the grain boundary interface. Both the Fatemi-Socie FIP and the grain boundary impingement FIP are applicable to a very wide set of materials, yet on occasion it may be beneficial to create new FIPs that are tailored to

capture the frequently observed fracture mechanisms specific to the investigated material. For example, a lamellar decohesion FIP has been proposed by Zhang (2008) to determine the likelihood of a micro-crack occurring at the α/β interface within lamellar grains of a duplex Ti-64 microstructure. This lamellar FIP is also an adaptation of the Fatemi-Socie FIP, i.e.,

$$P_{lamellar} = \frac{\Delta\gamma_{lam}^{p^*}}{2}\left(1 + K\frac{\sigma_{lam}^{n^*}}{\sigma_y}\right) \tag{2.12}$$

where $\Delta\gamma_{lam}^{p^*}/2$ is the plastic shear strain range resolved onto the lamellar interface and $\sigma_{lam}^{n^*}$ is the stress normal to the α/β layer. All three of the mentioned FIPs are utilized in this work to investigate the fatigue performance of variant titanium microstructures, which will be discussed in Chapter 4.

Statistical Measures of Fatigue

Scatter in fatigue data is produced from a combined contribution of life-limiting effects, e.g., variation in the material, applied loading, and manufacturing processes. Due to these variations, it is impossible to completely eliminate the possibility of premature failure due to fatigue damage. However, engineers have been able to successfully utilize empirically based statistical methods to ensure that the probability of failure in their designs is sufficiently small, typically 1% or less. Of these empirical statistical distributions, the most widely utilized framework is the Weibull (1939) distribution, which can be expressed as the following:

$$P = 1 - \exp\left[-\left(\frac{\sigma_f}{\sigma_0}\right)^{m_w}\right] \tag{2.13}$$

where P is the fraction of specimens that will fail below the applied stress amplitude (σ_f), σ_0 is the reference stress, and m_w is the Weibull modulus. The parameters in 2.13 can be determined from a large set of experimental fatigue data; m_w is the slope of the linearized plot and σ_0 is the strength value at which 63.2% of the experiments are expected to have failed.

The fatigue failure of engineering materials is an extreme phenomenon that is initialized by local hot spots within the microstructure. Extreme value statistics Gumbel (1958) can be employed to describe the behavior of the maximum values of numerous sets of data, e.g., maximum calculated FIP values from multiple FEM simulations (Prasannavenkatesan et al., 2011; Przybyla and McDowell, 2010). There are three possible single variable extreme value distributions that are non-degenerate: (1) Gumbel (Type I), (2) Fréchet (Type II), and (3) Weibull (Type III). Ideally, the maximum values of the data sets would fit to one of these distributions so that the characteristics of the data could be better understood. These distributions can be expressed as the following (Haldar, 2000):

$$F_{Y_n}^{I}\left(y_n\right) = \exp\left[-e^{\alpha_n\left(y_n - u_n\right)}\right] \tag{2.14}$$

$$F_{Y_n}^{II}\left(y_n\right) = \exp\left[-\left(\frac{\nu_n}{y_n}\right)^k\right] \tag{2.15}$$

$$F_{Y_n}^{III}\left(y_n\right) = \exp\left[-\left(\frac{\omega - y_n}{\omega - w_n}\right)^k\right] \tag{2.16}$$

Here, $F_{Y_n}\left(y_n\right)$ is the probability that the maximum value of a particular data set, Y_n, is less than or equal to some critical value y_n. In the Gumbel distribution (Eq. 2.14), α_n is a

measure of dispersion and u_n is the characteristic largest value while k is a measure of dispersion and ν_n is the characteristic value in the Fréchet distribution (Eq. 2.15). For the Weibull distribution, k is a shape parameter or measure of dispersion and w_n is the characteristic largest value; ω is the upper-bound of the initial distribution, where $F(\omega)=1$.

The selection of the extreme value model should be based on the distribution's ability to fit to the data. The utilization of the Weibull extreme value distribution in this study has been inhibited by its requirement to specify an upper bound to the data. Currently there is no clearly established method for identifying the proper value of this upper bound. Przybyla and McDowell (2011) investigated the effectiveness of both the Gumbel and Fréchet distributions for describing the extreme value FIP data acquired from several fatigue simulations of variant Ti-64 microstructure statistics. They concluded that the Gumbel distribution more accurately captured the tails of the data distributions when compared to the Fréchet distribution. Following these results, the Gumbel distribution will be employed to describe the extreme value FIPs from numerous titanium FEM simulations and will be discussed in Chapter 4.

CHAPTER 3

CYCLIC PLASTICITY EXPERIMENTS AND POLYCRYSTAL MODELING

Introduction

Titanium alloys are utilized in many advanced engineering applications owing to its high strength-to-weight ratio, corrosion resistance, and high temperature strength. Although its utilization industry is often inhibited by high cost, it remains highly attractive for biomedical implants, athletic equipment, and several aerospace applications where the demand for exceptional properties out-weigh the additional cost (Boyer, 1996). The mechanical properties of α-β Ti alloys are strongly influenced by microstructure and crystallographic texture formed as a result of thermo-mechanical processing (Bache and Evans, 2001; Lütjering, 1998). Depending on the processing route, the microstructure morphology can be tailored to variations of the following forms: an equiaxed structure composed of equivalent sized primary α-phase (HCP) grains, a duplex structure comprised of a mixture of α-phase and colony phase (secondary α with BCC β-phase) grains, or a fully lamellar, a.k.a. Widmanstätten, structure composed of prior β-phase grains containing α-phase laths (Welsch et al., 1994). These different microstructures exhibit compromise relationships between beneficial and detrimental effects on the performance of the alloy (Lütjering, 1999). The broad span of achievable properties for α + β titanium alloys has naturally drawn researchers to investigate the correlation between its microstructure morphology and mechanical behavior (Filip et al., 2003; Lin et al., 1984). These experimental works have attempted to isolate attributes of microstructure morphology to quantify their individual effects on yield and ultimate strengths, ductility, and fatigue properties.

Increased computational power has opened the possibility to study complex microstructure-property relation through numerical simulation. This prospect can lead to a significant cost savings by reducing the required number of experiments necessary to determine a target microstructure and associated process route. Additionally, it is possible to control the simulated microstructure to isolate key morphological aspects in a manner that may not be practical experimentally. The current state of the art for studying microstructure-sensitive mechanical behavior is through the utilization of crystal plasticity models simulated with finite-element models (McDowell, 2007, 2008, 2009; McDowell and Olson, 2008; McDowell and Dunne, 2010; Roters et al., 2010) These models describe complex mechanical behavior through the explicit assignment of grain orientation and disorientation distributions, as well as material-specific deformation mechanisms, e.g., crystallographic slip (Peirce et al., 1982), twinning (Kalidindi, 1998), and phase transformation. These attributes of crystal plasticity models grant a distinct advantage over traditional initially isotropic, homogeneous plasticity models that ignore details of microstructure, and offer improved modeling of plastic strain localization (Goh et al., 2003) which is critical for evaluating high cycle fatigue performance (McDowell, 1996, 2007, 2009; McDowell and Dunne, 2010) Several early studies have successfully utilized crystal plasticity frameworks to evaluate Ti-6Al-4V fretting fatigue performance (Goh et al., 2001; Morrissey et al., 2001), creep deformation (Hasija et al., 2003), and twinning (Salem et al., 2005). These applications have established the value of crystal plasticity for microstructure-sensitive modeling of Ti alloys. However, before employing these models for the purpose of materials design it is important to calibrate the model frameworks to experimental data to ensure physically relevant results. For example, Mayeur (2004) built a 3D crystal plasticity model to describe α-β Ti-6Al-4V deformation and calibrated his model to experimental results from Kurath (1999) before performing fretting fatigue simulations. Also, Zhang et al. (2007) calibrated Mayeur's model to

complex loading histories in order to capture strain rate sensitivity in the model before proceeding to simulate cyclic fatigue of Ti-6Al-4V.

In this study, two distinct crystal plasticity model frameworks have been calibrated to cyclic deformation data obtained from experiments performed on three different titanium alloy microstructures: (1) Ti-6Al-4V β-annealed, (2) Ti-18 solution-treated, age-hardened (STA) (Fanning, 2011), and (3) Ti-18 beta-annealed, slow-cooled, age-hardened (BASCA). The first of these models was originally developed by Mayeur (2004) and consists of a power law relation between the strain rate and applied stress while the latter model includes the thermally-activated flow rule proposed by Kocks et al. (1975). Initially, the characterization of each microstructure is presented followed by the experimental procedures and results. Both constitutive frameworks have been coded as ABAQUS User MATerial subroutines (ABAQUS, 2011) and their individual methodologies are outlined. The estimated parameter sets for each model, along with comparisons between experimental and simulation results, are then discussed the Ti-64, Ti-18 STA, and Ti-18 BASCA materials. Finally, concluding remarks are summarized at the end of the Chapter.

Materials

Ti-64 β-annealed microstructure

Ti-6Al-4V (Ti-64) is the most commonly used Ti alloy having numerous industrial applications ranging from aerospace structures to biomedical implants. The β-annealed Ti-64 material was initially characterized through optical microscopy by mounting samples in an epoxy-resin mold then grinding and polishing the surfaces with a Streuers Rotopol-15 polisher. The final polishing step utilized a 0.02 μm colloidal silica slurry. Shortly after the final polish, the samples were swab etched with a 0.5% HF solution for approximately 20 seconds to reveal the grain boundaries. A micrograph of

the Ti-64 β-annealed structure is shown in Figure 3.2a. The characterization of the β-annealed alloy revealed a coarse, lamellar structure with grains as large as several hundred microns; moreover, the microstructure is completely composed of α + β colony grains. These colony grains consist of α-phase (HCP) laths with small interstitial β-phase (BCC) laths. The alpha lath thickness was determined to be an average of 3 μm through an optical microscopy method similar to Fowler (1989). The material was sectioned and sent to EBSD Analytical Inc. (Lehi, UT) to measure spatial microstructure statistics, e.g., grain size distribution and orientation distribution of the transverse and longitudinal cross-sections of the microstructure via EBSD. The received micrograph and texture color map of the transverse sectional view are provided in Figure 3.1 and the basal plane pole figures appear in Figure 3.2b. Additional EBSD characterization Figures can be referenced in Appendix A. The step size in these scans was set to 4 μm and higher resolution scans at 0.3 μm and 60 nm were performed to better capture the phase volume fraction of the very fine β-phase laths. The structure was observed to be predominately α-phase which composed 98% of the volume fraction and the mean colony size was determined to be 165 μm. The acquired microstructure statistics are incorporated into the numerically reconstructed microstructure to support ABAQUS simulations.

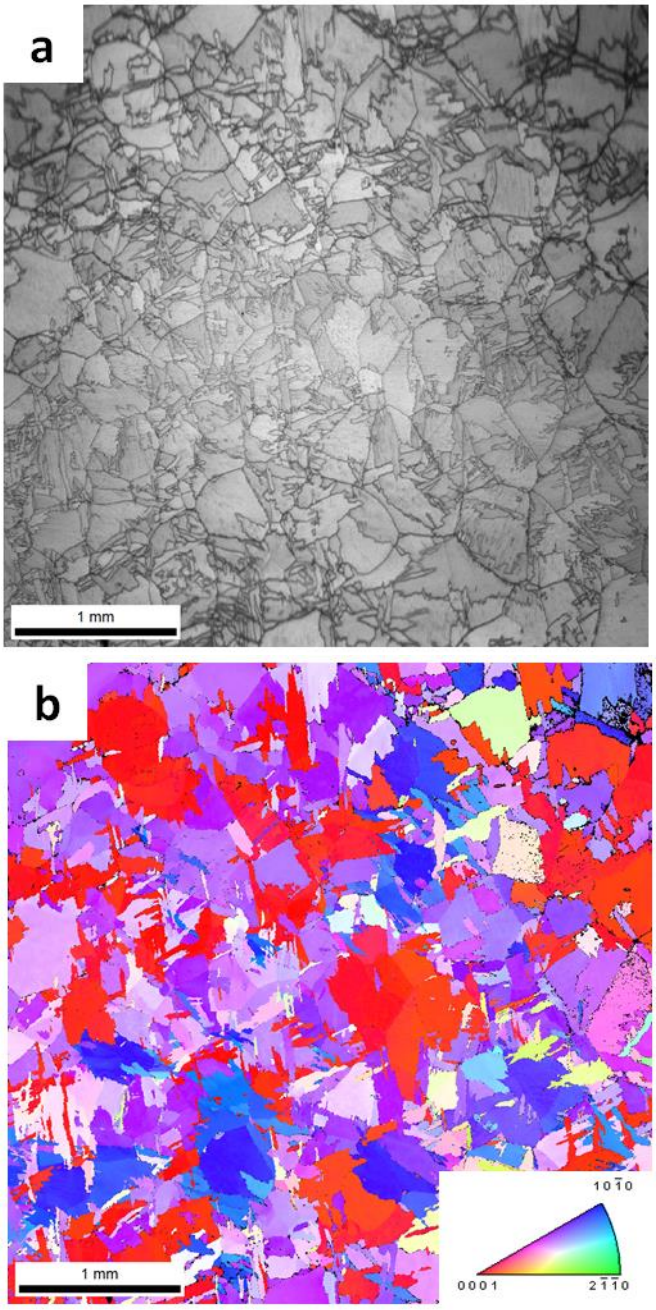

Figure 3.1. (a) Optical micrograph of Ti-64 in β-annealed condition, and (b) matching texture color map acquired from an EBSD scan with 4 μm step size.

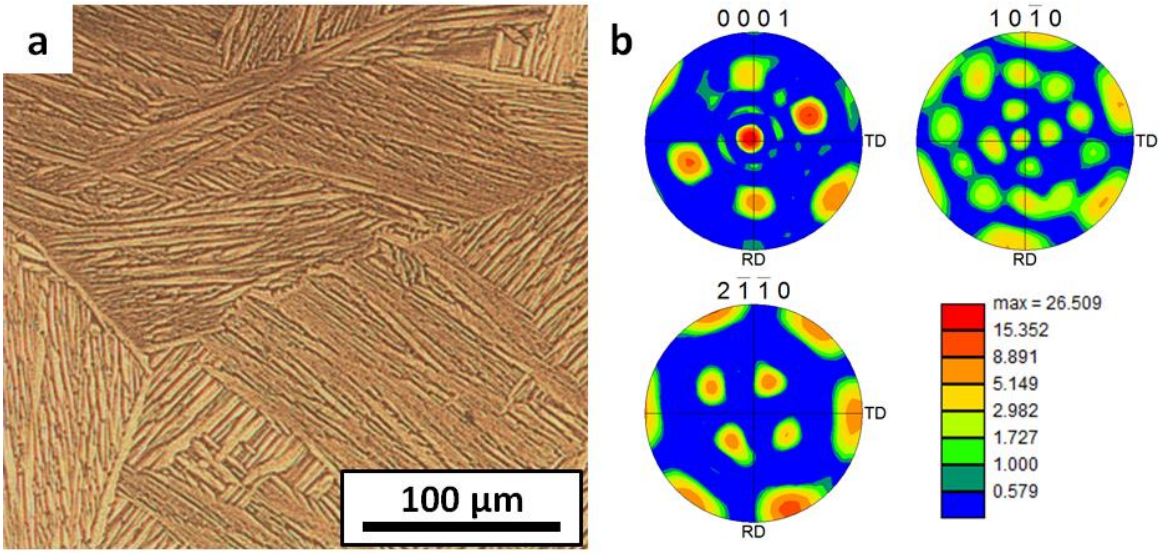

Figure 3.2. (a) Optical micrograph depicting the alpha phase laths in the colony structures for the Ti-64 β-annealed material, and (b) pole figures from the EBSD scan.

Ti-18 STA microstructure

The second material is Ti-18, which is a near-β titanium alloy developed by Titanium Metals Corporation (Exton, PA) to serve as an incremental improvement to Ti-5Al-5Mo-5V-3Cr-0.6Fe (Ti-5553) (Fanning, 2011). Ti-5553 is typically processed in a solution-treated age hardened (STA) condition and it is able to provide excellent strength for large forged parts with less sensitivity to processing parameters when compared to similar near-β titanium alloys (Nyakana et al., 2005). These traits are very attractive for airplane structures, particularly landing gear components (Boyer and Briggs, 2005). The selected STA processing of the Ti-18 material generated a fine bi-modal phase distribution of beta phase (BCC) grains along with small alpha phase (HCP) grains that precipitated into the beta phase matrix during cooling. An optical micrograph and matching texture color map of the transverse cross-sectional face are displayed in Figure 3.3, and relevant pole figures appear in Figure 3.4. Additional EBSD characterization Figures for the Ti-18 STA microstructure can be found in Appendix B. These figures show that the β-phase grains dominate the matrix with 72% of the volume fraction and they also possess a larger average grain size of 3.5 µm compared to 1 µm for the α-phase

precipitates. A significant micro-texture is observed for the β-phase with similar orientations spanning several grains. This micro-texture can be expected to cause long range interaction effects and must be taken into account when calibrating the plasticity models.

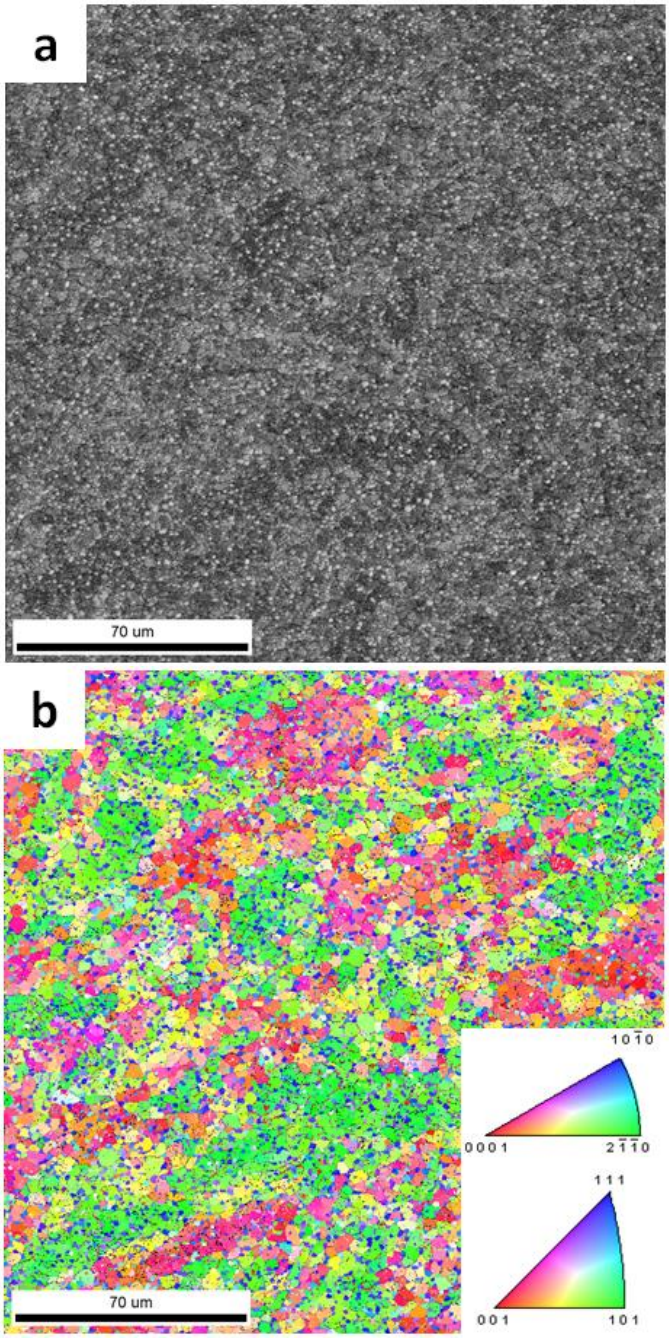

Figure 3.3. (a) Optical micrograph of the Ti-18 STA microstructure and (b) matching texture color map from an EBSD scan with a 0.2 μm step size.

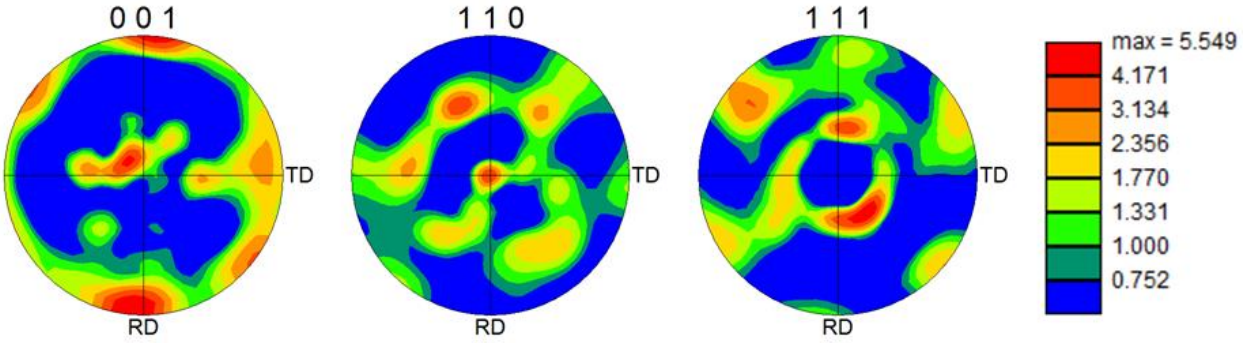

Figure 3.4. Pole figures from EBSD scan of the Ti-18 STA material for the β-phase.

Ti-18 BASCA microstructure

The Ti-18 alloy was also obtained in a β-annealed, slow cooled and aged (BASCA) condition. This processing schedule produced a Widmanstätten microstructure consisting of alpha laths grown with varying orientations within large prior beta phase grains. The volume fractions for the α- and β-phases were nearly the same at 52% and 48%, respectively. This is a much higher volume fraction for the β-phase when compared to that in the Ti-64 β-annealed structure. A micrograph and texture color map of the Ti-18 BASCA microstructure are provided in Figure 3.5 and more EBSD scan images are included in Appendix C. To more accurately capture the large β grain size and orientation statistics, an additional scan was conducted which covered a 7.8 mm by 3.8 mm area, shown in Figure 3.8. This large area scan showed that the overall grain textures were dominated by the β–phase and the mean colony grain size was determined to be 146 μm. A pole figure of the β phase for the large area scan appears in Figure 3.7, generated via MTEX (Bachmann et al., 2010), an open source MATLAB (2011) plug-in.

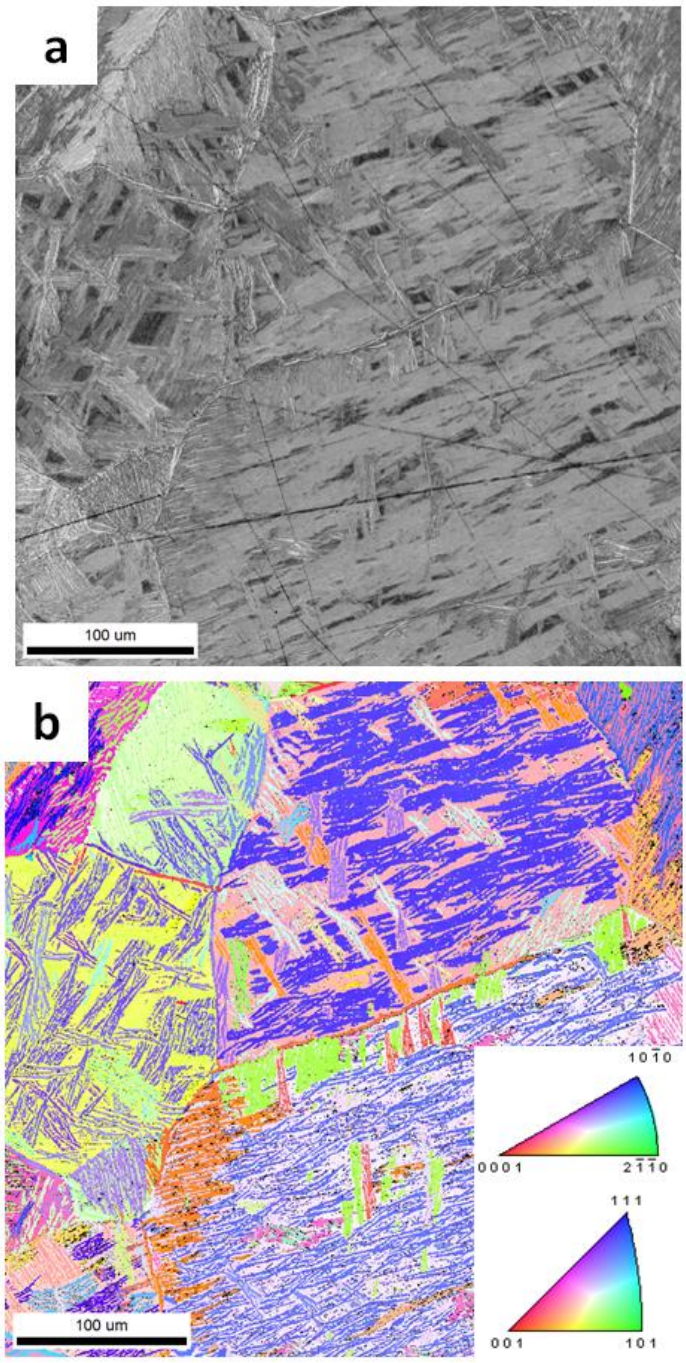

Figure 3.5. (a) An optical micrograph displaying the Ti-18 BASCA microstructure and a (b) matching texture color map from an EBSD scan having a 0.2 μm step size.

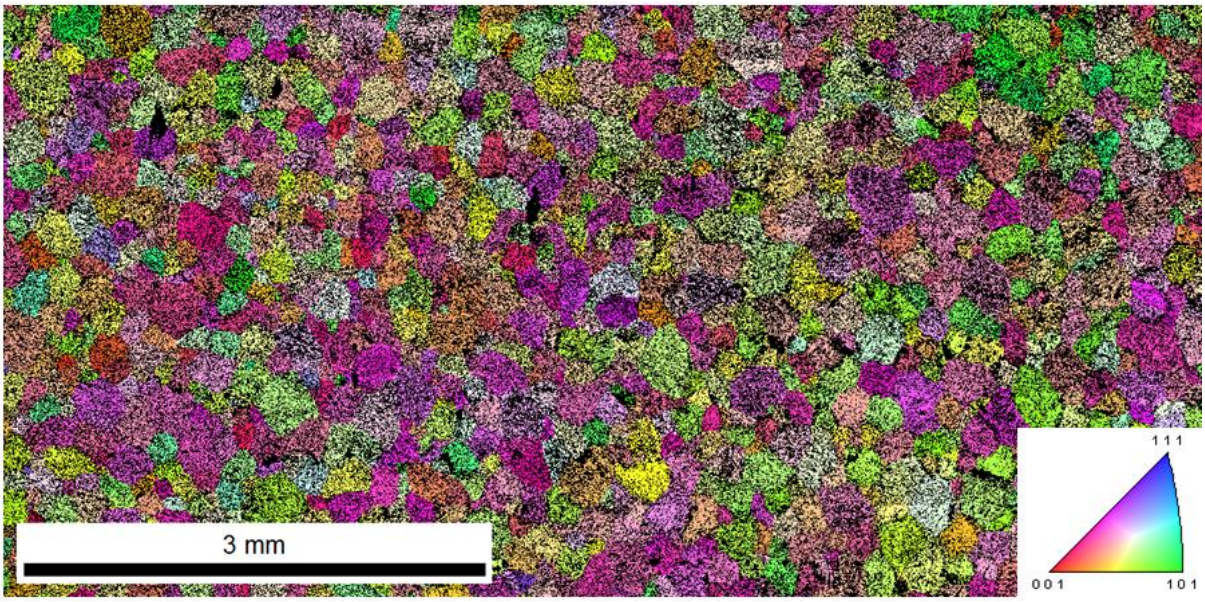

Figure 3.6. A texture color map of the β-phase orientation in the Ti-18 BASCA microstructure from a large area EBSD scan with a step size of 5 μm.

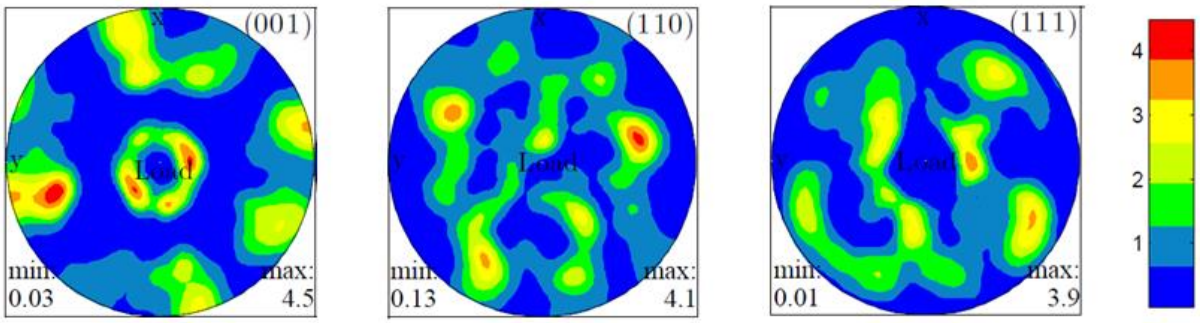

Figure 3.7. Pole figures for the β-phase data acquired from the large area EBSD scan of the Ti-18 BASCA material.

Experimental Results

Uniaxial monotonic and cyclic deformation experiments were performed on the different microstructures for the purpose of supporting constitutive model calibration in the Mechanical Properties Research Lab (MPRL) at Georgia Tech. All materials were machined into dog-bone specimens compliant with ASTM-E606 (2004). The monotonic and cyclic loading experimental matrices and experimental results for the Ti-64 and Ti-18 alloys are discussed next.

Ti-64 β-annealed microstructure results

The experimental matrix for the Ti-64 β-annealed microstructure is shown in Table 3.1. The experiments probed different levels of cyclic plasticity as well as temperature dependence, and were run to target numbers of cycles listed in the right column in Table 3.1. The elevated temperature experiments were conducted using an induction heating apparatus in the MPRL (Fernandez-Zelaia, 2012). Monotonic tension experiments were taken to failure and the results at both room temperature and 450^{o}C are shown in Figure 3.8. Monotonic properties are listed in Table 3.2, where the yield strength is based on 0.2% strain offset. The material displayed a dramatic reduction of strength at elevated temperature, with approximately 60% of the ultimate tensile strength retained. This strength loss is consistent with previous studies with titanium (Gysler and Lütjering, 1982) and is a major reason that 450^{o}C is near the highest application temperatures of Ti-64. Example uniaxial cyclic deformation results for both temperatures are shown in Figure 3.9. The room temperature cyclic data exhibits cyclic softening for the various strain rates investigated. However, cyclic strain hardening behavior was observed during the elevated temperature experiments. The material did not show significant strain rate sensitivity over the range of tested strain rates between $5x10^{-4}$ s^{-1} and 10^{-3} s^{-1}.

Table 3.1. Matrix of experiments for the Ti-64 β-annealed microstructure.

Specimen Number	Loading Ratio	Experiment Temperature (°C)	Strain Rate (s^{-1})	Strain Amplitude (%)	Cycles
24	0	23	$5x10^{-4}$	--	--
3	-1	23	$5x10^{-4}$	0.5	125
9	-1	23	$5x10^{-4}$	0.8	110
27	-1	23	$5x10^{-4}$	1.0	100
26	-1	23	10^{-3}	0.5	3000
2	-1	23	10^{-3}	0.8	150
7	-1	23	10^{-3}	1.0	205
21	0	450	$5x10^{-4}$	--	--
1	-1	450	$5x10^{-4}$	0.5	110
16	-1	450	$5x10^{-4}$	0.8	105
13	-1	450	$5x10^{-4}$	1.0	100
10	-1	450	10^{-3}	0.5	120
5	-1	450	10^{-3}	0.8	105
25	-1	450	10^{-3}	1.0	105

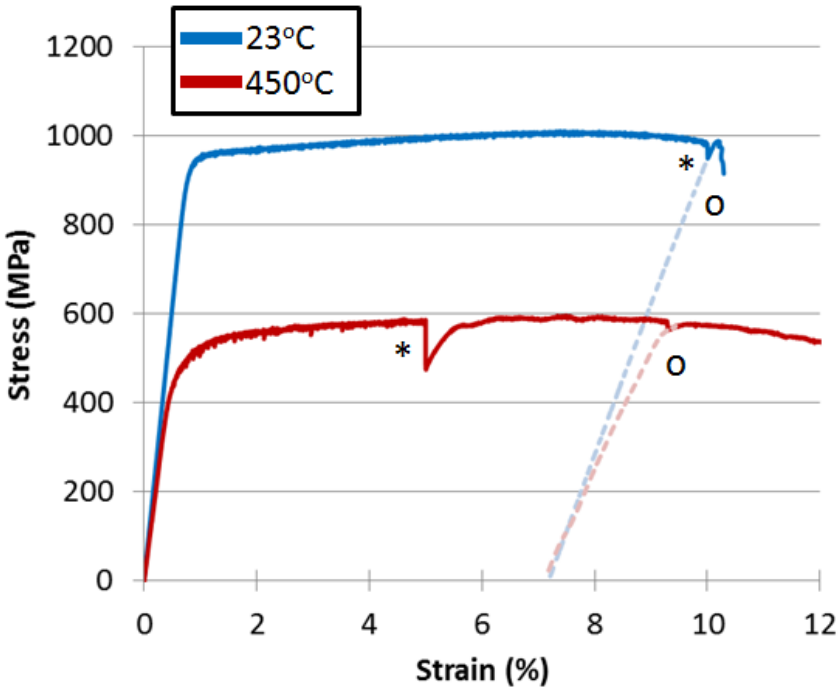

Figure 3.8. Measured monotonic tension engineering stress-strain curves for the Ti-64 β-annealed material at room temperature and 450°C, at a strain rate of $5x10^{-4}$ s^{-1}. The extensometer was removed and loading was switched to displacement control at points (*). The specimens were elastically unloaded at points (o).

Table 3.2. Summary of Ti-64 β-annealed mechanical properties from monotonic tests.

Temperature (°C)	Yield Strength (MPa)	Ultimate Strength (MPa)	Failure Strain (%)
23	955	1010	10.29
450	485	596	13.77

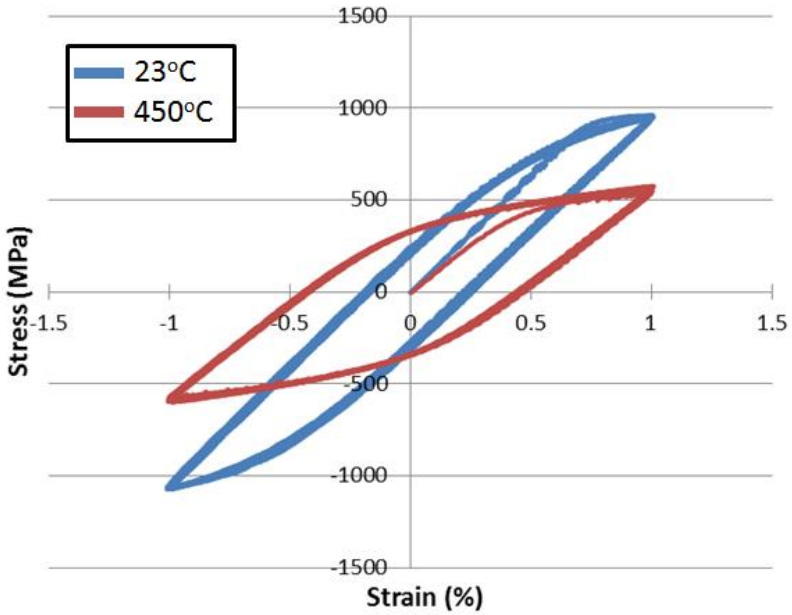

Figure 3.9. Measured **c**yclic deformation engineering stress-strain hysteresis loops for fully reversed, 1% strain amplitude, at $5x10^{-4}$ s^{-1} strain rate for the Ti-64 microstructure at 23^{o} C and 450^{o} C. Each of these specimens was cycled 100 times.

Ti-18 results

The experiments for the Ti-18 STA and the Ti-18 BASCA near-β titanium microstructures are summarized in Tables 3.3 and 3.4, respectively. Room temperature monotonic tension experiments were conducted to failure, as shown in Figure 3.10. The STA treatment of the Ti-18 alloy produced superior monotonic properties including a higher yield strength, ultimate strength, and failure strain. An interesting observation is the large amount of softening in the monotonic response for the STA microstructure. Significant softening in the STA structure is also observed in the cyclic loading response in Figure 3.11. The Ti-18 BASCA material exhibited strain bursts during the compressive loading regimes of the cyclic hysteresis response. Neither microstructure was found to be strain rate sensitive for strain rates in the range of $5x10^{-5}$ s^{-1} to 10^{-3} s^{-1}.

Table 3.3. Cyclic uniaxial experiments on the Ti-18 STA microstructure at room temperature.

Specimen Number	Loading Ratio	Strain Rate (s^{-1})	Strain Amplitude (%)	Cycles
7	0	$5x10^{-4}$	--	--
8	-1	$5x10^{-5}$	1.3	100
2	-1	$5x10^{-4}$	1.3	110
3	-1	10^{-3}	0.8	125
1	-1	10^{-3}	1.3	110
6	-1	10^{-3}	1.5	115

Table 3.4. Cyclic uniaxial experiments on the Ti-18 BASCA material at room temperature.

Specimen Number	Loading Ratio	Strain Rate (s^{-1})	Strain Amplitude (%)	Cycles
4	0	$5x10^{-4}$	--	--
3	-1	$5x10^{-4}$	1.3	115
6	-1	10^{-3}	0.8	120
2	-1	10^{-3}	1.3	125
11	-1	10^{-3}	1.5	125

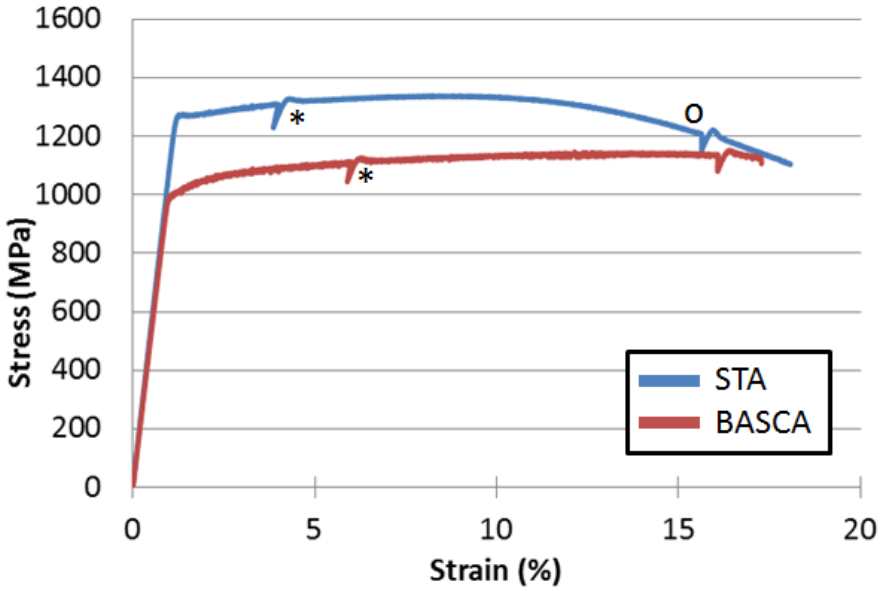

Figure 3.10. Room temperature monotonic engineering stress-strain curves for Ti-18 microstructures at $5x10^{-4}$ s^{-1} strain rate. The extensometer was removed and control mode was switched to displacement control at points (*). The specimens experienced a brief strain hold at (o).

Table 3.5. Monotonic room temperature properties of the Ti-18 microstructures.

Microstructure	Yield Strength (MPa)	Ultimate Strength (MPa)	Failure Strain (%)
STA	1270	1339	18.08
BASCA	1000	1152	17.28

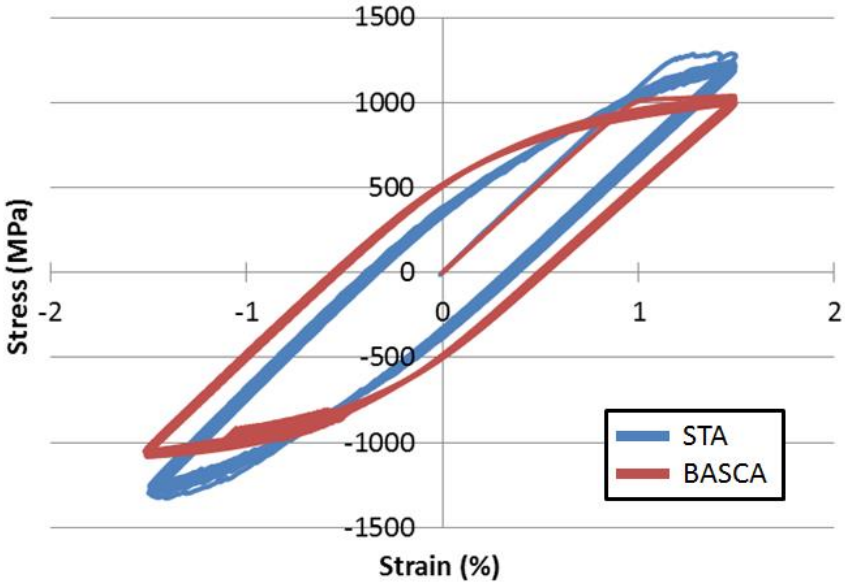

Figure 3.11. Initial ten cycles of engineering stress-strain response for the two Ti-18 alloy microstructures for fully reversed, 1.5% constant strain amplitude, and 10^{-3} s^{-1} strain rate at room temperature.

Crystal Plasticity Framework

The crystal plasticity model assumes thermally activated dislocation glide through the lattice (Asaro, 1983; McGinty, 2001). The deformation gradient is multiplicatively decomposed into dislocation slip and elastic lattice deformation, including rigid body rotation of the crystalline lattice, i.e.,

$$\mathbf{F} = \mathbf{F}^e \cdot \mathbf{F}^p \tag{3.1}$$

Where $\mathbf{F}^e$ is representative of the elastic stretching and rigid body rotation of the lattice and $\mathbf{F}^p$ describes the cumulative effect of dislocation migration through the lattice. The plastic velocity gradient for the isoclinic, lattice invariant intermediate configuration is

determined by summing the crystallographic shearing rates over all of α slip systems (Asaro, 1983), i.e.,

$$\hat{\mathbf{L}}^p = \sum_{\alpha=1}^{N_{sys}} \dot{\gamma}^\alpha \left(\mathbf{s}_0^\alpha \otimes \mathbf{n}_0^\alpha \right) = \dot{\mathbf{F}}^p \cdot \left(\mathbf{F}^p \right)^{-1}, \tag{3.2}$$

where $\mathbf{n}_0^\alpha$ and $\mathbf{s}_0^\alpha$ are the slip plane and slip direction normal vectors, respectively, in the reference configuration. These vectors have the same orientation in both the reference and isoclinic intermediate configurations.

In previous crystal plasticity work on titanium, the primary α-phase grains have been assigned 24 slip systems (Mayeur, 2004): 3 $\langle 11\bar{2}0 \rangle \{0001\}$ basal, 3 $\langle 11\bar{2}0 \rangle \{10\bar{1}0\}$ prismatic, 6 $\langle 11\bar{2}0 \rangle \{10\bar{1}1\}$ first order pyramidal, and 12 $\langle 11\bar{2}3 \rangle \{10\bar{1}1\}$ second order pyramidal slip systems. The relative strength of these slip systems has been reviewed by Mayeur and McDowell (2007). The colony phase grains are assumed to be a hybrid α-β type (Mayeur, 2004) consisting of 24 slip systems: 12 basal, prismatic, and first order pyramidal α-phase slip systems and 12 $\langle 111 \rangle \{110\}$ BCC slip. The Burgers orientation relationship (BOR) between the α and β phase laths in the lamellar colony grains is specified as $(0001)_\alpha \parallel \{110\}_\beta$ and $\langle 11\bar{2}0 \rangle_\alpha \parallel \langle 111 \rangle_\beta$ (Ankem and Margolin, 1980). The following sections review the evolution equations (kinetics) of slip and hardening incorporated into finite element simulations as ABAQUS UMAT subroutines.

Model 1: Power Law Flow Rule

The power law formulation was first implemented for Ti-6Al-4V by Mayeur (2004) ; it was then extended to describe complex loading histories by Zhang et al. (2007) and high-cycle fatigue (HCF) loading by Bridier et al. (2009). Przybyla and McDowell (2011) utilized this calibrated model to investigate HCF performance over a range of Ti-

64 microstructures by employing extreme value statistics. The power law shearing rate relation is given by

$$\dot{\gamma}^{\alpha} = \dot{\gamma}_o \left\langle \frac{\left|\tau^{\alpha} - \chi^{\alpha}\right| - \kappa^{\alpha}}{D^{\alpha}} \right\rangle^{M} \operatorname{sgn}\left(\tau^{\alpha} - \chi^{\alpha}\right) \tag{3.3}$$

Here, D^{α} is the drag stress on the α^{th} slip system, $\dot{\gamma}_o$ is the reference shearing rate, χ^{α} is the back stress, and κ^{α} is the threshold stress. The threshold stress is defined as the sum of the Hall-Petch strength term and a softening term, κ_s^{α}, i.e.,

$$\kappa^{\alpha} = \frac{\kappa_y}{\sqrt{d}} + \kappa_s^{\alpha} \tag{3.4}$$

where κ_y is the Hall-Petch slope and *d* is the mean slip distance in the α-phase (primary or secondary). The strength contribution of the Hall-Petch term is assumed not to evolve so that the evolution of the threshold stress is governed solely by the softening term, which follows a dynamic recovery law, i.e.,

$$\dot{\kappa}^{\alpha} = \dot{\kappa}_s^{\alpha} = -\mu\kappa_s \left|\dot{\gamma}^{\alpha}\right| \tag{3.5}$$

where μ is the softening rate coefficient. The initial value of κ_s^{α}, prior to the breakdown of short range order, is given by $\left(\kappa_s^{\alpha}\right)_{t=0}$. The drag stress is determined from its relationship with the critical resolved shear stress and the threshold stress (Bridier et al., 2009), i.e.,

$$D^{\alpha} = \tau_{CRSS}^{\alpha} - \kappa_{t=0}^{\alpha} = \tau_{CRSS}^{\alpha} - \frac{\kappa_y}{\sqrt{d}} - \left(\kappa_s^{\alpha}\right)_{t=0} \tag{3.6}$$

Here, τ_{CRSS}^{α} is the critical resolved shear stress on the α^{th} slip system. The drag stress does not evolve so that $\dot{D}^{\alpha} = 0$. The back stress is initially set to zero and it evolves according to an Armstrong-Frederick direct hardening/dynamic recovery relation (Armstrong and Frederick, 1966), i.e.,

$$\dot{\chi}^{\alpha} = h\dot{\gamma}^{\alpha} - h_D \chi^{\alpha} \left| \dot{\gamma}^{\alpha} \right| \tag{3.7}$$

In Equation 3.7, h is the direct hardening coefficient and h_D is the dynamic recovery coefficient. The saturated value of the back stress is determined by the ratio of the direct hardening constant divided by the dynamic recovery term corresponding to $\dot{\chi}^{\alpha} = 0$, i.e.,

$$\chi_{sat} = \frac{h}{h_D} \tag{3.8}$$

The critical resolved shear stress (CRSS) of the α + β colony grains is known to be higher than that of the primary α-phase grains for slip systems due to the presence of the lamellar interfaces. To account for this difference in the CRSS, a factor of 1.25 is applied to the basal slip systems and the prismatic slip system that is oriented parallel to the lamellar laths (Bridier et al., 2009), i.e.,

$$\tau_{CRSS}^{\alpha}(\alpha+\beta) = 1.25\tau_{CRSS}^{\alpha}(\alpha) \tag{3.9}$$

The critical resolved shear stress in compression has also been modified to account for the tension-compression asymmetry observed experimentally. It has been hypothesized that the physical basis of this asymmetry is the non-planar core structure observed in a-type screw dislocations in titanium (Naka et al., 1988), and core constriction necessary to render the dislocations mobile is not of Schmid character. To model this non-Schmid behavior, Qin and Bassani (1992) suggested that the critical

resolved shear stress be augmented by a strength term with linear dependence on secondary shear stresses, i.e.,

$$\tau^{*\alpha} = \tau^{\alpha} + \sum_{i}^{N_{sys}} a_i^{\alpha} \tau_i^{\alpha} \tag{3.10}$$

Where $\tau^{*\alpha}$ is the modified critical resolved shear stress, N_{sys} is the number of influential secondary slip systems for core spreading, and a_i^{α} are model parameters that reflect core constriction contributions. Screw dislocations on prismatic slip planes dominate slip of α-Ti (Naka et al., 1988). It has been proposed that these prismatic dislocations can dissociate into the pyramidal planes that share common slip directions (Mayeur, 2004; Naka et al., 1988).

In the current framework, the prismatic threshold stress is increased in compression by the addition of a non-planar dislocation core strength term. A simple first order 3D criterion for activation of this asymmetry term is adopted as det(**F**) < 1, i.e., indicative of compressive dilatation. While this specific formulation can distinguish between uniaxial tension and compression loading conditions, additional work is necessary to assess whether the condition on det(**F**) is sufficient or requires modification for more complex multiaxial stress states, e.g., combined axial-torsion loading or shear. The asymmetric strength contribution is described by the relations

$$\tau_{CRSS}^{prism} = \tau_{CRSS}^{prism}\Big|_0 + \eta\left(\left|\tau_{RSS}^{pyr1,1}\right| + \left|\tau_{RSS}^{pyr1,2}\right|\right),\ J = \det(\mathbf{F}) < 1 \tag{3.11}$$

$$\tau_{CRSS}^{prism} = \tau_{CRSS}^{prism}\Big|_0,\ J \geq 1$$

where the terms $\tau_{RSS}^{pyr1,1}$ and $\tau_{RSS}^{pyr1,2}$ represent the resolved shear stresses on the two first order pyramidal systems that share the same slip direction as the prismatic plane under consideration, η is a parameter that defines the sensitivity of the asymmetry strength to

the resolved shear stress on these pyramidal planes, and $\tau_{CRSS}^{prism}\Big|_0$ is the critical resolved shear stress for the prismatic slip systems for positive det(**F**). A summary of the previously identified model parameters appears in Table 3.6.

Table 3.6. Parameters of the power law model (Model 1) obtained from literature sources.

Property	Value	Reference
$\dot{\gamma}_o$	0.001 s^{-1}	Goh (2002)
M	15	Zhang et al. (2007)
κ_y	12.7 MPa $mm^{0.5}$	Lederich et al. (1978)
$\chi_{t=0}$	0 MPa	--

Model 2: Activation Enthalpy Flow Rule

The second constitutive model is based on a Kocks-type flow rule (Kocks et al., 1975) which incorporates a thermally activated contribution to dislocation glide past obstacles. The flow rule for this model is given by

$$\dot{\gamma}^{\alpha} = \dot{\gamma}_o \exp\left\{-\frac{\Delta F}{k_b T}\left(1-\left(\frac{\tau_*^{\alpha}}{s_*^{\alpha}}\right)^{p}\right)^{q}\right\}\operatorname{sgn}\left(\tau^{\alpha}-\chi^{\alpha}\right) \tag{3.12}$$

$$\tau_*^{\alpha} = \left|\tau^{\alpha}-\chi^{\alpha}\right| - s_a^{\alpha} \tag{3.13}$$

for the range $0 \le \tau_*^{\alpha} \le s_*^{\alpha}$. Here, k_b is Boltzmann's constant, T is absolute temperature, τ_*^{α} is the effective stress, s_*^{α} is the thermal stress, χ^{α} is the back stress, and s_a^{α} is the athermal threshold stress for the α^{th} slip system. The activation energy, ΔF, is the barrier for thermally activated bypass, where constants *p* and *q* determine the shape of the energy barrier. The athermal threshold stress consists of four different contributions (Britt et al., 2011), i.e.,

$$s_a^\alpha = s_{SS}^\alpha + s_{SRO}^\alpha + s_{disl}^\alpha + s_{HP}^\alpha \tag{3.14}$$

where s_{HP}^α is the Hall-Petch term, s_{disl}^α is the dislocation interaction term, s_{SRO}^α is the short range order term, and s_{SS}^α is the solid solution strengthening term. . The length scale value in the Hall-Petch term is based on the size, d, for the primary α grains and as the secondary α-lath thickness (interlamellar spacing), *IS*, for the colony α + β grains, i.e.,

$$s_{HP}^\alpha(\alpha) = \frac{\kappa_y}{\sqrt{d}}; \qquad s_{HP}^\alpha(\alpha+\beta) = \frac{\kappa_{IS}}{\sqrt{IS}}; \qquad \dot{s}_{HP}^\alpha = 0\ . \tag{3.15}$$

where k_y is the Hall-Petch slope for the grain size, and k_{IS} is the Hall-Petch slop for the α-layer thickness. Experimental results from Lee et al. (2003) show that there can be different Hall-Petch slopes pertaining to the α-grain size and the α-lath thickness. Typically, $k_{IS} < k_y$ (Kim et al., 2004; Maruyama et al., 2002; Perdrix et al., 1999). The dislocation interaction strength is based on a simple Taylor relation, i.e.,

$$s_{disl}^\alpha = \kappa\mu b\sqrt{\rho^\alpha} \tag{3.16}$$

Here, κ is a constant, μ is the temperature dependent shear modulus, *b* is the magnitude of the Burgers vector, and is the dislocation density on the α^{th} slip system. The initial dislocation density is assumed to be 10^6/mm^2, which establishes $s_{\text{disl}}^\alpha|_{t=0}$. The values of the constant κ and the Burgers vector are 0.5 (Picu and Majorell, 2002) and 0.29 nm (Lütjering, 2003), respectively. The dislocation interaction strength evolves indirectly through the change in the dislocation density. The dislocation density evolution is based on a hardening-dynamic recovery form (Mecking and Kocks, 1981), i.e.,

$$\dot{\rho}^\alpha = \left(k_2\sqrt{\sum_\xi \rho^\xi} - k_3\rho^\alpha\right)\left|\dot{\gamma}^\alpha\right| \tag{3.17}$$

where k_2 = 40,000 mm^{-1} and k_3 = 100. The short range order strength term represents the added strength of the solid solution due to the interstitial Ti-Al precipitates. This term is allowed to soften in order to simulate the physical phenomenon of short range order break down from the leading dislocation, which allows trailing dislocations to migrate on the same system with reduced restriction (Neeraj and Mills, 2001). The initial short range order strength has a precipitate solvus temperature of 550 K built in so that the contribution is negligible at elevated temperatures, i.e.,

$$s^{\alpha}_{\mathrm{SRO}}(T, t=0) = \left(s^{\alpha}_{\mathrm{SRO}}\right)_{\max}\left(1 - \frac{1}{1+\exp\left(\frac{-(T-550)}{30}\right)}\right)\mathrm{MPa} \tag{3.18}$$

The short range order contribution evolves according to

$$\dot{s}^{\alpha}_{\mathrm{SRO}} = -k_1 s^{\alpha}_{\mathrm{SRO}}\left|\dot{\gamma}^{\alpha}\right| \tag{3.19}$$

where k_1 is the softening coefficient, and $s^{\alpha}_{\mathrm{SRO}}|_{t=0}$ is the initial value. The final component of the athermal threshold stress is the solid solution strengthening term, s^{α}_{ss}, which is estimated as

$$s^{\alpha}_{SS} = \mathrm{CRSS}^{\alpha}|_{T=650\mathrm{K}} - s^{\alpha}_{\mathrm{SRO}}|_{t=0} - s^{\alpha}_{\mathrm{disl}}|_{t=0} \tag{3.20}$$

This estimation assumes that the athermal threshold stress is equivalent to the high temperature CRSS for each slip system assuming that the grain is sufficiently large so that the Hall-Petch strength contribution is negligible. The high temperature CRSS values have been determined using experimental data from Williams et al. (2002). The solid solution strengthening levels for each slip plane have the following values: 60 MPa

for the basal plane, 65 MPa for the prismatic plane, 250 MPa and 450 MPa for the first and second order pyramidal planes, respectively.

Suri et al. (1998) observed yield strength asymmetry between the a-type basal and prismatic slip directions experimentally, with higher strengths measured in the systems that traverse the lamellar interface, caused by the inhibition of dislocation motion. In our homogenized colony model, the a_1 slip direction is assumed to be parallel to the α/β interface and an addition of 40 MPa is attributed to the a_2 and a_3 athermal stresses. The simulated increased strength for the hard oriented basal slip systems mimics Suri's experimental results, i.e.,

$$s_a^{\alpha}\left(a_2\right) = s_a^{\alpha}\left(a_3\right) = s_a^{\alpha}\left(a_1\right) + 40MPa \tag{3.21}$$

The athermal threshold stress for the prismatic slip planes in the activation enthalpy-based flow rule has been defined to have the same tension-compression asymmetry as was expressed in Equation 3.11, i.e.,

$$s_a^{prism} = s_a^{prism}\Big|_0 + \eta\left(\left|\tau_{RSS}^{pyr1,1}\right| + \left|\tau_{RSS}^{pyr1,2}\right|\right),\ J = \det\left(\mathbf{F}\right) < 1 \tag{3.22}$$

$$s_a^{prism} = s_a^{prism}\Big|_0,\ J \geq 1$$

Again, the $\tau_{RSS}^{pyr1,1}$ and $\tau_{RSS}^{pyr1,2}$ terms represent the resolved shear stresses on the two first order pyramidal planes sharing the same slip direction, η is a sensitivity parameter, and $s_a^{prism}\Big|_0$ is the critical resolved shear stress for the prismatic slip systems under the condition $J \geq 1$, i.e., tensile dilatation.

Finally, the back stress for both phases is initially set to zero ($\chi_{t=0}^{\alpha} = 0$) and is only allowed to evolve for the colony phase grains with a dynamic recovery format similar to Equation 3.7, i.e.,

$$\dot{\chi}^{\alpha}\left(\alpha+\beta\right)=\sum_{\beta}h^{\alpha\beta}\dot{\gamma}^{\beta}-h_{D}\chi^{\alpha}\mid\dot{\gamma}^{\alpha}\mid \tag{3.23}$$

In this formulation, h_D is the dynamic dynamic recovery coefficient. The back stress evolves with an anisotropic hardening coefficient, $h^{\alpha\beta}$, which is biased to capture different slip system interaction effects observed experimentally (Suri et al., 1998). Components of the hardening coefficient matrix are listed in Equation 3.24 (Britt et al., 2011). A summary of the model parameters, including those acquired from previous studies, is listed in Table 3.7.

$$h^{11}=easy\ slip,\quad h^{21}=-0.5h^{11},\quad h^{22}=20h^{11},\quad h^{12}=h^{32}=-1.6h^{11},\quad h^{33}=5h^{11} \tag{3.24}$$

Table 3.7. Parameters for the activation enthalpy model (Model 2).

Property	Value	Reference
$\dot{\gamma}_0$	500,000 s^{-1}	--
k_b	8.617x10^{-5} eV/K	--
κ_y	12.7 MPa $mm^{0.5}$	Lederich et al., (1978)
κ_{IS}	2.7 MPa $mm^{0.5}$	close to Perdrix et al., (1999)
κ	0.5	Picu and Majorell, (2002)
b	2.9x10^{-7} mm	Lütjering, (2003)
ρ_0	10^6 mm^{-2}	--
k_2	40000 mm^{-1}	Britt et al., (2011)
k_3	100	
$(s_{ss}^{\alpha})_{prism}$	65 MPa	Williams et al., (2002)
$(s_{ss}^{\alpha})_{basal}$	60 MPa	
$(s_{ss}^{\alpha})_{pyr<a>}$	250 MPa	
$(s_{ss}^{\alpha})_{pyr<a+c>}$	450 MPa	
$\chi_{t=0}$	0 MPa	--

Parameter Estimation for Ti-64

Ti-64 β-annealed microstructure representation

A modified version of the ellipsoidal packing algorithm implemented by Przybyla (2010) was used to build the polycrystalline, polyphase finite element model (ABAQUS) geometry for the characterized Ti-64 β-annealed microstructure. The ellipsoidal packing algorithm is coded into MATLAB (2011) and randomly places ellipsoids, representing distinct grains, into a 3D volume until a specified packing fraction factor has been met. After the ellipsoidal packing is complete, the ellipsoids are allowed to grow to fill the remaining space in the model. Generated grain sizes are estimated by the relationship (Horálek, 1990)

$$d_{grn} = 0.7\left(V_{grn}\right)^{1/3} \tag{3.25}$$

Once the grains have been defined, MTEX (Bachmann et al., 2010), an open source MATLAB plug-in, is utilized to assign the orientations of each grain by sampling the orientation distribution acquired from the EBSD data. Finally, the misorientation distribution is optimized by randomly switching grain orientations to minimize the calculated error between the model misorientation distribution and the measured misorientation distribution from the EBSD scan. The instantiated Ti-64 microstructure is shown in Figure 3.12. The associated statistical volume element (SVE) includes 150 grains with an average size of 169 μm. This model contains 2,197 elements and was determined to have simulated stress-strain results that closely agreed with much larger ABAQUS models composed of up to 500 grains. A comparison of the simulated basal plane pole figure and the EBSD scan pole figure appears in Figure 3.13. Two sets of experimental results were used at each temperature to calibrate the models for the Ti-64 β-annealed material. The strain amplitudes considered at room temperature were $\varepsilon_a = 1\%$

and $\varepsilon_a = 0.8\%$, with strain rates of $\dot{\varepsilon} = 5\times10^{-4} s^{-1}$ and $\dot{\varepsilon} = 10^{-3}\ s^{-1}$, respectively. For elevated temperature calibration, the strain amplitudes were $\varepsilon_a = 0.8\%$ and $\varepsilon_a = 1\%$, with strain rates of $\dot{\varepsilon} = 5\times10^{-4} s^{-1}$ and $\dot{\varepsilon} = 10^{-3}\ s^{-1}$, respectively. These strain rates and amplitudes were applied as boundary conditions on the instantiated microstructures and the simulation results were calibrated to the selected experiments. Periodic boundary conditions were utilized for all SVEs in this study (cf. Przybyla, 2010).

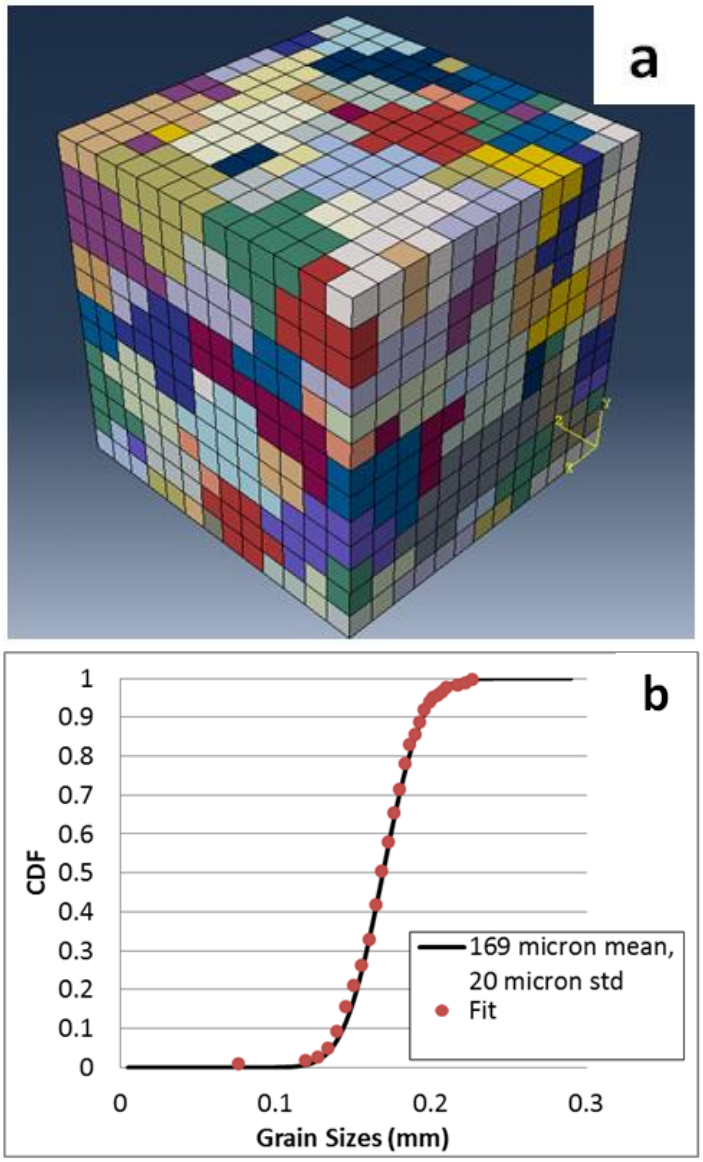

Figure 3.12 (a) ABAQUS geometry utilized for constitutive model calibration and (b) grain size distribution fit.

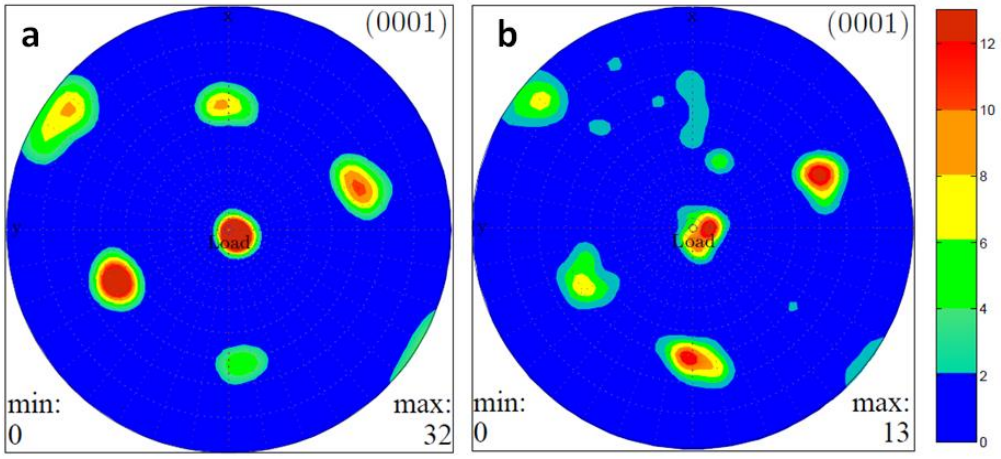

Figure 3.13. Comparison between the textures obtained from the (a) EBSD scan (0001) pole figure and the (b) simulated (0001) pole figure generated in the ABAQUS model via MTEX (Bachmann et al., 2010).

Room Temperature Parameter Estimation for Ti-64

Several model parameters for the crystal plasticity framework can be estimated based on results in the literature as well as from the observed characterization statistics. Parameters that remain unchanged throughout the calibration procedures for Models 1 and 2 are listed in Tables 3.6 and 3.7, respectively. The remaining parameters are estimated to achieve a best fit of the simulations with experimental results (based on an L2 norm of stress error). The initial step in calibrating the models is the estimation of an appropriate set of elastic constants. The elastic constants for titanium single crystals have been measured over a wide range of temperatures by Simmons and Wang (1971), and their observed room temperature values have been successfully utilized to fit the power law model to experimental data by Mayeur (2004) and Zhang et al. (2007). The next step is estimation of the flow rule exponents and drag stress terms, cooperatively utilized to achieve desired stress levels in simulations. The thermal stress, s_*^α, in the activation enthalpy model represents the drag stress and the critical resolved shear stress values in the power law model, τ_{CRSS}^α, indirectly defines the drag stress through the relation in Equation 3.6. After these parameters have been estimated, the threshold terms are estimated such that the simulated yield point agrees with experiments. When estimating

the threshold values for the different slip systems, their relative strengths were not assigned to a specific ratio. However, the estimated values were made to agree with the relative strength trends discussed by Mayeur and McDowell (2007) so that the order of increasing threshold values were assigned to the prismatic, basal, 1st order pyramidal, and 2nd order pyramidal planes, respectively. Lastly, the back stress is fit such that the simulated cyclically stable response matches the shape of the experimental hysteresis loops in the work hardening region. An overall iterative looping process is necessary owing to interdependence of parameters. A comparison of the room temperature experimental results with the simulation results for both models are shown in Figure 3.14 and their associated calibrated values are provided in Table 3.8.

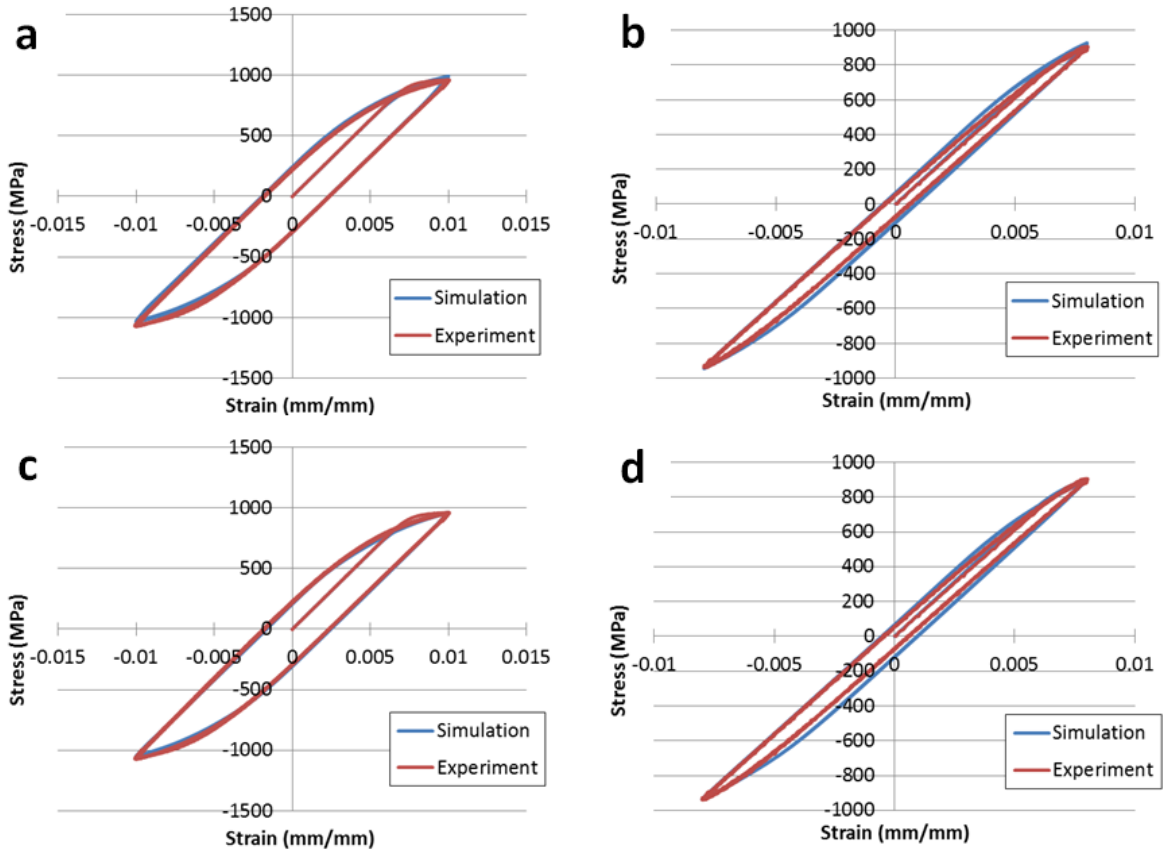

Figure 3.14. Calibrated results for the initial five cycles of loading of the Ti-64 β-annealed microstructure at room temperature for the power law model (Model 1) at (a) ε_a=1%, 5x10^{-4} s^{-1} and (b) ε_a=0.8%, 10^{-3} s^{-1}; and the activation enthalpy model (Model 2) at (a) ε_a=1%, 5x10^{-4} s^{-1} and (b) ε_a=0.8%, 10^{-3} s^{-1}. The experimental results have been smoothened to facilitate comparison.

Table 3.8. (a) Model 1 (power law model) calibrated parameters for Ti-64 at room temperature.

$C11$	172,832 MPa	$(\tau_{cr}^{\alpha})_{prism}$	275 MPa	h	8000 MPa
$C12$	97,910 MPa	$(\tau_{cr}^{\alpha})_{basal}$	350 MPa	h_D	8000
$C13$	73,432 MPa	$(\tau_{cr}^{\alpha})_{pyr<a>}$	470 MPa	η	15
$C33$	192,308 MPa	$(\tau_{cr}^{\alpha})_{pyr<a+c>}$	570 MPa	d_{α}	160 μm
$C44$	49,700 MPa	$(\kappa_s^{\alpha})_{t=0}$	50 MPa	$d_{\alpha+\beta}$	3 μm
		μ	2		

(b) Model 2 (activation enthalpy model) calibrated parameters for Ti-64 at room temperature.

$C11$	172,832 MPa	$(s_*^{\alpha})_{prism}$	460 MPa	h^{11}	15 MPa
$C12$	97,910 MPa	$(s_*^{\alpha})_{basal}$	510 MPa	h_D	1
$C13$	73,432 MPa	$(s_*^{\alpha})_{pyr<a>}$	560 MPa	η	0.21
$C33$	192,308 MPa	$(s_*^{\alpha})_{pyr<a+c>}$	1300 MPa	ΔF	3 eV
$C44$	49,700 MPa	$(s_{SRO}^{\alpha})_{max}$	34 MPa	p	0.4
d_{α}	160 μm	k_1	2	q	1.7
IS	3 μm				

Elevated Temperature Parameter Estimation for Ti-64

After the room temperature model parameters for the Ti-64 material were identified, the calibration process was then repeated to estimate the elevated temperature parameters. Threshold stress and drag stress terms were the primary parameters used to achieve reduced high temperature strength. These values were significantly decreased since they are known to depend strongly on temperature up to 450^{o}C (Williams et al., 2002). The degree of softening incorporated into the models was also significantly decreased since the elevated temperature experimental results exhibited cyclic hardening. The asymmetry term, η, was decreased to match the diminished asymmetry observed in the experimental results with increasing temperature. Figure 3.15 compares the experimental and simulation stress-strain behavior, and the associated calibrated parameters are listed in Table 3.9 for 450^{o}C.

Table 3.9. (a) Model 1 (power law model) calibrated parameters for Ti-64 at 450°C.

$C11$	153,661 MPa	$(\tau_{cr}^{\alpha})_{prism}$	110 MPa	h	8000 MPa
$C12$	104,415 MPa	$(\tau_{cr}^{\alpha})_{basal}$	170 MPa	h_D	8000
$C13$	73,465 MPa	$(\tau_{cr}^{\alpha})_{pyr<a>}$	230 MPa	η	0
$C33$	178,863 MPa	$(\tau_{cr}^{\alpha})_{pyr<a+c>}$	280 MPa	d_{α}	160 μm
$C44$	42,134 MPa	$(\kappa_s^{\alpha})_{t=0}$	5 MPa	$d_{\alpha+\beta}$	3 μm
		μ	2		

(b) Model 2 (activation enthalpy model) calibrated parameters for Ti-64 at 450°C.

$C11$	153,661 MPa	$(s_*^{\alpha})_{prism}$	323.33 MPa	h^{11}	15 MPa
$C12$	104,415 MPa	$(s_*^{\alpha})_{basal}$	381.67 MPa	h_D	1
$C13$	73,465 MPa	$(s_*^{\alpha})_{pyr<a>}$	413.41 MPa	η	0.03
$C33$	178,863 MPa	$(s_*^{\alpha})_{pyr<a+c>}$	960 MPa	ΔF	3 eV
$C44$	42,134 MPa	$(s_{SRO}^{\alpha})_{max}$	0.1 MPa	p	0.4
d_{α}	160 μm	k_1	2	q	1.7
IS	3 μm				

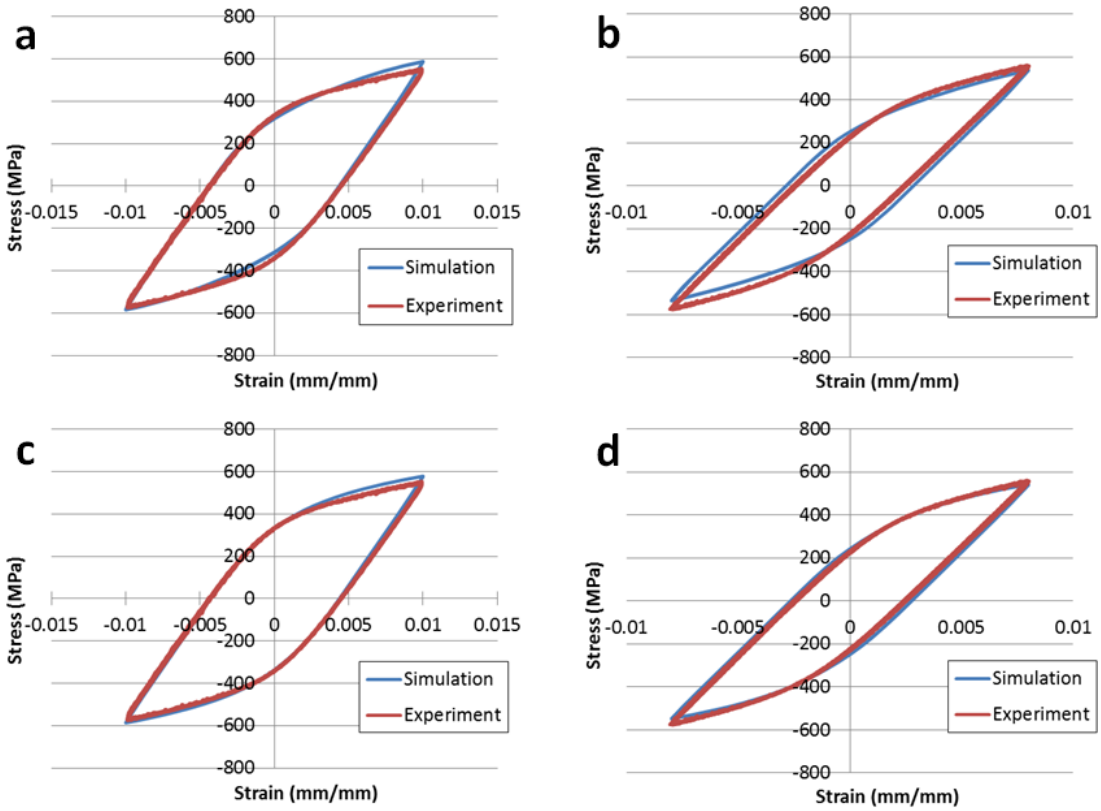

Figure 3.15 Calibrated results for the cyclically stable response for Ti-64 β-annealed microstructure at 450° C for Model 1 (power law model) at (a) ε_a=1%, 10^{-3} s^{-1} and (b) ε_a=0.8%, $5x10^{-4}$ s^{-1}; and Model 2 (activation enthalpy model) (a) ε_a=1%, 10^{-3} s^{-1} and (b) ε_a=0.8%, $5x10^{-4}$ s^{-1}. Experimental data pertain to cycles 10-20 and have been smoothened to facilitate comparison.

The temperature dependence of relevant parameters was then nonlinearly interpolated between room temperature and 450°C. Two expression were utilized to describe the temperature dependence of the elastic constants based on the trends observed in the α-Ti single crystal experimental data in Simmons and Wang (1971). The first is the Varshni, (1970) equation in Equation 3.26, which is used for c_{11}, c_{33}, and c_{44}; c_{12} and c_{13} have been fit through the utilization of the sigmoidal Boltzmann equation in Equation 3.27. The parameters used to fit the elastic constants to the experimental data for the Ti-64 β-annealed microstructure are provided in Table 3.10 and the elastic constants over a range of temperatures appear in Figure 3.16.

$$c = c_0 - \frac{s}{\exp\left(\frac{t}{T}\right) - 1} \tag{3.26}$$

$$c = A_1 + \frac{A_1 - A_2}{1 + \exp\left(\frac{T - T_0}{\Delta T}\right)} \tag{3.27}$$

Table 3.10. Parameters for temperature dependent relationships for elastic constants.

	Varshni Equation			Boltzmann Equation			
	c_0 (GPa)	s (GPa)	t (K)	A_1 (GPa)	A_2 (GPa)	T_0 (K)	ΔT (K)
c_{11}	185	2.67	58.7				
c_{33}	201	1.07	33.7				
c_{44}	53.1	5.00	272				
c_{12}				106	122	299	182
c_{13}				73.5	74.4	209	27.7

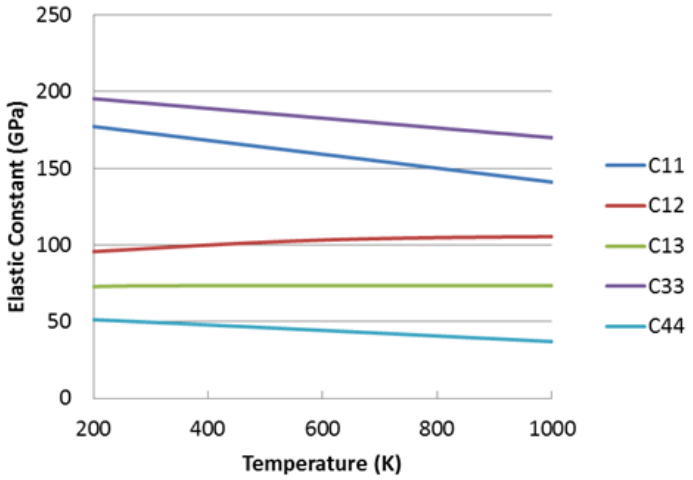

Figure 3.16. Variation of elastic constants with temperature from Equations 3.25-3.26.

The critical resolved shear stresses for the power law model and the thermal stresses in the activation enthalpy model are assumed to follow a power law relation with the temperature of the form

$$CRSS = A(T)^{b} \tag{3.28}$$

with parameters A and b listed in Table 3.11. The asymmetry term, η, was fit to a temperature dependent equation similar to the short range order strength term in Equation 3.18. This allowed for the simulated asymmetry to vanish at elevated temperature. These temperature dependent relationships facilitate simulation of the Ti-64 β-annealed microstructure at temperatures between 300K and 723K.

Table 3.11. (a) Constants for Model 1 (power law) temperature dependent critical resolved shear stress.

Parameter	b	A (MPa K^{-b})
$(\tau_{cr}^{\alpha})_{prism}$	-1.0417	104641
$(\tau_{cr}^{\alpha})_{basal}$	-0.8210	37816
$(\tau_{cr}^{\alpha})_{pyr<a>}$	-0.8125	48377
$(\tau_{cr}^{\alpha})_{pyr<a+c>}$	-0.8081	57239

Table 3.11. (b) Constants for Model 2 (activation enthalpy) temperature dependence.

Parameter	b	A (MPa K^{-b})
$(s_*^\alpha)_{prism}$	-0.4008	4525
$(s_*^\alpha)_{basal}$	-0.3295	3341
$(s_*^\alpha)_{pyr<a>}$	-0.3450	4007
$(s_*^\alpha)_{pyr<a+c>}$	-0.3447	9284

Validation of parameter sets

After estimation, the selected parameters were validated through the utilization of additional experimental data. These data were acquired from fully reversed strain-controlled experiments at a strain rate of $\dot{\varepsilon} = 10^{-3}\ s^{-1}$ and amplitude of $\varepsilon_a = 1\%$ at room temperature and at a strain rate of $\dot{\varepsilon} = 5\times10^{-4} s^{-1}$ and strain amplitude at elevated temperature. Both of these datasets were not used in the calibration process. The simulation results closely agree with the experiments, as shown in Figure 3.17.

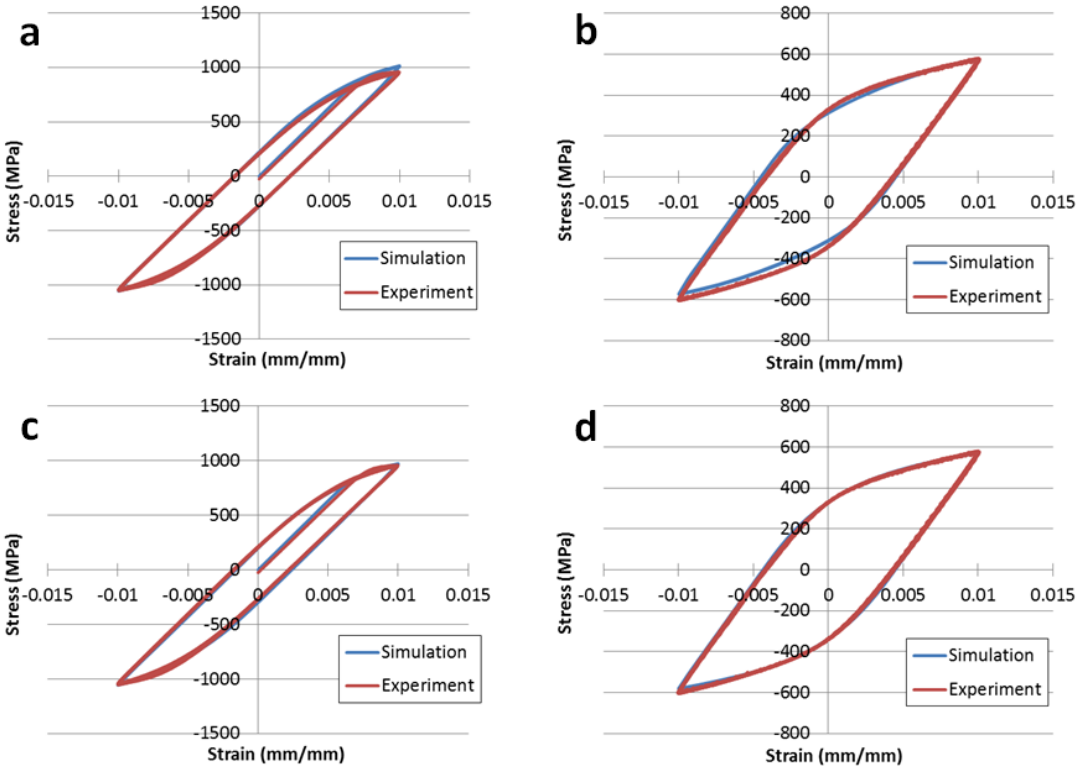

Figure 3.17. Validation of calibrated parameter sets for the power law model (Model 1) at room temperature (a) and 450°C (b) as well as for the activation enthalpy model (Model 2) at room temperature (c) and 450°C (d).

Parameter Estimation for Ti-18 STA

Microstructure Representation

The characterization of the Ti-18 STA microstructure (Figure 3.4) reveals significant microtexture (bands of similar crystallographic orientation). This microtexture poses a significant challenge to simulating a 3D geometry for the material due to the large size disparity between the 1 μm α-phase precipitates, the 3.5 μm β-phase grains, and the ~70 μm microtextured regions. A substantial number of elements would be required to represent this structure due to the combined constraints of generating a cubic volume large enough to appropriately capture the long range effects associated with the microtexture coupled with the requirement for small elements to represent the individual grains. These restrictions can easily force a 3D model to contain in excess of over one million elements, which is computationally prohibitive for parametric study using crystal plasticity models. To represent this microstructure, 2D generalized plane strain elements (CPEG4R) have been utilized to model the longitudinal cross-section; a fully 3D constitutive relation is used for each. The orientation and phase of each element has been defined such that the material properties match the EBSD scan point nearest the element's centroid for both geometries. The selected calibration model is a 100 μm square composed of 2 μm elements; periodic in-plane boundary conditions are imposed. This model was determined to have a very similar stress-strain response to larger models and finer mesh densities. The calibration geometry is displayed in Fig. 18 along with the longitudinal EBSD scan.

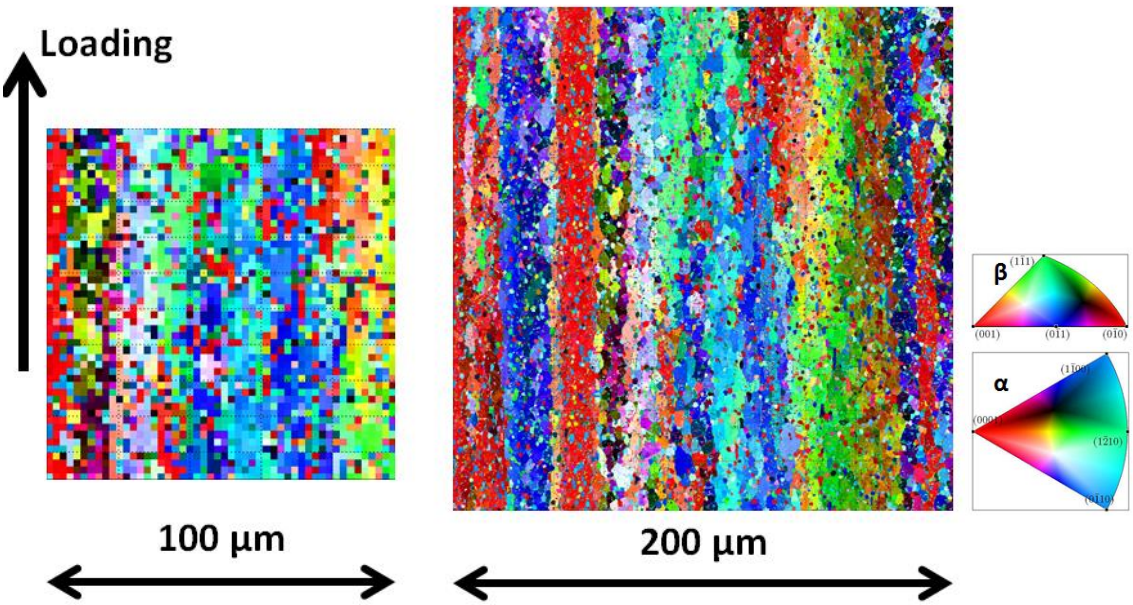

Figure 3.18. ABAQUS 2D geometry (left) used to represent the longitudinal cross-sectional EBSD scan of the Ti-18 STA microstructure on the right.

Estimated Model Parameters

All parameters for this microstructure pertain to the room temperature response. The β-phase of the Ti-18 STA structure is of BCC character. The slip systems in these grains have been modified so that they represent 24 BCC slip systems, including 12 $\langle 111 \rangle \{110\}$ and 12 $\langle 111 \rangle \{112\}$ systems. The strength of the BCC slip systems is defined as 90% of the prismatic slip system strength in the α-phase grains. The asymmetry in the BCC grains has been prescribed to follow Equation 3.11 for $\langle 111 \rangle \{110\}$ the slip systems (Bassani et al., 2001).

To accurately simulate the hardening in the cyclically stable stress-strain response for the activation enthalpy model (Model 2), the back stress evolution is changed to promote isotropic hardening, as is done in the power law model (Model 1, Equation 3.7). Experimental results for the Ti-18 STA specimen at 1.5% strain amplitude and 10^{-3} s^{-1} strain rate were used to calibrate the model parameters for the two constitutive models. The softening parameters in the crystal plasticity models have been estimated so that the

simulated softening correlates very well with the observed experimental softening in the initial five cycles. The estimated parameters are listed in Table 3.12 and the simulation response is shown in Figure 3.19.

Table 3.12. (a) Calibrated Model 1 (power law model) parameters for Ti-18 STA.

$C11$	151,969 MPa	$(\tau_{cr}^{\alpha})_{prism}$	390 MPa	h	250,000 MPa
$C12$	86,090 MPa	$(\tau_{cr}^{\alpha})_{basal}$	440 MPa	h_D	1000
$C13$	64,567 MPa	$(\tau_{cr}^{\alpha})_{pyr<a>}$	590 MPa	η	1.0
$C33$	169092 MPa	$(\tau_{cr}^{\alpha})_{pyr<a+c>}$	690 MPa	d_{α}	1 μm
$C44$	43,700 MPa	$(\kappa_s^{\alpha})_{t=0}$	100 MPa	d_{β}	3 μm
		μ	60	κ_y	2.7 MPa mm$^{0.5}$

(b) Calibrated Model 2 (activation enthalpy model) parameters for Ti-18 STA.

$C11$	151,969 MPa	$(s_*^{\alpha})_{prism}$	520 MPa	h^{11}	18334 MPa
$C12$	86,090 MPa	$(s_*^{\alpha})_{basal}$	570 MPa	h_D	166.67
$C13$	64,567 MPa	$(s_*^{\alpha})_{pyr<a>}$	620 MPa	η	0.13
$C33$	169,092 MPa	$(s_*^{\alpha})_{pyr<a+c>}$	1300 MPa	ΔF	2 eV
$C44$	43,700 MPa	$(s_{SRO}^{\alpha})_{max}$	100 MPa	p	0.4
d_{α}	1 μm	k_1	50	q	1.7
$d_{\alpha+\beta}$	3 μm				

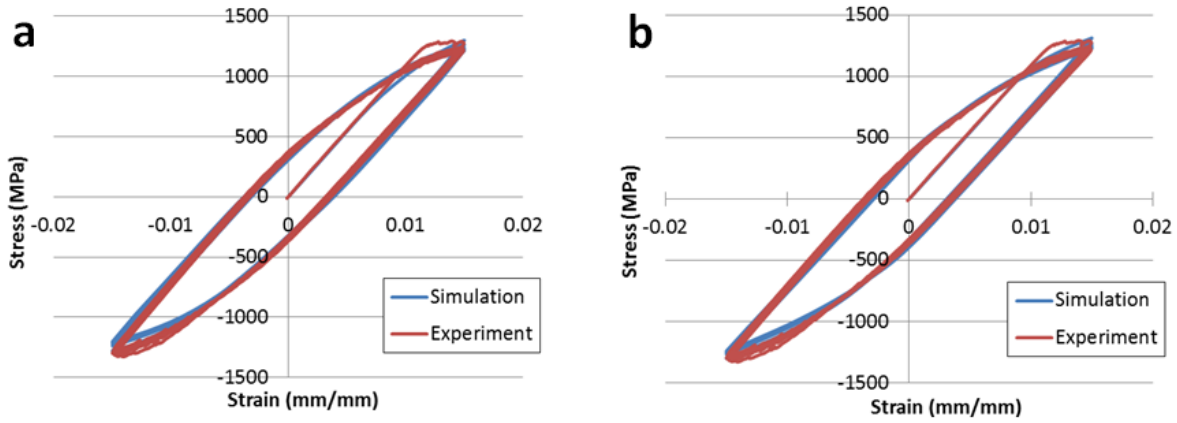

Figure 3.19. Calibrated simulation results for the (a) power law model (Model 1) and the (b) activation enthalpy model (Model 2) for Ti-18 STA. The simulations are compared to experimental results for 1.5% strain amplitude and 10^{-3} s^{-1} strain rate for the initial five cycles.

Validation of Parameters

The estimated parameters were then validated by comparing the simulated response to experimental results for a 1.3% strain amplitude and $5\times10^{-4}\,s^{-1}$ strain rate at room temperature. Simulations are compared with experimental results in Figure 3.20.

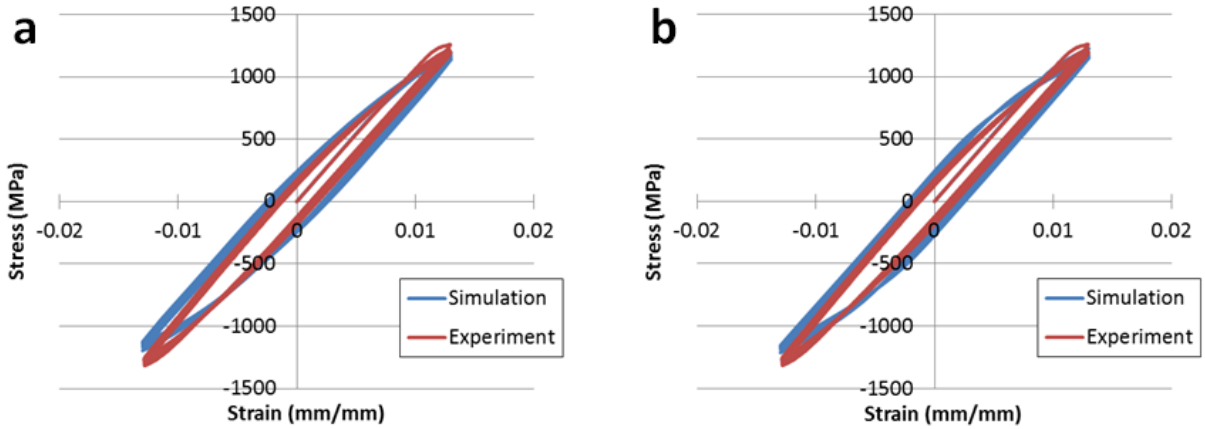

Figure 3.20. Validation of calibrated parameter sets for the (a) power law model (Model 1) and (b) the activation enthalpy model (Model 2) for the Ti-18 STA microstructure loaded at 1.3% strain amplitude and $5x10^{-4}$ s^{-1} strain rate. The initial five cycles of the experimental data are shown.

Parameter Estimation for Ti-18 BASCA

Microstructure Instantiation

The ellipsoidal packing algorithm (Przybyla, 2010) is again exploited to build a 3D polycrystalline microstructure mesh consisting completely of colony phase grains. The grain size of these colonies is defined to fit the statistics received from EBSD Analytical for the large prior beta grains. This grain size distribution was identified to have a mean grain size of 146 μm and a standard deviation of 35 μm. The selected calibration model geometry contains 150 grains fit to the appropriate size and consists of 2,197 C3D8R elements. After the geometry is created, the orientations of each of the single crystals within the matrix are sampled from a pole figure based on EBSD scan information for the β-phase. A generated Ti-18 BASCA model appears in Figure 3.21,

and comparisons of experimental and instantiated β-phase pole figure appear for this SVE is shown in Figure 3.22.

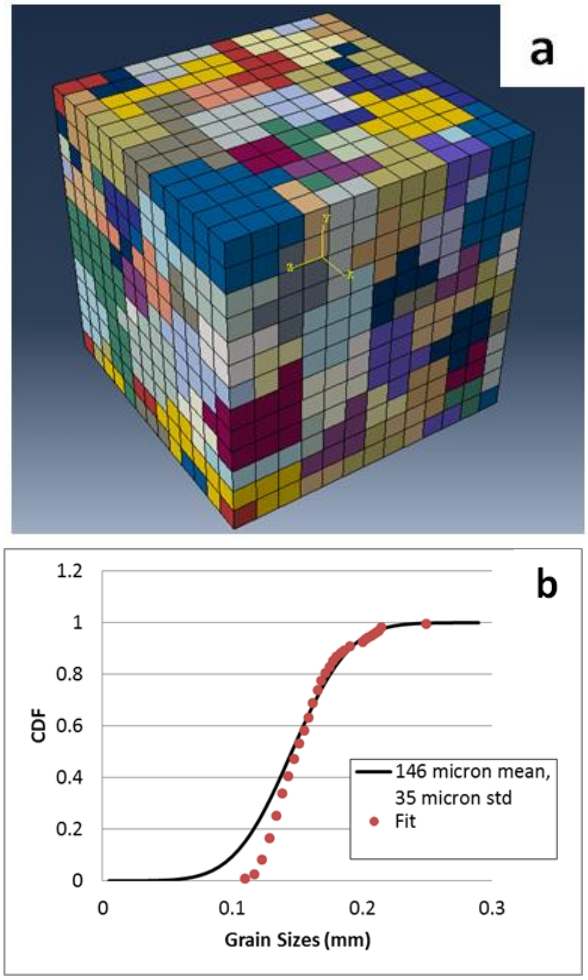

Figure 3.21. (a) ABAQUS voxellated mesh for polycrystal used for constitutive model calibration and (b) grain size distribution fit.

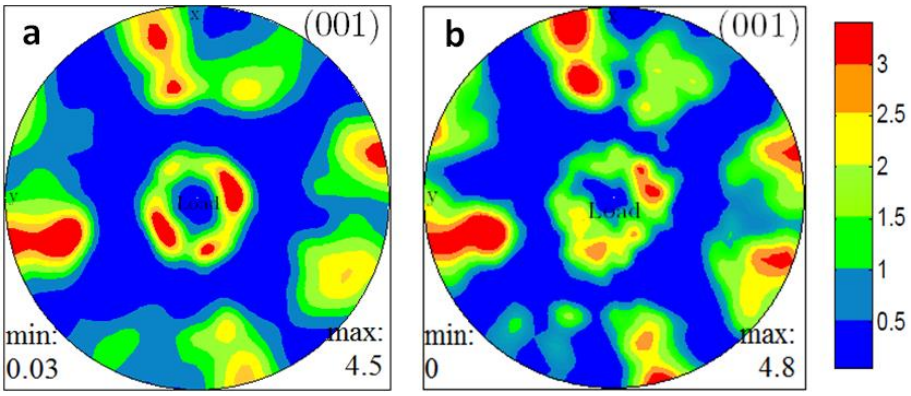

Figure 3.22. Comparison between the pole figure obtained from the EBSD scan (left) and the simulated pole figure (right) generated in the Ti-18 BASCA ABAQUS model using MTEX (Bachmann et al., 2010).

Estimated Parameters

Fully reversed strain-controlled experiments were used for the calibration of the Ti-18 BASCA microstructure response at a strain amplitude of 1.5% and $\dot{\varepsilon} = 10^{-3}\ s^{-1}$. The calibrated values for the Ti-64 β-annealed material (Table 3.8) were used as an initial starting point for the parameter estimation process for Ti-18 BASCA. The process outlined in the estimation of the Ti-64 model parameters was repeated to determine the Ti-18 BASCA calibrated parameters. Most of the selected model parameters were extremely similar to the results for Ti-64 with the chief differences being in the back stress hardening and recovery coefficients. The changes in the parameters likely reflects the effect of the large amount of β-phase in the microstructure (48% volume fraction compared to much lower values in Ti-64), as well as the alpha lath geometry. The estimated parameters for Models 1 and 2 are provided in Table 3.13 and the simulation results for each model are shown in Figure 3.23.

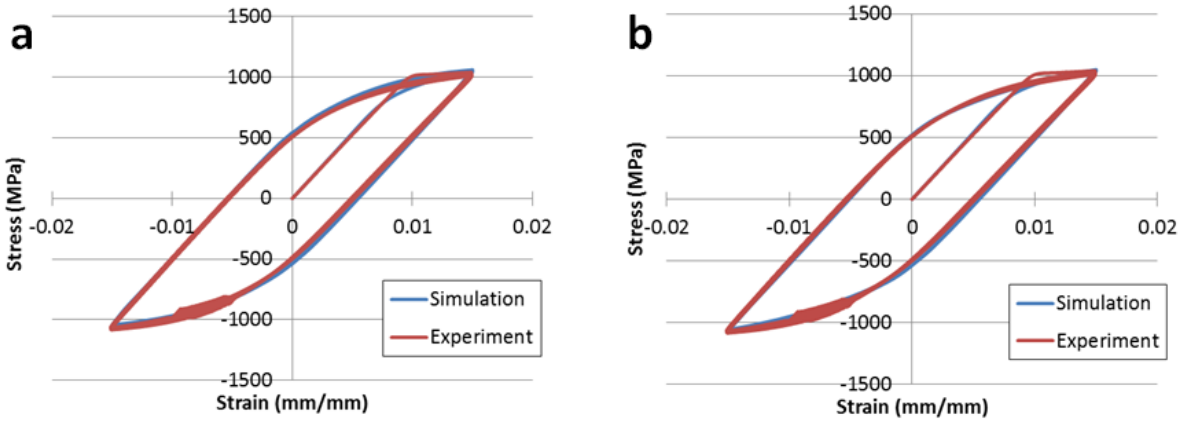

Figure 3.23. Calibrated results for the initial five loading cycles of the Ti-18 STA microstructure at room temperature for the (a) Model 1 and (b) Model 2 for reversed strain-controlled loading with ε_a=1.5% and a strain rate of 10^{-3} s^{-1}.

Table 13. (a) Calibrated Model 1 parameters for Ti-18 STA at room temperature.

$C11$	132,841 MPa	$(\tau_{cr}^{\alpha})_{prism}$	275 MPa	h	60,000 MPa
$C12$	75,255 MPa	$(\tau_{cr}^{\alpha})_{basal}$	300 MPa	h_D	500
$C13$	56,441 MPa	$(\tau_{cr}^{\alpha})_{pyr<a>}$	470 MPa	η	0.3
$C33$	147,810 MPa	$(\tau_{cr}^{\alpha})_{pyr<a+c>}$	570 MPa	d_{α}	146 μm
$C44$	38,200 MPa	$(\kappa_s^{\alpha})_{t=0}$	50 MPa	$d_{\alpha+\beta}$	6.8 μm
		μ	2		

(b) Calibrated Model 2 parameters for Ti-18 STA at room temperature.

$C11$	132,841 MPa	$(s_*^{\alpha})_{prism}$	520 MPa	h^{11}	2500 MPa
$C12$	75,255 MPa	$(s_*^{\alpha})_{basal}$	570 MPa	h_D	166.67
$C13$	56,441 MPa	$(s_*^{\alpha})_{pyr<a>}$	620 MPa	η	0.075
$C33$	147,810 MPa	$(s_*^{\alpha})_{pyr<a+c>}$	1300 MPa	ΔF	3 eV
$C44$	38,200 MPa	$(s_{SRO}^{\alpha})_{max}$	30 MPa	p	0.42
d_{α}	146 μm	k_1	2	q	1.6
IS	6.8 μm				

Validation of Parameter Sets

These model parameter sets for the Ti-18 BASCA microstructure were then validated by comparing simulation results with the experimental data for fully reversed loading, $\dot{\varepsilon} = 5\times10^{-4}\ s^{-1}$, and $\varepsilon_a = 1.3\%$ at room temperature, as shown in Figure 3.25.

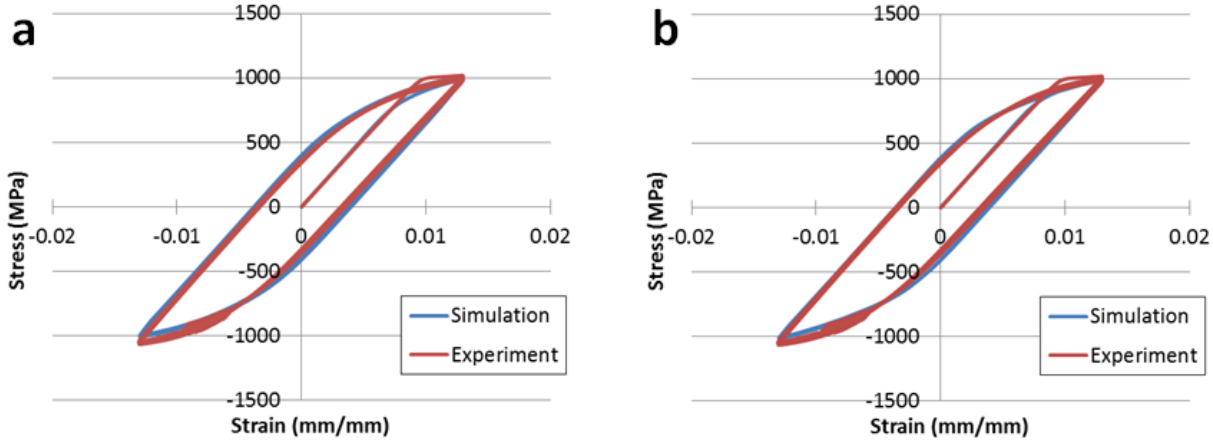

Figure 3.24. Validation of calibrated parameter sets for (a) Model 1 and (b) Model 1 for the room temperature response of Ti-18 BASCA. The displayed data is associated with the initial five cycles of loading for 1.3% strain amplitude and $5\text{x}10^{-4}$ s^{-1} strain rate.

Conclusions

Cyclic deformation experiments have been completed to inform the calibration of two crystal plasticity models for three distinct titanium alloy microstructures: Ti-64 β-annealed, Ti-18 STA, and Ti-18 BASCA at room temperature and 450^{o}C. Polycrystalline finite element (ABAQUS) model geometries were instantiated using an ellipsoidal packing algorithm to fit microstructure statistics acquired from EBSD characterization. The constitutive framework for each of the models has been outlined. A number of the model parameters have been obtained from literature sources. Some are specified as constant for all microstructures considered, while the remaining parameters have been estimated to achieve agreement between the simulated and experimental stress-strain responses for each of the three microstructures. It is noted that the activation enthalpy model (Model 2) has more parameters, but a lower fraction of parameters that vary among microstructures, likely as a consequence of its enhanced physical basis relative to Model 1. Anisotropic elastic constants for each model at each temperature are the same, but differ among models. This is likely attributed to the differences in model structure, in view of the fact that both models represent simplified treatments of deformation mechanisms for these highly complex microstructures.

By spanning such a broad range of Ti alloy microstructures across a broad range of potential service temperatures, this study gives some indication of the level of detail required for validated modeling protocols that support parametric studies for tailoring microstructures to reach target property sets using thermomechanical process route, as is the goal in Integrated Computational Materials Engineering (ICME) (Pollock et al., 2008). For example, these calibrated and validated models will be utilized in future work to estimate the influence of microstructure on computed driving forces for fatigue crack formation and early growth within the microstructure (cf. McDowell, 2009; McDowell and Dunne, 2010; Przybyla and McDowell, 2011).

CHAPTER 4

FATIGUE HOT SPOT SIMULATION FOR TWO WIDMANSTÄTTEN TITANIUM MICROSTRUCTURES

Introduction

The current study is focused on the fatigue performance of the Widmanstätten microstructure for alpha/beta titanium alloys. This structure is achieved by annealing the material above the α-β transus temperature (β-annealed) and selecting an appropriate cooling rate to achieve the desired width of the individual α-phase lamellae grown into the prior β-phase grains. Despite exhibiting a slightly reduced mechanical strength and lower fatigue strength compared to the duplex microstructure, the lamellar morphology is utilized for its superior fracture resistance (Chesnutt et al., 1980; Eylon et al., 1976; Yoder et al., 1977) as well as for its improved formability that can be obtained from optionally deforming the material above the α-β transus temperature (Eylon and Hall, 1977). These properties are ideal for damage tolerant design of complex engineering components in critical applications.

The structure-property relationships for the β-annealed materials have been well characterized by experimental researchers (Eylon et al., 1976; Lin et al., 1984). The primary morphological features identified to strongly affect the fatigue and fracture strength is the size and orientation of the α laths and colonies (Lehr, 1980; Shechtman and Eylon, 1978). Two primary modes of fatigue crack initiation have been observed experimentally. In regions of lower stress intensity, Stubbington and Bowen (1974) found that micro-crack initiation in a Ti-64 β-annealed structures often occurred at α/β interfaces. This phenomenon implies that the high cycle fatigue strength of the structure is increased by reducing the α lath length, leading to nucleation crack sizes (Eylon and Pierce, 1976; Stubbington and Bowen, 1974). More often, cracks have been detected to

form parallel to slip planes that experience intense shear and are not usually aligned with the α/β interface (Eylon and Bania, 1978; Eylon and Hall, 1977; Plumbridge and Stanley, 1986; Shechtman and Eylon, 1978; Stubbington and Bowen, 1974). Though crack initiation has been observed on both basal and prismatic slip planes (Shechtman and Eylon, 1978), the critical crack plane is more often identified to occur on or near the (0001) basal planes (Eylon, 1979; Wojcik et al., 1988), which are known have lower fatigue strength in aggressive environments for titanium, including air (Peters et al., 1980, 1984). Similar to the α/β interfacial cracking, the suggested method for enhancing fatigue resistance is to decrease the size of the colony packets, limiting the extent of slip bands and inhibiting fatigue crack initiation (Eylon and Hall, 1977).

Fatigue crack propagation in the Widmanstätten structure is also sensitive to the mean colony size (Lütjering and Gysler, 1995; Yoder and Eylon, 1979; Yoder et al., 1980). For improved propagation resistance, large colony sizes are necessary to induce a more tortuous crack path. In addition to the colony size, the orientations of the neighboring colonies can have a critical role in crack growth. (Eylon, 1979) has shown that it is possible for neighboring packets to have similarly oriented basal planes through the possible Burgers orientation relationship (BOR) variants of the α laths. Since the basal planes have relatively low fatigue resistance, there is a high likelihood that these planes will form cracks that propagate across neighboring colonies with significantly reduced resistance. The crystallographic texture, which describes the orientation of the basal planes, will inevitably have a role in the fatigue and fracture properties of the material. This texture dependence is illustrated by Peters et al. (1984), who studied the fatigue and fracture properties of highly textured Ti-64 materials possessing a fine equiaxed microstructure. They determined that the crack propagation rate was much higher when the crack path was along the (0001) basal planes.

Although the structure-property relationships for the β-annealed material have been identified, a significant amount of development time and cost is necessary to

experimentally tailor a microstructure for individual component designs to reach target levels of associated properties, e.g., fatigue and fracture strength. With increasing computing power over the past few decades, it has become increasingly feasible to expedite the material design process by utilizing physics-based crystal plasticity models to simulate the material performance of variant microstructures (McDowell and Dunne, 2010; McDowell, 2007). The simulated results can be used to inform the design process and reduce the required number of experiments along with their associated costs. Microstructure-sensitive crystal plasticity models have been employed by many researchers to evaluate the fatigue performance of both nickel-based superalloys (Dunne, Wilkinson, et al., 2007; Przybyla et al., 2010; Shenoy et al., 2007) and duplex α-β titanium (Dunne and Rugg, 2008; Kirane and Ghosh, 2008; Przybyla and McDowell, 2011). Early applications of simulated fatigue studies for bi-modal α-β titanium included the use of a 2D finite element (FE) crystal plasticity model by Goh et al. (2001) to study fretting fatigue behavior of Ti-64. Mayeur (2004) extended this model for 3D FE analysis, which was then utilized by Bridier et al. (2009) to observe slip band evolution in high cycle fatigue loading. (Przybyla, 2010) employed this 3D constitutive framework to simulate fatigue loading of various duplex α-β microstructures and proceeded to compute the fatigue indicator parameters (FIPs) at local hot spots. He coupled the simulated results with extreme value statistics (Gumbel, 1958) and radial correlation functions (Torquato, 2002) to analyze the influence of the phase volume fraction and mean grain size on the calculated FIPs for Ti-64 bi-modal microstructures (Przybyla and McDowell, 2011).

The current study is an extension of Przybyla's work to the investigation of the Widmanstätten titanium microstructures. Analytical methodologies similar to Przybyla and McDowell (2011) were exercised in evaluating the computed FIP dependence on grain size, phase volume fraction, and crystallographic texture for the β-annealed Ti-64 and Ti-18 BASCA alloys. The methodology behind the considered FIPs, marked correlation functions, as well as the microstructure instantiation and simulation

procedures, are outlined in the methodology section. Following the methodology, the simulation outcomes for the Ti-64 microstructures are presented. Next the results for the Ti-18 BASCA microstructures are discussed. Lastly, a summary of the key findings and concluding remarks is included in the Chapter conclusions.

Methodology

Fatigue Indicator Parameters

Three distinct FIPs have been computed to investigate the driving force for fatigue crack initiation and propagation in the β-annealed microstructures. These FIPs are based on localized plastic strain. Initially, the maximum plastic shear strain range (MPSS) is calculated for each cycle. The plastic strain range is determined by subtracting the ratchet strain (difference between plastic strain at the beginning and end of the cycle from the same point of loading) from the plastic strain at the point of maximum loading (Przybyla et al., 2010), i.e.,

$$\left(\Delta\varepsilon_{ij}^{p}\right)_{ratch} = \varepsilon_{ij}^{p}\Big|_{end\ of\ cycle} - \varepsilon_{ij}^{p}\Big|_{beginning\ of\ cycle} \tag{4.1}$$

$$\left(\Delta\varepsilon_{ij}^{p}\right)_{cycle} = \varepsilon_{ij\,\max}^{p}\Big|_{over\ the\ cycle} - \left(\Delta\varepsilon_{ij}^{p}\right)_{ratch} \tag{4.2}$$

The eigenvalue problem is solved for this plastic strain range tensor to find the ordered principal plastic strain ranges and their corresponding directions. Assuming proportional loading, the maximum plastic shear strain range is then identified by

$$\frac{\Delta\gamma^{p}{}_{\max}}{2} = \frac{\left(\Delta\varepsilon^{p}{}_{1}\right)\Big|_{cycle} - \left(\Delta\varepsilon^{p}{}_{3}\right)\Big|_{cycle}}{2}\,. \tag{4.3}$$

The maximum plastic shear strain range on various slip planes are also evaluated as a product of the crystal plasticity simulation which tracks slip on various systems.

Following the identification of the maximum plastic shear strain range, the Fatemi-Socie parameter (Fatemi and Socie, 1988) is then determined. The Fatemi-Socie parameter (FS FIP) correlates to both the crack formation and early Stage I crystallographic fatigue crack growth on critical planes (Castelluccio and McDowell, 2012). The formulation for this parameter is expressed as the following:

$$P_{FS} = \frac{\Delta\gamma^{p}_{\max}}{2}\left(1 + K\frac{\sigma^{n}_{\max}}{\sigma_{y}}\right) \tag{4.4}$$

here, K is a parameter constant denoting the stress dependence and σ_y is the uniaxial yield strength. The peak tensile stress normal to the maximum plastic shear stress plane, σ^{n}_{max}, is obtained by finding the projection of the maximum stress tensor during the maximum loading portion of the cycle onto the unit normal vector n, perpendicular to the critical plane, i.e.,

$$\sigma^{n}_{\max} = \max\big|_{cycle}\left(n_i \sigma_{ij} n_j\right) \tag{4.5}$$

The second calculated parameter is the grain boundary slip impingement FIP proposed by McDowell (2007) to account for cracks forming from the pile-up of dislocations at grain boundaries. This parameter is based on the Fatemi-Socie FIP but employs the net cumulative plastic shear on any plane impinging on a grain boundary segment, and the peak stress normal to this segment is considered, i.e.,

$$P_{IMP} = \gamma^{p}_{net}\left(1 + K_{p}\frac{\sigma^{n}_{GB}}{\sigma_{y}}\right) \tag{4.6}$$

where γ^{p}_{net} is the accumulated plastic shear strain in its maximum direction, K_p is a material parameter, σ^{n}_{GB} and is the peak stress normal to the grain boundary segment.

The final FIP determined in this study is the α/β lamellar interface decohesion parameter (Zhang, 2008), which is tailored for the β-annealed microstructure. This FIP is similar to the Fatemi-Socie parameter, with the exception that the α/β lamellar interface defines the critical plane(s), i.e.,

$$P_{lamellar} = \frac{\Delta\gamma^{p}_{lam}}{2}\left(1 + K_{l}\frac{\sigma^{n}_{lam}}{\sigma_{y}}\right) \tag{4.7}$$

where $\Delta\gamma^{p}_{lam}/2$ is the maximum plastic shear strain range parallel to the lamellar interface and is the stress normal to the interface. All of the investigated FIP values have been determined for nonlocal averaging volumes, including element volumes, grain volumes, and cubic "box" volumes composed of multiple elements. A summary of the calculated FIP values is displayed in Figure 4.1. The parameter constants K, K_p, and K_l have been set to a value of 1 for all calculations of the FIP values.

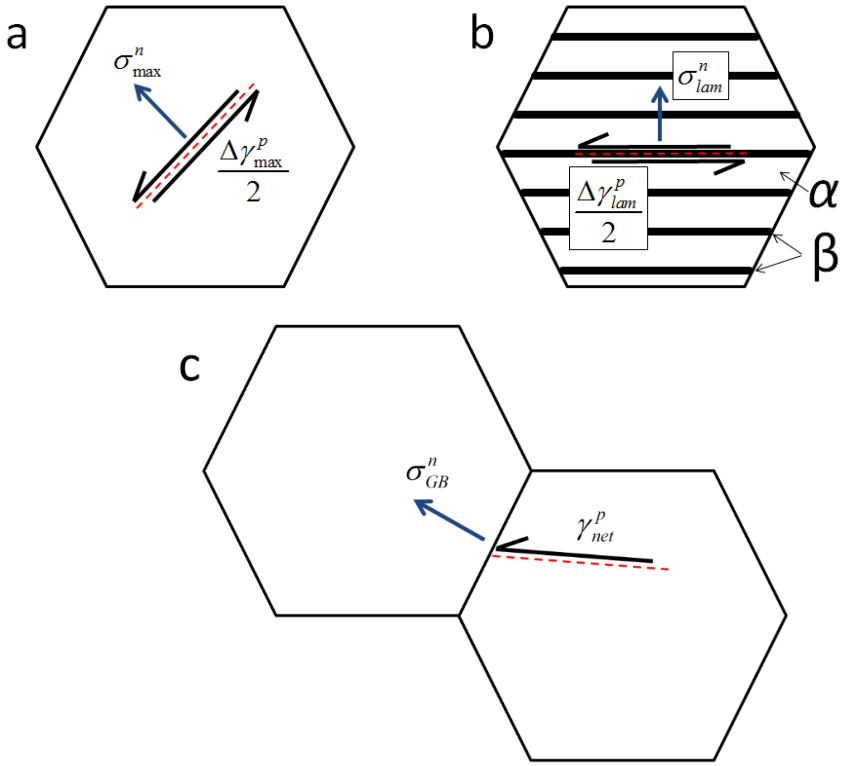

Figure 4.1. Graphical representation of the (a) Fatemi-Socie FIP, (b) Lamellar FIP, and (c) Impingement FIP. Adapted from (Zhang, 2008)

Extreme Value Statistics

The data generated in the fatigue simulations have been utilized to conduct an extreme value distribution analysis for each of the aforementioned FIPs. The calculated FIP values have been fit to a Gumbel (Type I) probability distribution (Gumbel, 1958) which can be expressed as (Haldar, 2000)

$$F_{Y_n}\left(y_n\right) = \exp\left[-e^{-\alpha_n\left(y_n - u_n\right)}\right]. \tag{4.8}$$

Here, $F_{Y_n}\left(y_n\right)$ is the probability that the value Y_n will be less than or equal to y_n, u_n is the characteristic largest value of the sampled population, and α_n is an inverse measure of the dispersion of the largest value of the population. The α_n and u_n parameters can be explicitly evaluated by finding the linear regression fit between the linearized probability function and the corresponding largest values for the volume averaged FIPs over numerous simulation results. The linearization of the Gumbel probability distribution is accomplished through the following approach:

$$F_{Y_n}\left(y_n\right) = p = \exp\left[-e^{-\alpha_n\left(y_n - u_n\right)}\right] \tag{4.9}$$

$$\ln\left(1/p\right) = e^{-\alpha_n\left(y_n - u_n\right)} \tag{4.10}$$

$$\ln\left(1/\ln\left(1/p\right)\right) = \alpha_n\left(y_n - u_n\right) \tag{4.11}$$

Here, we have a linear relationship between the LHS of Eq. 4.11 and y_n. The value of p is estimated for the rank ordered maximum FIP values by

$$p = \frac{i - 0.3}{n + 0.4} \tag{4.12}$$

where n is the population size and i is rank of the maximum FIP value (numbered from smallest to largest). For each nominal microstructure, the extreme value distribution is constructed from sampling the maximum value for each of a large number of realizations or statistical volume elements (SVEs) of polycrystals, as explained by Przybyla and

McDowell (2011) and Przybyla (2010). These statistics are utilized to compare the trends in minimum fatigue life (low probability of failure) performance among several different nominal microstructures.

Radial Correlation Functions

A radial correlation post-processing package developed by Przybyla (2010) has been employed to examine the proximity of grains with favorably aligned slip systems via comparison of their Schmid factors (Przybyla and McDowell, 2011). The definition of a radial correlation function is such that $R(\beta,\beta'|r)$ is the probability of an attribute β having a second attribute β' within a distance between r and $r + dr$ in any direction (Torquato, 2002). The radial correlation function for the complete structure has been compared to the correlation function for the extreme value locations by employing a marked extreme value marked correlation function algorithm created by Przybyla and McDowell (2011). The data generated from the marked correlation function are compared to the total radial correlation function results to observe the favorably oriented slip systems present at the extreme value locations. Figure 4.2 depicts a schematic of the radial correlation function.

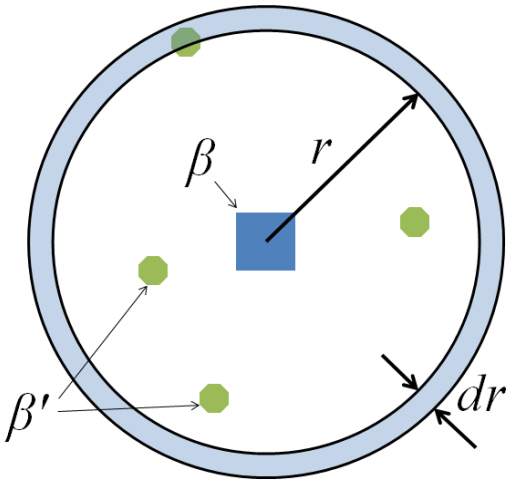

Figure 4.2. Radial correlation function, *R*, is the probability of finding an attribute β and another attribute β' within a distance of *r* to *r* + *dr* in any direction from the first attribute β (Torquato, 2002). Adapted from (Przybyla, 2010).

Statistical Volume Element Generation

An ellipsoidal packing algorithm (Przybyla and McDowell, 2011) has been exploited to build polycrystalline ABAQUS models of statistical volume elements, ensembles of grains/phases that are sufficiently large to encompass relevant nearest and second nearest neighbor effects but too small to be considered as a representative volume element. The algorithm works by randomly placing undersized ellipsoids representative of crystalline grains into an empty 3D space until a defined volume packing fraction has been reached. The ellipsoids are then allowed to grow uniformly until the remainder of the empty space has been filled. The grain sizes are estimated by $d_{grn} = 0.7\left(V_{grn}\right)^{1/3}$ (Horálek, 1990) and the input parameters for the algorithm are iterated to gain a good fit between the estimated and desired grain size distributions. An example microstructure and grain size distribution is displayed in Figure 4.3. After the polycrystalline model had been created, the orientation distribution of the grains was defined by simulating the appropriate pole figure with a free MATLAB (2011) plug-in: MTEX (Bachmann et al., 2010). Pole figures for each of our investigated materials have been acquired from EBSD scan data provided by EBSD Analytical Inc. (Lehi, UT) and are utilized when defining the texture of each instantiated microstructure. Exemplary scanned and simulated pole figure fits for the Ti-64 β-annealed material and the Ti-18 microstructure are included in Figures 4.4 and 4.5, respectively.

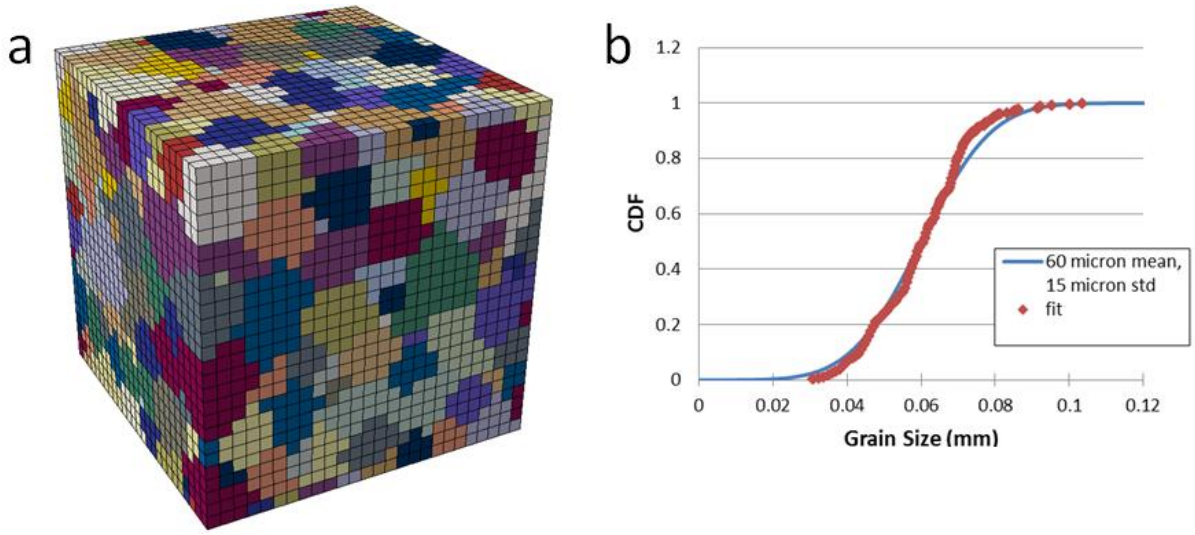

Figure 4.3. (a) ABAQUS geometry generated via ellipsoidal packing algorithm and (b) grain size distribution fit.

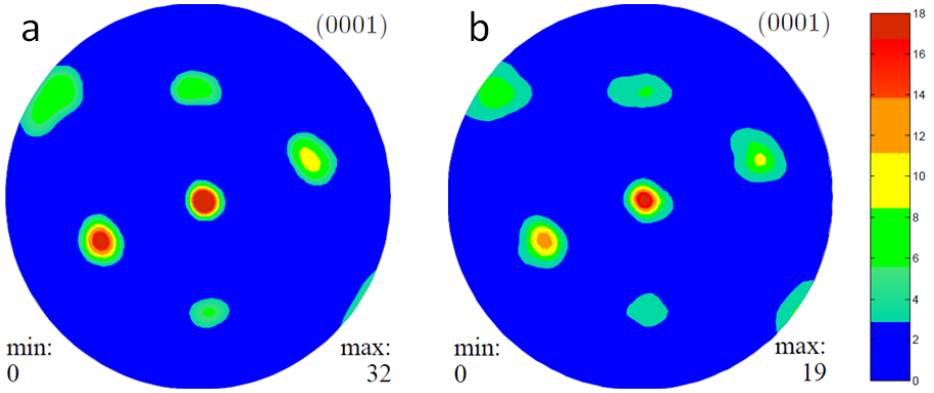

Figure 4.4. (a) (0001) pole figure obtained from an EBSD scan and (b) the simulated (0001) pole figure generated in the ABAQUS model with MTEX (Bachmann et al., 2010) for the Ti-64 β-annealed material.

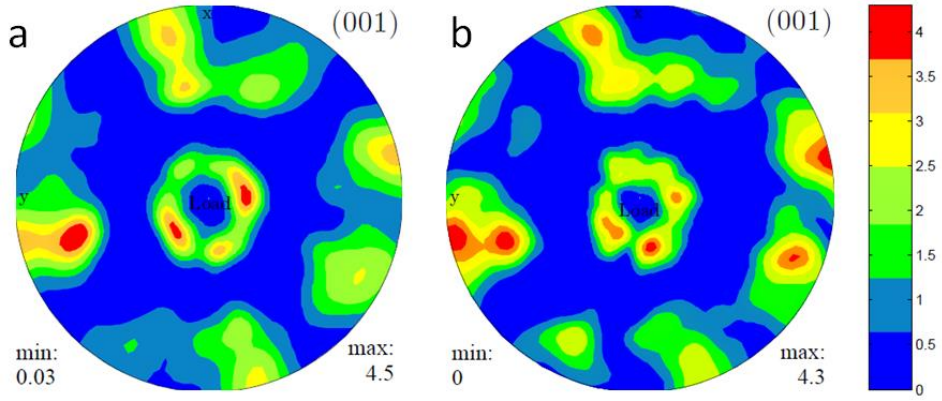

Figure 4.5. (a) (001) pole figure obtained from an EBSD scan and (b) the simulated (001) pole figure generated in the ABAQUS model with MTEX (Bachmann et al., 2010) for the Ti-18 BASCA material.

Once the polycrystalline geometry and orientation distribution have been defined, the disorientation distribution function (DDF) between neighboring grains is optimized. This is accomplished by randomly switching grain orientations within the microstructure model and comparing the computed error between the new disorientation distribution and the observed DDF from the EBSD scan information. The switched grain orientation definition is accepted if the overall error is reduced. This allows for an optimal DDF to be achieved while retaining the overall texture of the model. Figure 4.6 displays typical DDF results for the two alloys.

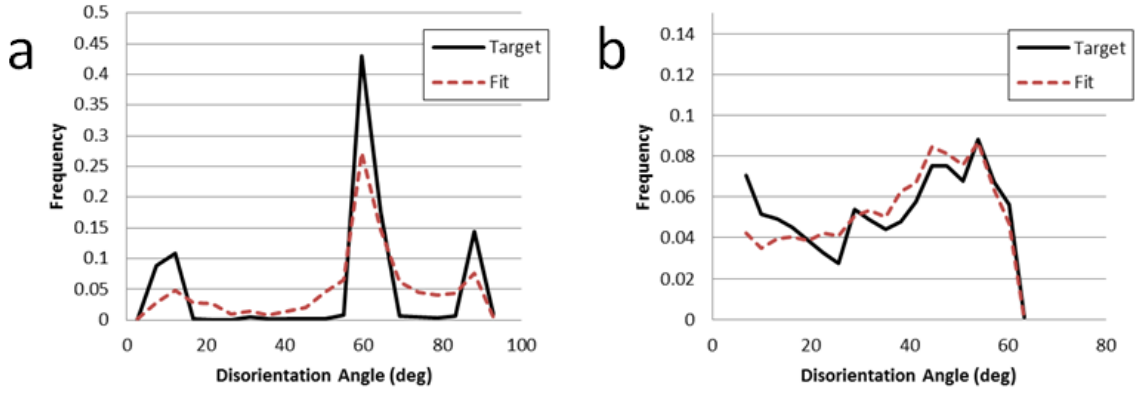

Figure 4.6. Disorientation distribution fit results for the (a) Ti-64 β-annealed microstructure and the (b) Ti-18 BASCA structure.

Ti-6Al-4V β-annealed Fatigue Simulation Results

The selected attributes for the simulated Ti-64 β-annealed alloy microstructures are shown below in Table 4.1. These microstructures allow for parametric investigation of the fatigue parameter dependence on three influential characteristics: the mean colony size (micros A and B), crystallographic texture (micros B through D), and phase volume fraction (micros B and E). Example pole figures for the transverse and basal textures are shown in Figure 4.7. The ABAQUS model side length for microstructures B through E is 0.6 mm, while the size for microstructure A was selected to be 1.2 mm to accommodate a sufficient number of the larger grains. Each of the instantiated structures contains 17,576

C3D8R elements and is strained at $2x10^{-3}$ s^{-1} strain rate with fully reversed loading, R = -1, and a strain amplitude of ε_a = 0.5%. This strain amplitude corresponds with approximately 75% of the macroscopic polycrystal yield strain: ε_y = 0.67%. Periodic boundary conditions (Przybyla, 2010) have been imposed in all directions for the instantiated voxellated polycrystals. After the initial three cycles of simulated loading, the magnitude of the plastic strain range utilized in the FIP calculations (Equation 4.3) had reached a nearly cyclically stable value. Hence, all of the polycrystals were simulated for simply three cycles before computing the maximum FIPs to minimize the simulation time. One hundred realizations (SVEs) of each microstructure have been simulated using a previously calibrated crystal plasticity algorithm based on a Kocks-type flow rule (Kocks et al., 1975) and the computed FIPs have been determined to achieve convergence to the Gumbel extreme value distribution. The calculation of the FIP values is directly related to the simulated irreversible strain on crystallographic slip planes; consequently, the magnitudes of the computed FIPs will be dependent on the slip planes defined for different crystal structures. As long as the same phases are present, then comparison among the variant microstructures containing the same phases is sensible even though the phases could be distributed differently. The comparison of the simulated FIP distributions indicating the grain size dependence, texture dependence, and phase volume fraction effects for all of the microstructures can be referenced in Figures 4.8, 4.9, and 4.10, respectively.

Table 4.1: Simulated microstructures for the Ti-64 β-annealed material

	Grain Size (μm)							
Micro.	α + β (μ)	α + β (σ)	α (μ)	α (σ)	Simulated Texture	Colony volume fraction	Number of grains	Elements per grain
A	160	40	--	--	EBSD Scan	100%	140	125
B	60	15	--	--	EBSD Scan	100%	301	59
C	60	15	--	--	Basal	100%	301	59
D	60	15	--	--	Transverse	100%	301	59
E	60	15	60	15	EBSD Scan	50%	300	59

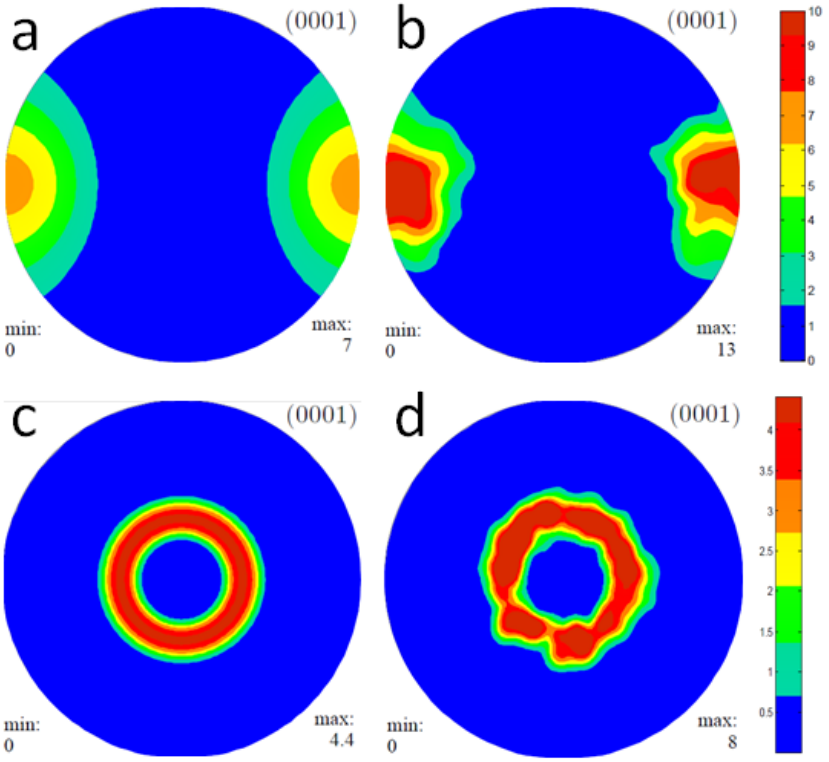

Figure 4.7. Pole figures for (a) transverse texture target, (b) simulated transverse texture, (c) basal texture target, and (d) simulated basal texture generated via MTEX (Bachmann et al., 2010).

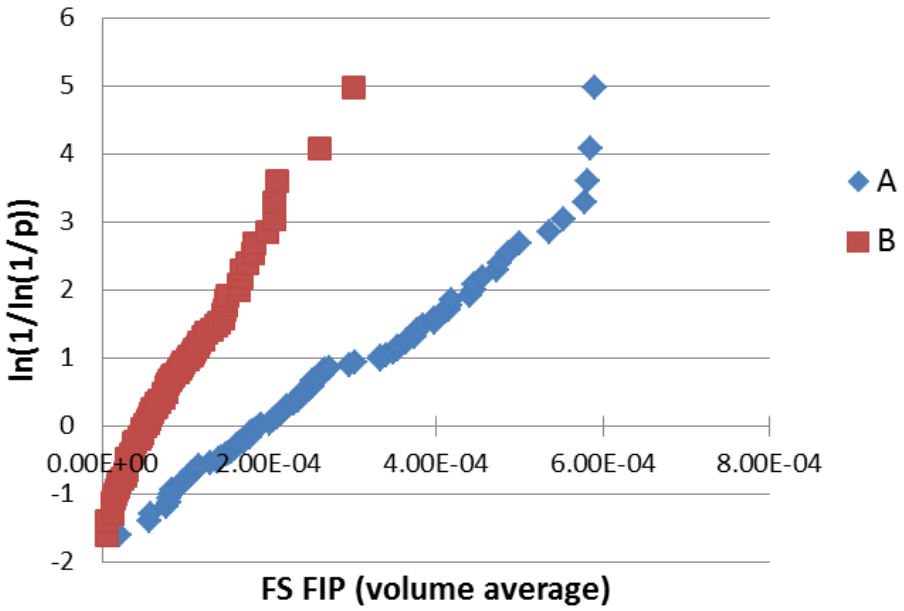

Figure 4.8. Ti-64 β-annealed FIP distributions indicating the grain size dependence of the Fatemi-Socie FIP averaged over 65 μm equivalent grain volumes.

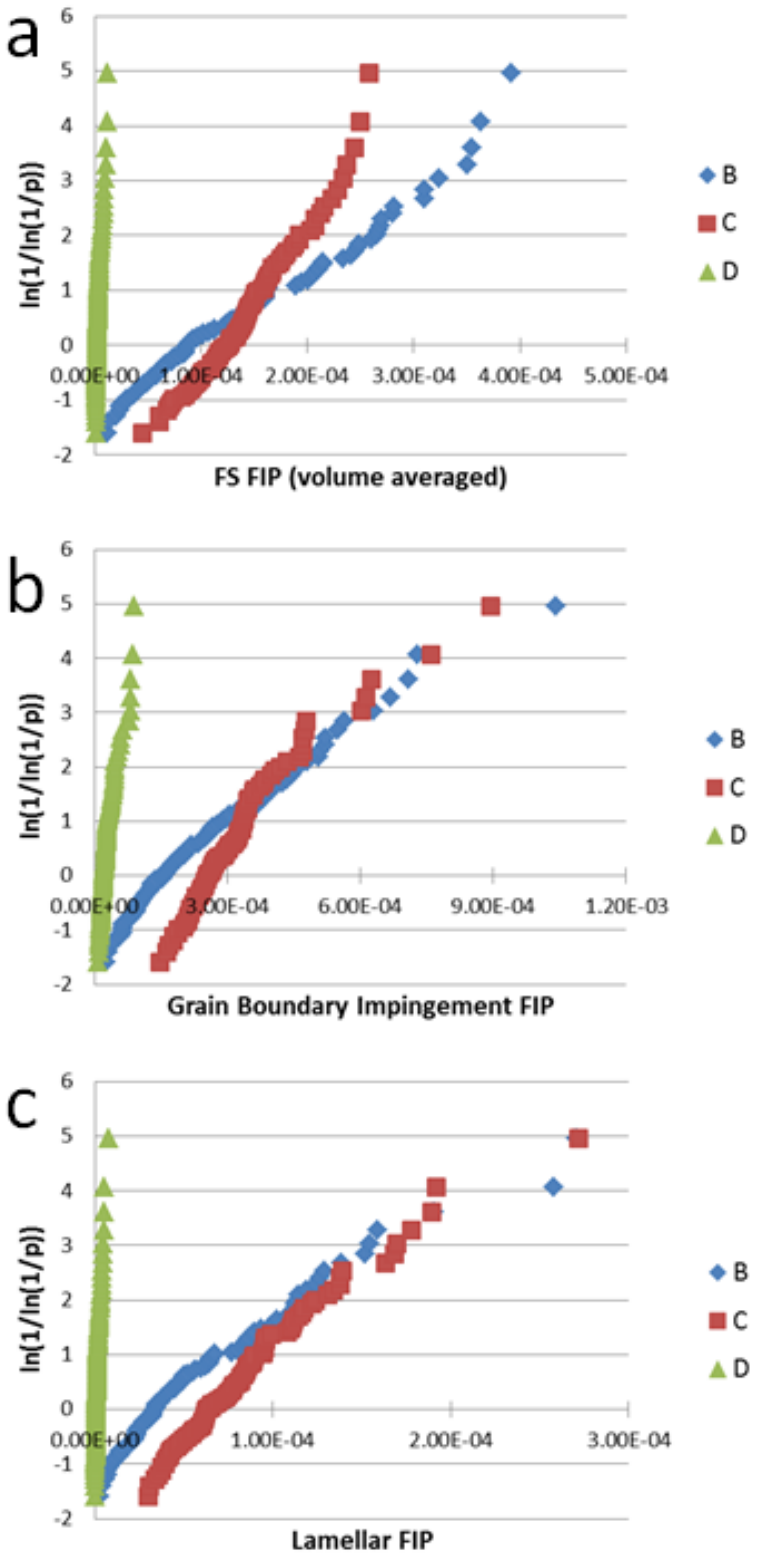

Figure 4.9. Ti-64 β-annealed FIP distributions indicating the texture dependence of the (a) Fatemi-Socie FIP, (b) grain boundary impingement FIP, and (c) lamellar FIP averaged over 48 μm equivalent grain volumes, grain boundary interfaces, and grain volumes, respectively.

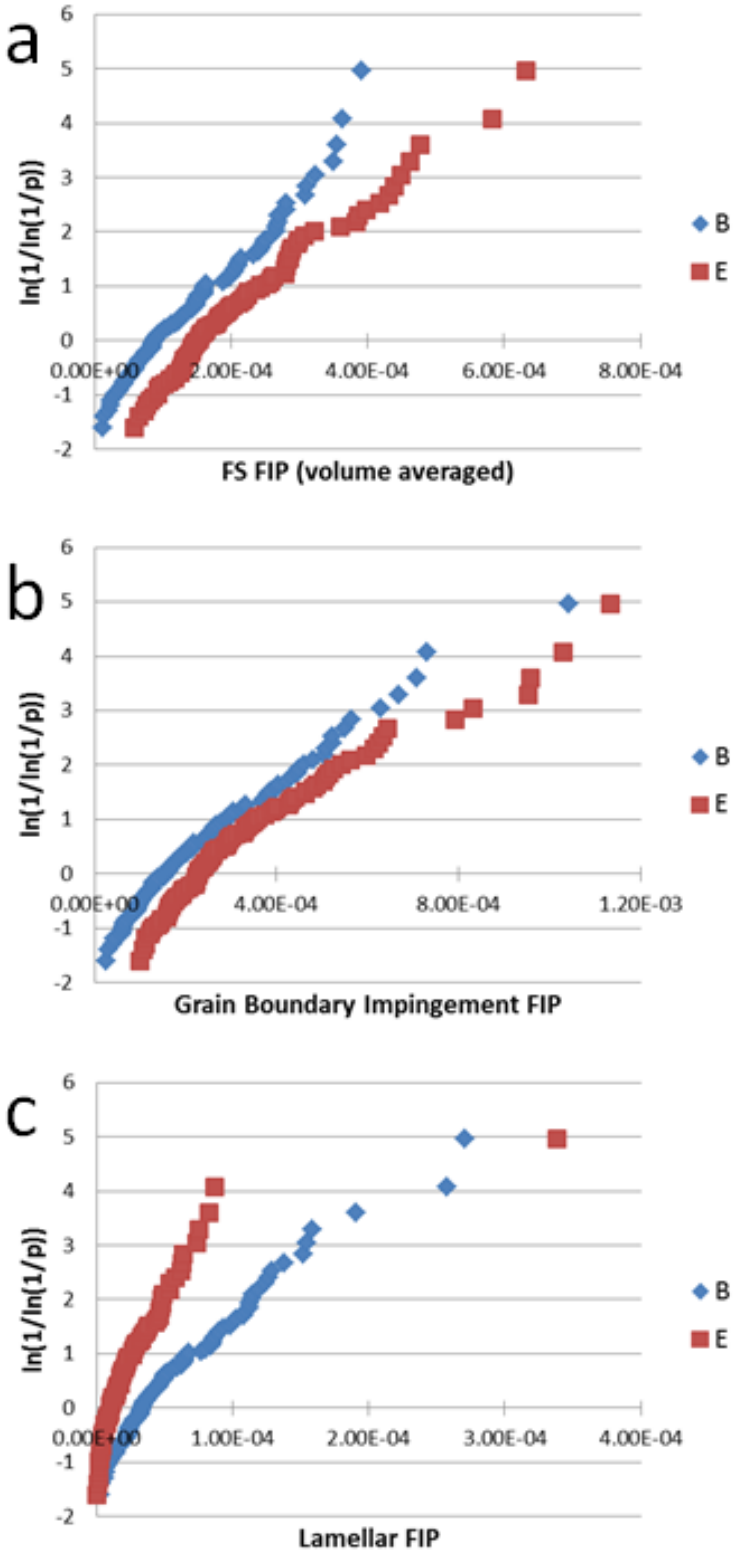

Figure 4.10. Ti-64 β-annealed FIP distributions indicating the phase volume fraction dependence of the (a) Fatemi-Socie FIP, (b) grain boundary impingement FIP, and (c) lamellar FIP averaged over 48 μm equivalent grain volumes, grain boundary interfaces, and grain volumes, respectively.

Table 4.2: Gumbel distribution linear fit statistics for Fatemi-Socie FIP averaged over 48 μm equivalent grain volumes for the β-annealed Ti-6Al-4V material simulations. (*65 μm grain volume averaged as depicted in Fig. 8)

Micro.	α_n	u_n	$(\alpha_n)^{-1}/u_n$	R^2
A*	8.796×10^{3}	1.963×10^{-4}	0.58	0.9727
B*	2.068×10^{4}	5.659×10^{-5}	0.85	0.9868
B	1.361×10^{4}	9.887×10^{-5}	0.74	0.9813
C	2.767×10^{4}	1.206×10^{-4}	0.30	0.9795
D	4.870×10^{5}	2.561×10^{-6}	0.80	0.9349
E	1.097×10^{4}	1.602×10^{-4}	0.57	0.9782

Table 4.3: Grain boundary impingement FIP Gumbel distribution fit statistics for β-annealed Ti-6Al-4V material simulations.

Micro.	α_n	u_n	$(\alpha_n)^{-1}/u_n$	R^2
B	6.806×10^{3}	1.673×10^{-4}	0.88	0.9757
C	1.011×10^{4}	2.570×10^{-4}	0.39	0.9345
D	6.778×10^{4}	2.247×10^{-5}	0.66	0.9367
E	5.839×10^{3}	2.358×10^{-4}	0.73	0.9489

Table 4.4: Lamellar FIP Gumbel distribution fit statistics for β-annealed Ti-6Al-4V material simulations.

Micro.	α_n	u_n	$(\alpha_n)^{-1}/u_n$	R^2
B	2.434×10^{4}	3.692×10^{-5}	1.11	0.9564
C	3.042×10^{4}	6.529×10^{-5}	0.50	0.9705
D	8.608×10^{5}	1.106×10^{-6}	1.05	0.9238
E	5.644×10^{4}	1.263×10^{-5}	1.40	0.9522

Trends for the simulated FIP distribution results agree with experimentally observed trends in fatigue severity as a function of grain size. The determined distribution for microstructure A, having an average grain size of 160 μm, has a much larger characteristic maximum value (u_n) of 1.963×10^{-4} compared to the characteristic value for microstructure B: 5.659×10^{-5}. These computed distributions clearly show that the larger grain size will have higher extreme values for the Fatemi-Socie FIP value, suggesting increased sensitivity to crack formation and early propagation. This finding is consistent with experimental works (Eylon and Hall, 1977; Eylon et al., 1976) which

have shown that cracks form along intense shear bands across the larger colony grains. In addition, Przybyla and McDowell (2011) simulated FIP distributions for coarse bi-modal Ti-64 microstructures also exhibit larger FIP values compared to fine bimodal structures.

All of the computed FIP distributions reveal the same trend in terms of FIP dependence on crystallographic texture. The highest resistance (lowest FIPs) to fatigue crack initiation was observed for the transverse textured microstructures, followed by the basal textured assemblies. The texture fit to the experimental EBSD scan pole figure was identified to most likely have the lowest fatigue life. The relationship between the transverse and basal textures agrees with experimentally observed fatigue trends from Peters et al. (1984), who investigated fine equiaxed Ti-64 microstructures. Peters et al. (1984) determined that transverse textured materials were able to withstand slightly higher stress amplitudes in high cycle fatigue when loading normal to the HCP crystal c-axis (rolling direction) in comparison to loading along the c-axis (transverse direction). This variation in HCF performance is attributed to the orientation of the critical (0001) basal planes (Eylon, 1979; Peters et al., 1984; Shechtman and Eylon, 1978; Wojcik et al., 1988), which often correlates with fatigue crack initiation.

The phase volume fraction effects observed in the FIP distributions are consistent with the simulated results from Przybyla and McDowell (2011). The Fatemi-Socie and grain boundary impingement FIP values for microstructure E (duplex structure) are consistently larger than those of microstructure B (fully lamellar), which implies that the elimination or reduction of the α-phase would be advantageous for fatigue performance. The lamellar FIP distributions exhibit the opposite trend in FIP values; however, the lower FIP values for microstructure E are perhaps not surprising as the magnitude of the lamellar FIP is defined to be zero for the α-phase grains.

Each of the instantiated microstructures have also been analyzed via marked radial correlation functions (Przybyla, 2010). The correlation between favorably oriented slip planes and the extreme value locations within the structure are identified through the

evaluation of the apparent Schmid factors for each of the crystallographic slip planes. The apparent Schmid factor is merely the applied shear stress on the investigated plane divided by the macroscopic applied stress. The extreme values are based on the Fatemi-Socie FIP averaged over 48 μm equivalent grain size volumes for micros. B through D, while the averaging volume is equivalent to a 65 μm grain size for microstructure A. Radial correlation results depicting the most frequently observed extreme value planes are presented in Figures 4.11 – 4.15.

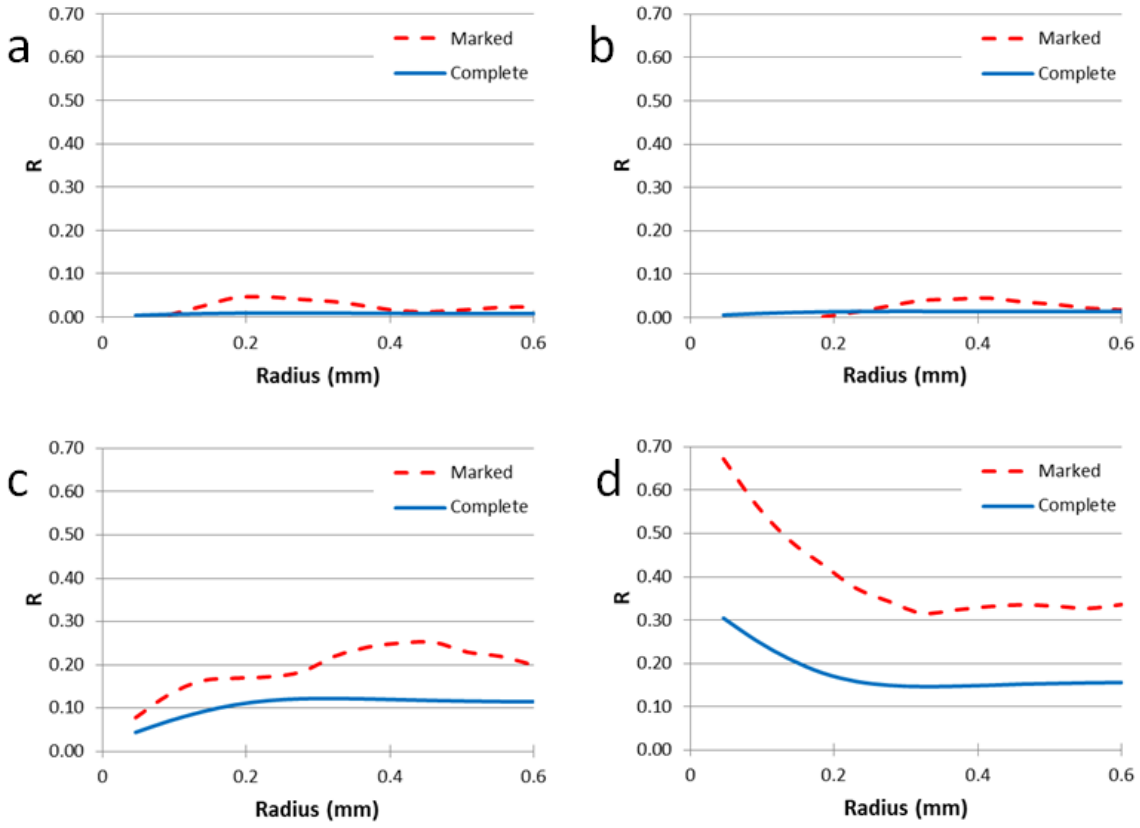

Figure 4.11. Ti-64 β-annealed microstructure A radial correlation functions describing the correlation between the apparent Schmid factors for $\langle 111 \rangle \{110\}$ BCC slip between 0.45 and 0.5 for the α + β colonies and the apparent Schmid factors between 0.45 and 0.5 for (a) basal slip, (b) prismatic slip, (c) pyramidal $\langle a \rangle$ slip, and (d) $\langle 111 \rangle \{110\}$ BCC slip.

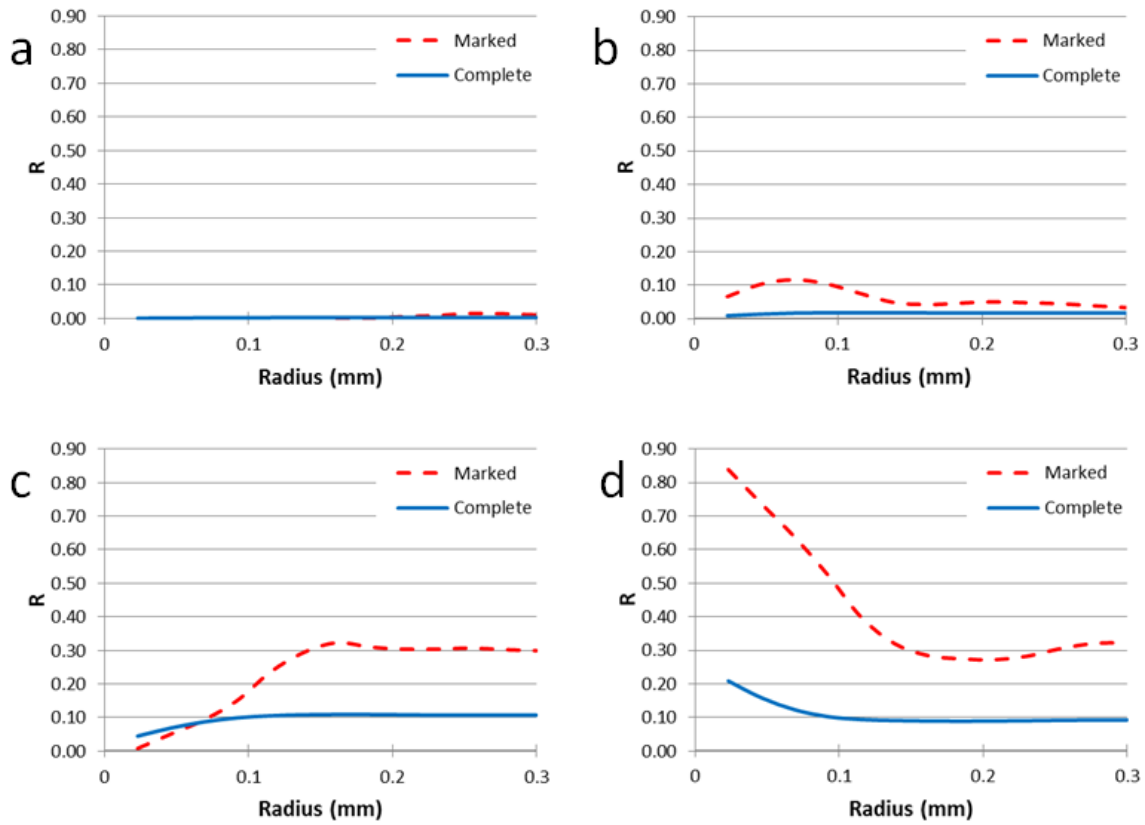

Figure 4.12. Ti-64 β-annealed microstructure B radial correlation functions describing the correlation between the apparent Schmid factors for $\langle 111 \rangle \{110\}$ BCC slip between 0.45 and 0.5 for the α + β colonies and the apparent Schmid factors between 0.45 and 0.5 for (a) basal slip, (b) prismatic slip, (c) pyramidal $\langle a \rangle$ slip, and (d) $\langle 111 \rangle \{110\}$ BCC slip

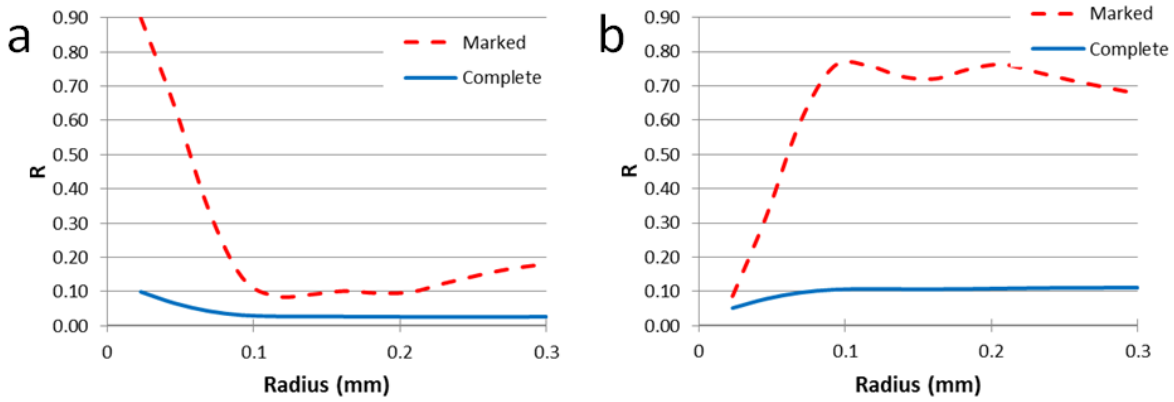

Figure 4.13. Ti-64 β-annealed microstructure C radial correlation functions describing the correlation between the apparent Schmid factors for basal slip between 0.45 and 0.5 for the α + β colony grains and the apparent Schmid factors between 0.45 and 0.5 for (a) basal slip and (b) $\langle 111 \rangle \{110\}$ BCC slip.

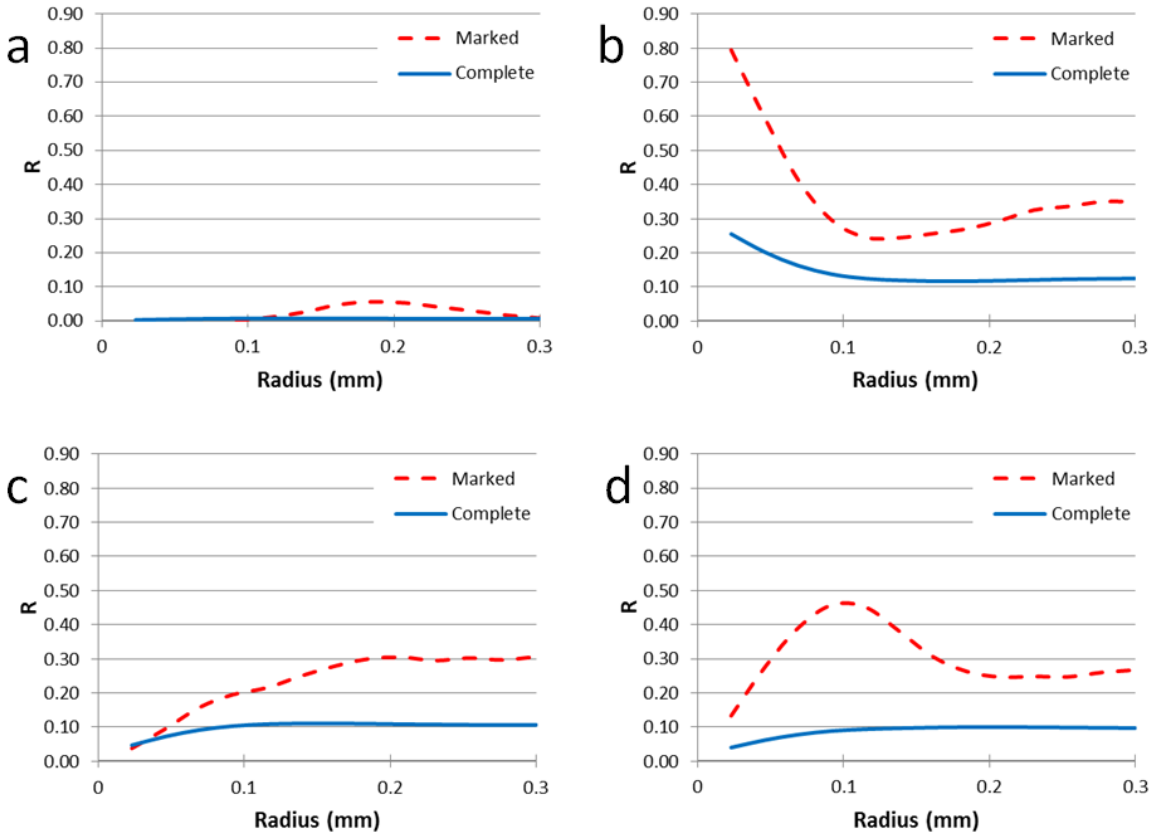

Figure 4.14. Ti-64 β-annealed microstructure D radial correlation functions describing the correlation between the apparent Schmid factors for prismatic slip between 0.45 and 0.5 for the α + β colony grains and the apparent Schmid factors between 0.45 and 0.5 for (a) basal slip, (b) prismatic slip, (c) pyramidal, and (d) $\langle 111 \rangle \{110\}$ BCC slip.

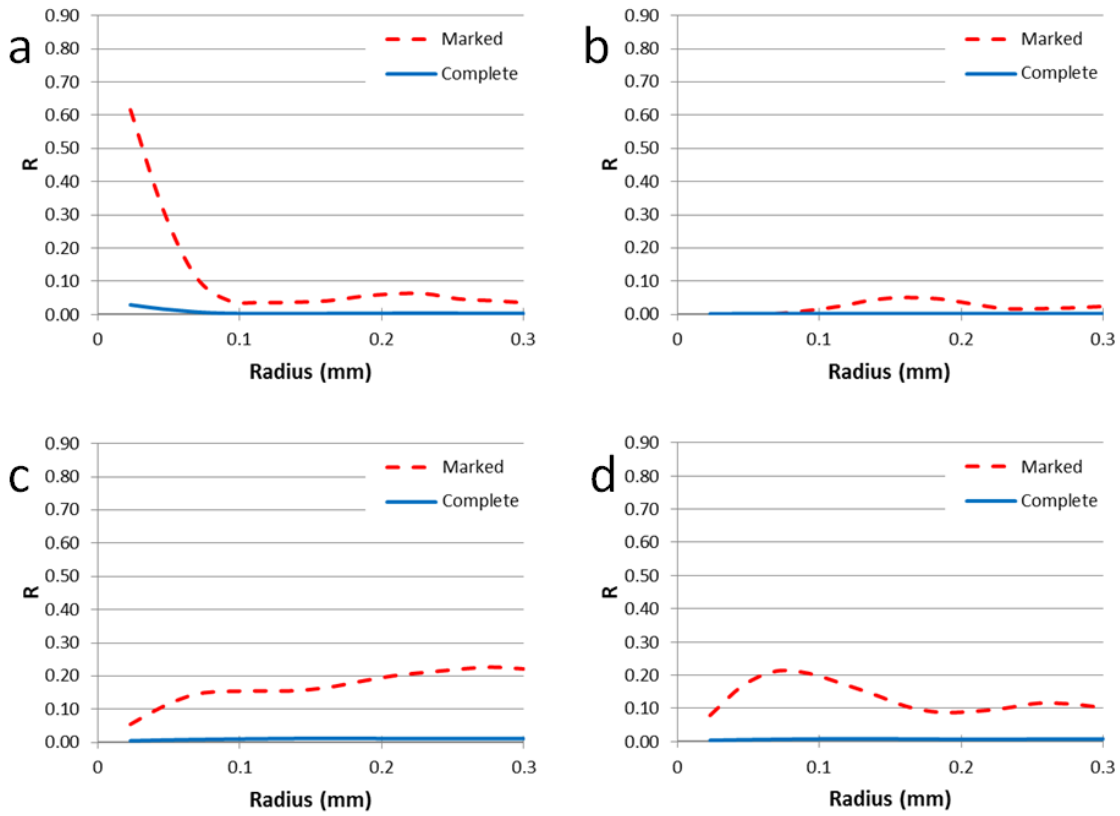

Figure 4.15. Ti-64 β-annealed microstructure E radial correlation functions describing the correlation between the apparent Schmid factors for basal slip between 0.45 and 0.5 for the α-phase grains and the apparent Schmid factors between 0.45 and 0.5 for (a) basal slip, (b) prismatic slip, (c) pyramidal, and (d) pyramidal $\langle a+c \rangle$ slip.

The dashed lines in the Figures 4.11 – 4.15 represent the radial correlation function results at the extreme value location in the model, while the solid lines illustrate the radial correlation averaged over the entire polycrystal. Each line portrays the frequency of a particular phase and slip system having a high apparent Schmid factor (0.45 – 0.5) and present at a distance *r* from the investigated extreme value slip plane. These lines are shown together to observe the prevalent conditions present near the localized fatigue hot spots. The typical correlation results for microstructure C (Figure 4.13) reveal that grains at the extreme value FIP locations are commonly oriented for easy basal slip. This outcome is consistent with previous experimental works for β-annealed titanium (Eylon, 1979; Shechtman and Eylon, 1978; Wojcik et al., 1988), which

have found that crack initiation and propagation frequently occur on basal planes in the lamellar colonies. The results for microstructure E, a duplex structure, shows that α-phase grains positioned for easy basal slip is also regularly present at the extreme value locations. This observation for the duplex α + β Ti structure is in agreement with experimental studies by Bridier et al. (2008) as well as simulated fatigue studies by Przybyla and McDowell (2011). In contrast, the correlation findings for microstructure D (Figure 4.13) show that grains oriented for easy prismatic slip are normally located at the extreme FIP sites. This deviation in the critical slip plane is not surprising as microstructure D possesses a transverse texture, which strongly favors prismatic slip. The simulated extreme FIP locations for microstructures A and B coincided with grains favorably oriented for $\langle 111 \rangle \{110\}$ BCC slip. The $\langle 111 \rangle \{110\}$ BCC slip directions have been defined with respect to the local HCP lattice frame to be compliant with the burgers orientation relationship (Ankem and Margolin, 1980): $(0001)_\alpha \parallel \{110\}_\beta$ and $\langle 11\bar{2}0 \rangle_\alpha \parallel \langle 111 \rangle_\beta$. When the BCC slip systems are favored, the grains are known to be oriented for hard slip.

The correlation statistics for C, D, and E show that the extreme value FIP locations are positioned nearby grains that are oriented for easy BCC slip. This situation is most clearly observed in Figure 4.13 and it indicates that the critical locations within the microstructure are typically found at grains experiencing soft slip adjacent to grains oriented for hard slip. This hard-soft grain interface has been shown to induce significant stress localization and plasticity intensification (Dunne, Rugg, et al., 2007; Hasija et al., 2003; Venkataramani et al., 2006). This phenomenon rationalizes the observed radial correlation results, which are also in agreement with Przybyla and McDowell's (2011) findings for duplex structures.

Ti-18 BASCA Fatigue Simulation Results

The simulated Ti-18 BASCA alloy microstructure characteristics are displayed in Table 4.5. Similar to the Ti-64 study, the selected voxellated structures gained an evaluation of the fatigue trends for the following characteristics: the mean colony size (micros A and B), texture (micros B through D), and phase volume fraction (micros B and E). Periodic boundary conditions have been defined for the ABAQUS models, and the model side lengths for microstructures B, C, D, and E were 0.6 mm, while the side length of microstructure A was 1.2 mm. All of the structures were strained at an amplitude of ε_a = 0.6%, which corresponds to 75% of the simulated yield strain of ε_y = 0.8%. Fully reversed loading at $2x10^{-3}$ s^{-1} strain rate is imposed onto the instantiated microstructures, each containing 17,576 C3D8R elements. One hundred simulations for each structure have been completed and the extreme value FIPs have been found to have an acceptable fit to the Gumbel distribution. The grain size dependence, texture dependence, and phase volume fraction effects on the extreme value FIP distributions appear in Figures 4.16, 4.17, and 4.18.

Table 4.5: Microstructures for Ti-18 BASCA fatigue study

	Grain Size (μm)							
Micro.	α + β (μ)	α + β (σ)	α (μ)	α (σ)	Simulated Texture	Colony volume fraction	Number of grains	Elements per grain
A	146	25	--	--	EBSD Scan	100%	171	102
B	60	15	--	--	EBSD Scan	100%	301	59
C	60	15	--	--	Basal	100%	301	59
D	60	15	--	--	Transverse	100%	301	59
E	60	15	60	15	EBSD Scan	50%	300	59

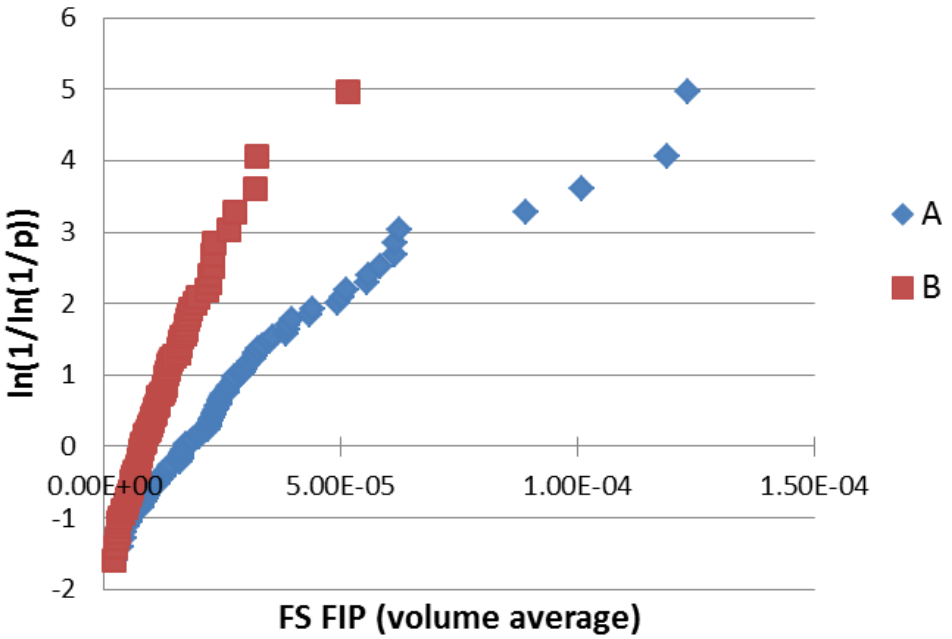

Figure 4.16. Ti-18 BASCA FIP distributions indicating the grain size dependence of the calculated extreme value Fatemi-Socie FIP averaged over 65 μm equivalent size grain volumes.

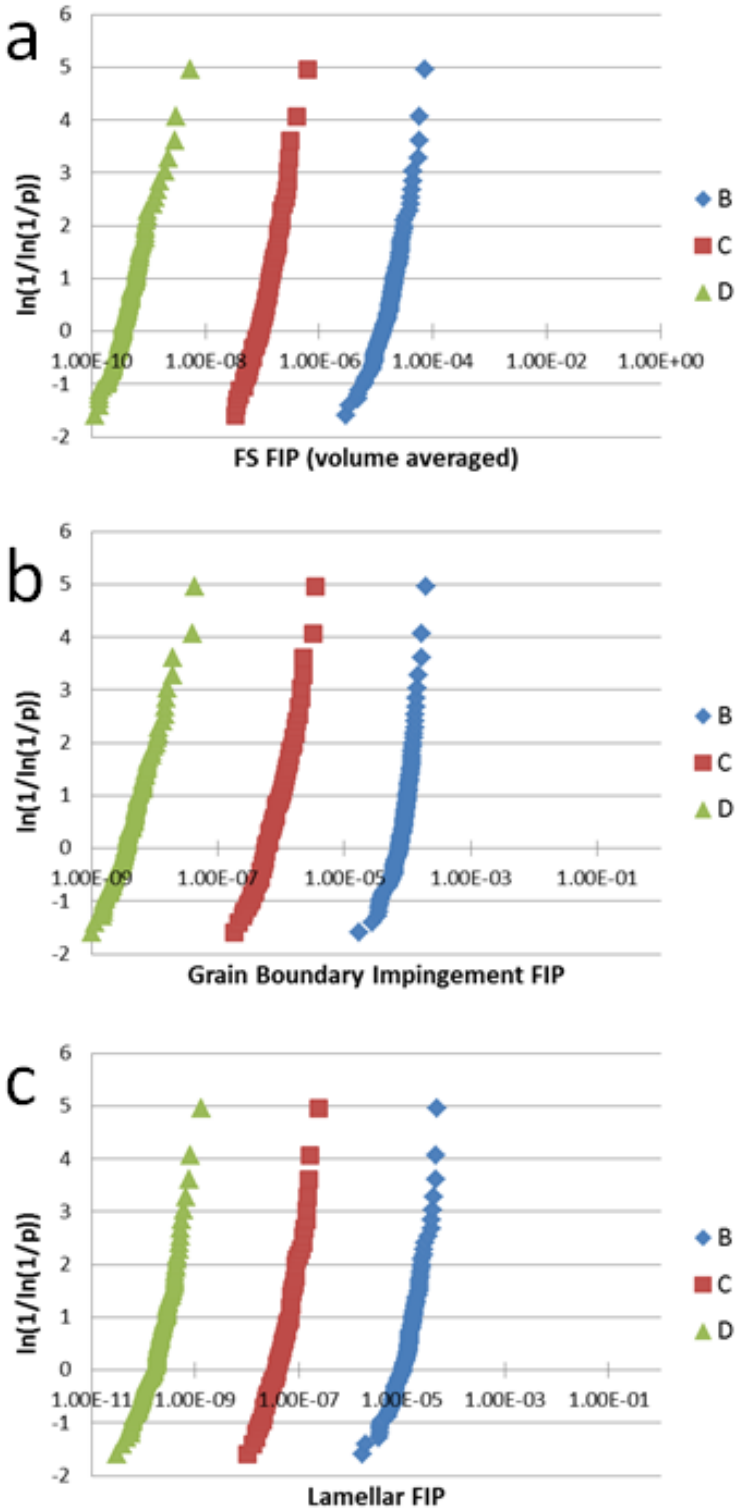

Figure 4.17. Ti-18 BASCA FIP distributions indicating texture dependence of the (a) Fatemi-Socie FIP, (b) grain boundary impingement FIP, and (c) lamellar FIP averaged over 48 μm equivalent grain volumes, grain boundary interfaces, and grain volumes, respectively.

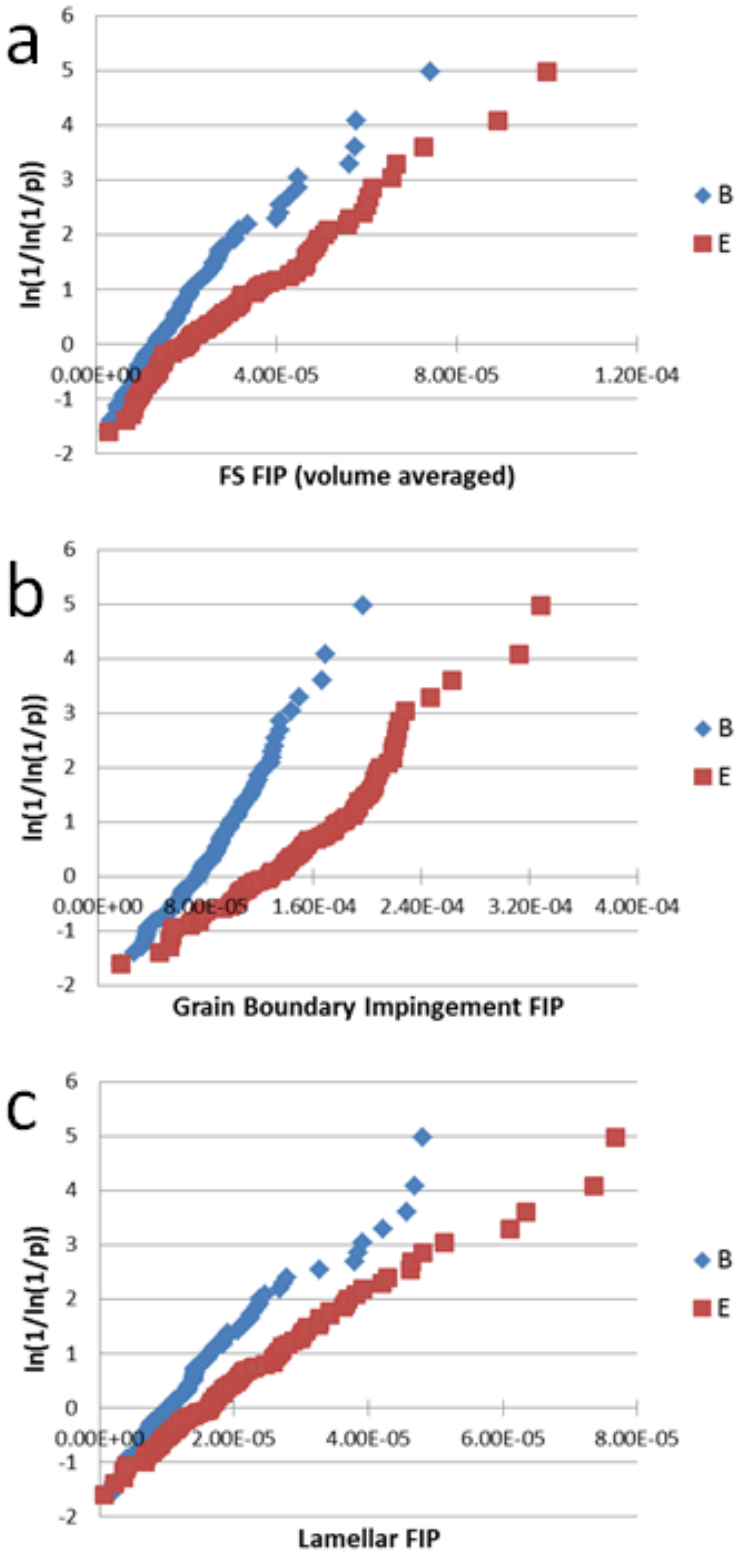

Figure 4.18. Ti-18 BASCA FIP distributions indicating phase volume fraction dependence of the (a) Fatemi-Socie FIP, (b) grain boundary impingement FIP, and (c) lamellar FIP averaged over 48 μm equivalent grain volumes, grain boundary interfaces, and grain volumes, respectively.

Table 4.6: Gumbel distribution linear fit statistics for Fatemi-Socie FIP averaged over 48 μm equivalent grain volumes for the Ti-18 BASCA material simulations. (*65 μm grain volume averaged as depicted in Fig. 16)

Micro.	α_n	u_n	$(\alpha_n)^{-1}/u_n$	R^2
A*	5.426×10^{4}	1.657×10^{-5}	1.11	0.9113
B*	1.606×10^{5}	8.175×10^{-6}	0.76	0.9510
B	9.513×10^{4}	1.353×10^{-5}	0.78	0.9635
C	1.389×10^{7}	8.721×10^{-8}	0.83	0.9084
D	1.485×10^{9}	2.296×10^{-10}	2.93	0.7027
E	6.598×10^{4}	2.130×10^{-5}	0.71	0.9865

Table 4.7: Grain boundary impingement FIP Gumbel distribution linear fit statistics for Ti-18 BASCA

Micro.	α_n	u_n	$(\alpha_n)^{-1}/u_n$	R^2
B	3.745×10^{4}	7.126×10^{-5}	0.37	0.9841
C	2.079×10^{6}	6.154×10^{-7}	0.78	0.9512
D	1.695×10^{8}	2.666×10^{-9}	2.21	0.7555
E	2.099×10^{4}	1.206×10^{-4}	0.40	0.9608

Table 4.8: Lamellar FIP Gumbel distribution linear fit statistics for Ti-18 BASCA

Micro.	α_n	u_n	$(\alpha_n)^{-1}/u_n$	R^2
B	1.225×10^{5}	1.041×10^{-5}	0.78	0.9629
C	3.124×10^{7}	3.893×10^{-8}	0.82	0.9560
D	6.193×10^{9}	1.525×10^{-10}	1.06	0.9442
E	8.408×10^{4}	1.565×10^{-5}	0.76	0.9840

The simulated fatigue trends for the Ti-18 BASCA alloy closely resembled that of the Ti-64 β-annealed microstructure. Despite both materials being loaded to 75% of their simulated yield strain, the magnitudes of the computed extreme value FIPs for the Ti-18 BASCA material were considerably smaller than those of the Ti-64 β-annealed material. The simulated grain size trend demonstrates that smaller grain sizes are favored for longer fatigue lives, which is aligned with past experimental and simulation studies (Eylon and Hall, 1977; Eylon et al., 1976; Przybyla and McDowell, 2011). The observed texture dependence is even more pronounced for the lower FIP values, with multiple orders of magnitude separating the extreme value distributions (Figure 4.17). The rank

ordering for the preferred textures is the following: (1) transverse texture, (2) basal texture, and (3) EBSD scan texture. This trend is on account of the variation of the critical (0001) basal plane orientation with respect to the loading axis. Lastly, the phase volume fraction displays the same influence on the FIP distributions as determined for the Ti-64 microstructure, with the duplex microstructure (E) inducing larger FIP values than the lamellar structure (B). This trend implies that a reduction in the α-phase volume fraction is beneficial for fatigue properties. The extreme value marked radial correlation functions are once again utilized to determine the spatial correlations between the critical planes oriented for easy slip in relation to the extreme value FIP locations. Figures. 4.19–4.23 show the radial correlation function results for the Ti-18 BASCA microstructures.

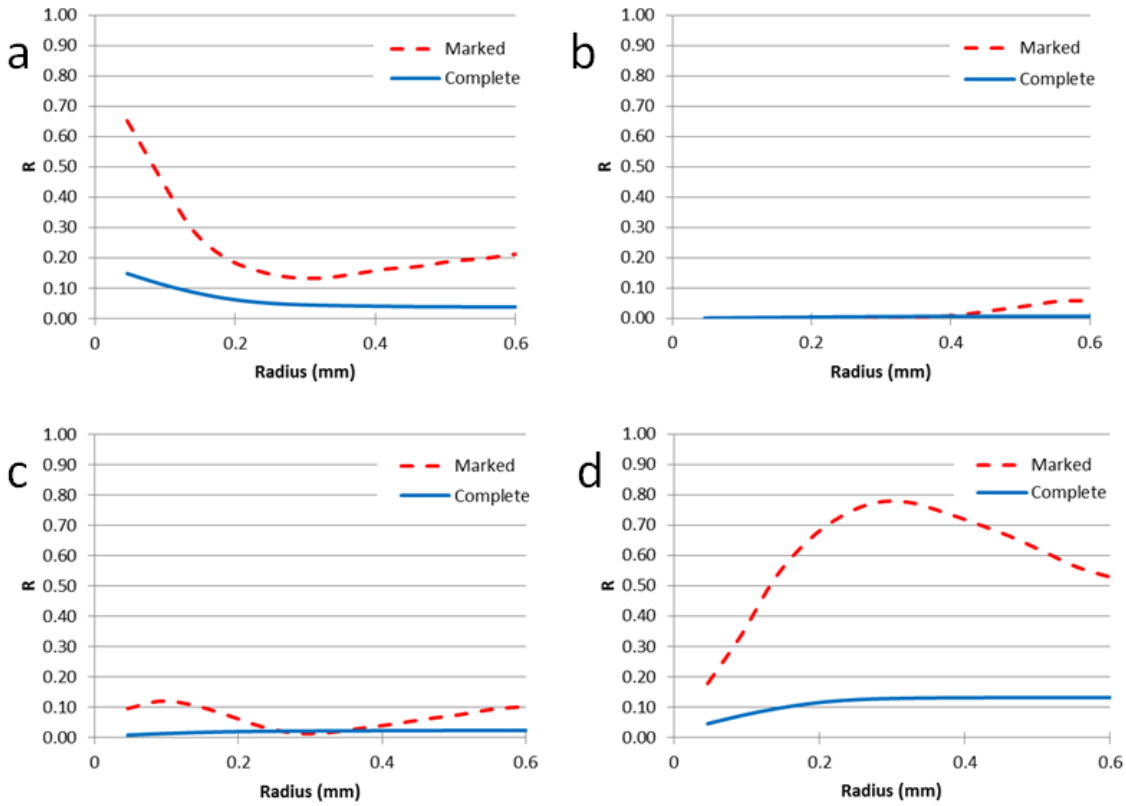

Figure 4.19. Ti-18 BASCA microstructure A radial correlation functions describing the correlation between the apparent Schmid factors for basal slip between 0.45 and 0.5 for the α + β colony grains and the apparent Schmid factors between 0.45 and 0.5 for (a) basal slip, (b) prismatic slip, (c) pyramidal $\langle a \rangle$ slip, and (d) $\langle 111 \rangle \{110\}$ BCC slip.

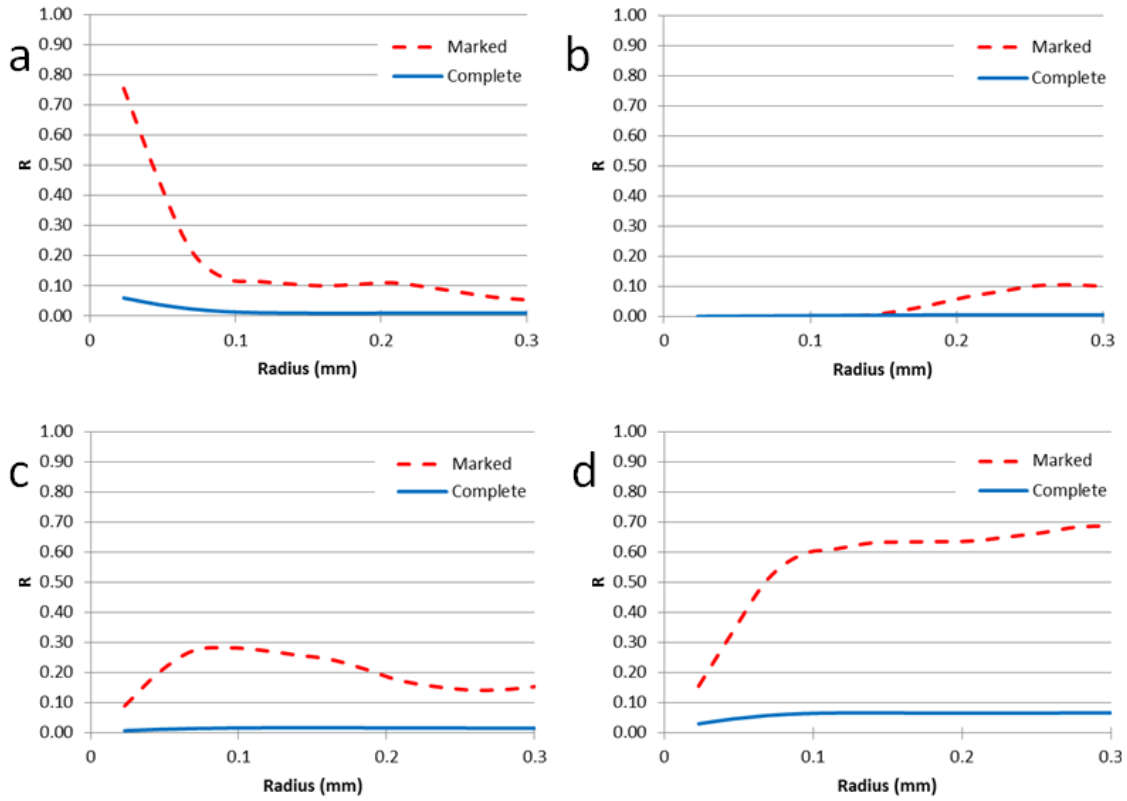

Figure 4.20. Ti-18 BASCA microstructure B radial correlation functions indicating the correlation between the apparent Schmid factors for basal slip between 0.45 and 0.5 for (a) basal, (b) prismatic, (c) pyramidal $\langle a \rangle$-type, and (d) $\langle 111 \rangle \{110\}$ BCC slip.

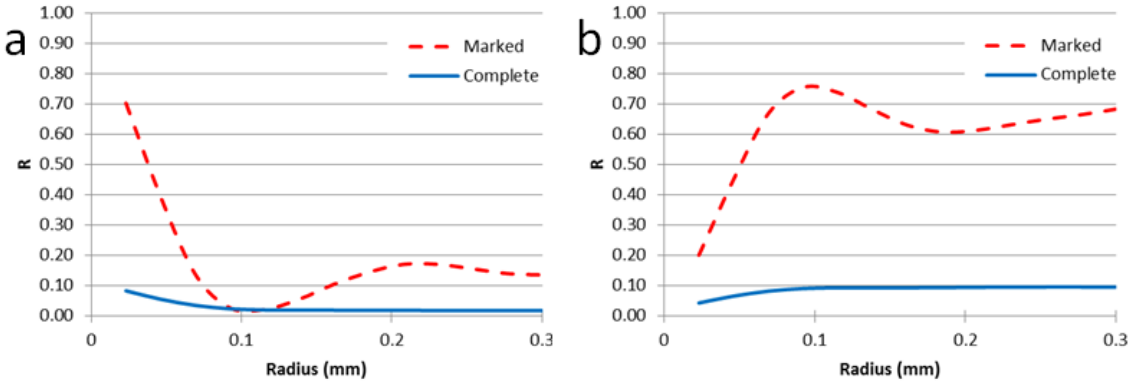

Figure 4.21. Ti-18 BASCA microstructure C radial correlation functions describing the correlation between the apparent Schmid factors for basal slip between 0.45 and 0.5 for the α + β colony grains and the apparent Schmid factors between 0.45 and 0.5 for (a) basal slip and (b) $\langle 111 \rangle \{110\}$ BCC slip.

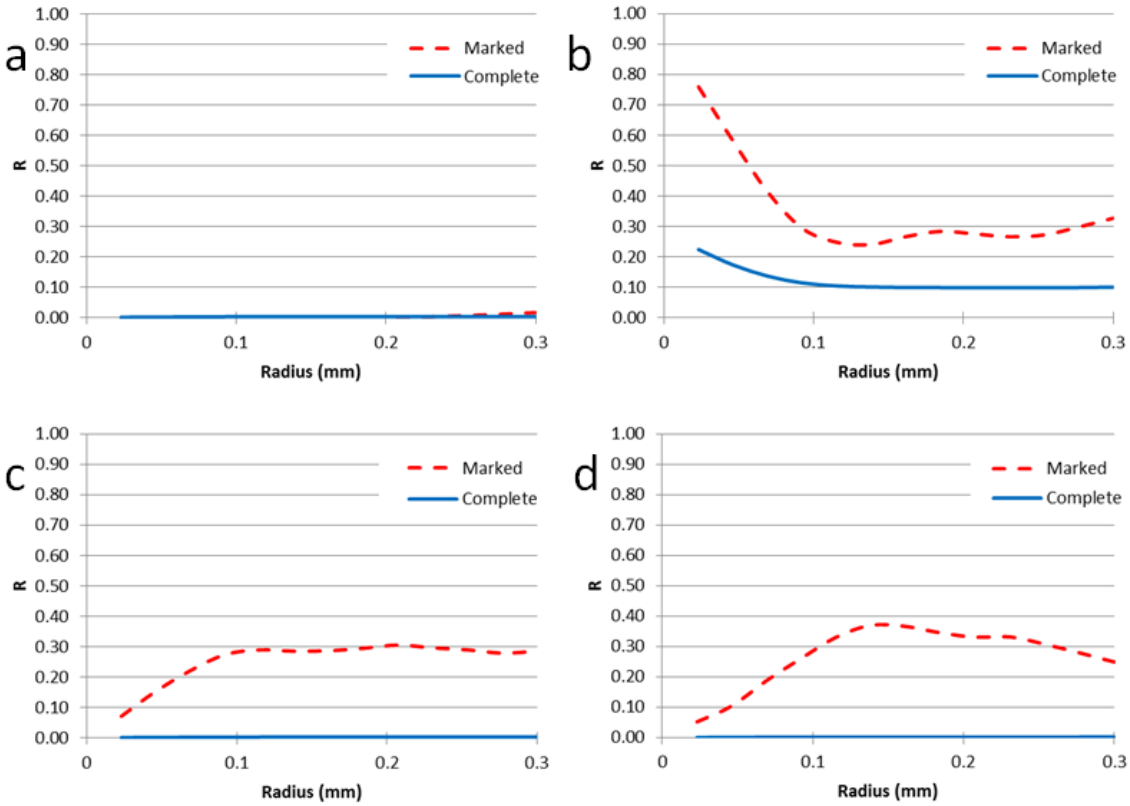

Figure 4.22. Ti-18 BASCA microstructure D radial correlation functions describing the correlation between the apparent Schmid factors for prismatic slip between 0.45 and 0.5 for the α + β colony grains and the apparent Schmid factors between 0.45 and 0.5 for (a) basal, (b) prismatic, (c) pyramidal $\langle a \rangle$-type, and (d) $\langle 111 \rangle \{110\}$ BCC slip.

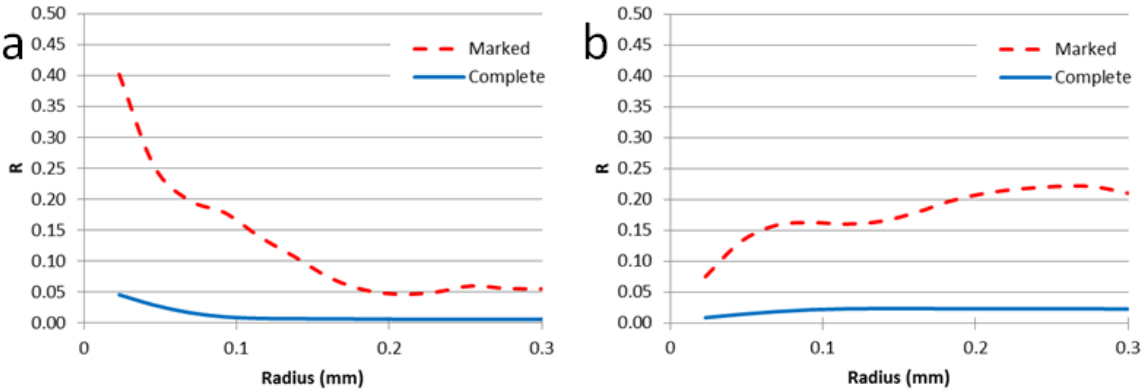

Figure 4.23. Ti-18 BASCA microstructure E radial correlation functions describing the correlation between the apparent Schmid factors for basal slip between 0.45 and 0.5 for the α + β colony grains and the apparent Schmid factors between 0.45 and 0.5 for (a) basal slip and (b) $\langle 111 \rangle \{110\}$ BCC slip.

The outcomes for the Ti-18 BASCA microstructures A, B, C, and E suggest that grains oriented for easy basal slip are likely to exist at the extreme locations in the

structure, while grains oriented for prismatic slip were prevalent for microstructure D. Previous experimental (Eylon, 1979; Shechtman and Eylon, 1978; Wojcik et al., 1988) and simulated (Przybyla et al., 2010; Przybyla and McDowell, 2011) studies agree that the basal slip planes are crucial for fatigue, and the prismatic orientations for microstructure D are justified by its imposed transverse texture, favoring prismatic slip. In all cases, these softer oriented grains were determined to be nearby harder oriented grains possessing high apparent Schmid factors for BCC slip. These findings further reinforce the argument for the critical role of this hard-soft grain boundary interface in fatigue crack nucleation (Dunne, Rugg, et al., 2007; Hasija et al., 2003; Venkataramani et al., 2006).

Conclusions

Simulated microstructure-sensitive fatigue performance of two distinct titanium alloy microstructures has been investigated. The considered materials were β-annealed Ti-6Al-4V and Ti-18 BASCA, both exhibiting a Widmanstätten morphology. The material constitutive relations are described via crystal plasticity models implemented into ABAQUS UserMATerial subroutines, which have been calibrated to experimental data in the previous Chapter. These models were utilized to simulate fatigue loading of variant microstructures of each alloy to investigate the performance trends associated with the mean grain size, phase volume fraction, and texture. The results suggest that reduced grain sizes, transverse textures, and reduced α-phase lead to improved fatigue performance. Extreme value marked correlation functions were employed to study the favorably oriented slip systems occurring near the extreme value FIP locations. The correlation statistics show that soft oriented grains, preferring basal or prismatic slip, are typically located at the maximum FIP location and are situated near hard oriented grains. The interaction between the hard and soft grains induces a substantial increase in localized stress and strain, leading to increased possibility of fatigue crack initiation.

CHAPTER 5

SIMULATED FATIGUE OF TI-18 STA MICROSTRUCTURE

Introduction

Titanium alloys are recruited for advanced engineering applications where their exceptional properties can be exploited, e.g., their high strength-to-weight ratio and corrosion resistance. Among the different types of alloys, metastable beta titanium alloys provide superior formability and permit forging of complex components (Huang et al., 2011; Ivasishin et al., 2008). Beta titanium is also known to be less sensitive to processing parameters; hence it can produce a more homogeneous strength through the thickness of very large forgings. On account of these properties, beta titanium is experiencing increased use in aerospace structures (Boyer and Briggs, 2005). Though the formability of near beta titanium is highly advantageous, forging of titanium alloys can induce strong micro-textured regions of similarly oriented grains that lead to a reduction in fatigue strength, particularly in dwell loading scenarios (Le Biavant et al., 2002; Sinha et al., 2006; Woodfield et al., 1995). These micro-textured regions have become very problematic in critical forged parts in industry, e.g. turbine disks (Gey et al., 2012). The reduction or elimination of these textured zones is critical for ensuring longer fatigue lives of engineering components and reducing the scatter of fatigue life data.

The discovery of these micro-textured zones was driven by an interest in the experimentally observed life debit associated with dwell fatigue loading of α/β titanium alloys. Early titanium dwell fatigue research was focused on the lamellar, a.k.a. Widmanstätten, microstructures which were known to be more resistant to dwell and creep scenarios. In all cases, dwell loading was found to significantly inhibit the fatigue life of the material (Evans and Gostelow, 1979; Evans, 1987; Eylon and Hall, 1977). The primary cause of this sensitivity was proposed to be from hydrogen accumulation on slip

bands during the dwell application (Eylon and Hall, 1977). In these studies, the observed fracture surfaces displayed facets formed by the cleavage of lamellar colonies consisting of aligned secondary alpha platelets. These results showed that the aligned alpha laths promoted a cleavage plane across the entire colony in spite of the presence of the interstitial beta phase laths. The cleavage plane was typically identified with the basal slip plane of the secondary alpha phase. Local texture regions were first determined to be important when Eylon (1979) found that it was possible for facets to form across neighboring colonies sharing the same basal plane orientation.

Woodfield et al. (1995) investigated the dwell sensitivity of bimodal α/β Ti-6242 microstructures and they also recorded a large reduction in fatigue life for dwell loading. While exploring the thermo-mechanical processing effects on the dwell fatigue life, they detected that it was possible to form large primary alpha colonies of similarly oriented grains which would promote a cleavage-like failure surface across the entire primary alpha colony. Le Biavant et al. (2002) termed these micro-textured regions as "macrozones" during their study on a duplex Ti-64 alloy. They observed that their macrozones were on the order of one hundred grains and that they dictated the fatigue crack initiation process via several of the primary alpha grains cracking on basal planes within the textured zones.

The formation of these macrozones was initially suggested to be an effect of the prior β phase grain structure (Woodfield et al., 1995). This concept is supported by the prior beta phase grain reconstruction derivations of Glavicic et al. (2009), however, the beta phase reconstruction works of Bocher et al. (2005) and Germain et al. (2005) disagree. While these results are in apparent contradiction, Germain et al. (2008) proposed that the prior beta phase structure is only one of several factors contributing to the microtexture generation; consequently, the disagreement in the beta phase grain reconstruction findings can likely be attributed to a difference in the combined effects producing the investigated macrozone formations. Germain et al. (2005, 2008) concluded

that the macrozones in duplex titanium alloys formed by the overlapping of two distinct primary and secondary alpha phase microtextures produced at different stages of thermo-mechanical processing. The primary alpha textured zones can be caused by (i) the size and orientation of the initial lamellar colonies that are broken up during deformation, (ii) the tendency of HCP crystal rotation during deformation to trend toward specific texture orientations, and (iii) the orientation of the new primary alpha grains formed during deformation and annealing (Germain et al., 2008). The microtexture of the colony grains can be created by the (i) conservation of the Burgers orientation relationship during and after deformation between neighboring primary alpha and beta grains as well as (ii) when the secondary alpha lath growth selects one of the 12 possible Burgers orientation variants that are closely aligned with neighboring primary alpha phase grains. Hence, the creation of the macrozones in duplex microstructures is a very complex process, however, the macrozones will generally form parallel to the direction of material flow during forging (Gey et al., 2012), e.g., in the elongation direction during billet creation (Uta et al., 2009).

Advances in cooperative mechanical testing and EBSD methods have allowed numerous researchers to highlight the importance of macrozones in contributing to fatigue crack initiation and propagation. For example, Sinha et al. (2006) observed that the site of an initiated crack facet for a dwell-fatigued Ti-6242 specimen directly correlated to a macrozone location on the fracture surface. Bridier et al. (2008) determined that considerable microcracking occurred on basal planes within micro-textured bands in a Ti-64 microstructure. Uta et al. (2009) detected that multiple cleavage cracks formed and quickly propagated in a macrozone of bimodal IMI 834 possessing several primary alpha grains possessing basal planes oriented nearly perpendicular to the applied load. Gey et al. (2012) showed that microtexture can be eliminated by severe compressive deformation oriented in the opposite sense of the original billet elongation direction. These studies have validated the importance of the macrozones and have

provided valuable insight into some of the mechanisms leading to failure, yet much additional work is necessary to fully understand the performance implications of the micro-textured regions and how to account for them in the design of engineering components.

In the current study, a newly developed near-β titanium alloy, Ti-18, has been acquired in a solution-treated, age-hardened (STA) condition (Fanning, 2011) from the Titanium Metals Corporation (Exton, PA). Characterization of this material has been accomplished by EBSD Analytical Inc. (Lehi, UT) and the received micrographs display a duplex structure consisting of globular alpha phase (HCP) precipitates dispersed throughout a beta phase (BCC) matrix. EBSD scans reveal strong micro-textured regions of beta phase grains. For the purpose of simulating fatigue performance with (ABAQUS, 2011) finite element software, these texture bands are approximated as dendritic grains. A crystal plasticity model possessing a Kocks-type flow rule (Kocks et al., 1975) is utilized to simulate the fatigue trends associated with varying orientations of texture bands with respect to the applied macroscopic loading and the results are discussed here-in. The methodology behind fatigue indicator parameters, extreme value statistics, and the statistical volume element generation are briefly outlined and the key findings are summarized in the conclusion.

Methodology

Fatigue Indicator Parameters

A critical plane approach has been utilized to quantify the simulated microstructure fatigue sensitivity of the Ti-18 STA material. Numerous critical plane approaches using macroscopic damage parameters have been identified to correlate very well with experimental fatigue data (Gallagher et al., 2004; McDowell and Berard, 1992; Park and Nelson, 2000). When critical plane parameters are computed at the micro-scale,

they are termed “fatigue indicator parameters” (FIPs). These FIPs are determined at the scale of microstructural features to provide a measure of the accumulated damage associated with fatigue crack initiation and propagation. In this study, we will utilize two FIPs (P) to describe the fatigue behavior of the Ti-18 STA structure. The first is the Fatemi-Socie FIP (Fatemi and Kurath, 1988; Fatemi and Socie, 1988):

$$P_{FS} = \frac{\Delta\gamma^{p}_{\max}}{2}\left(1 + K\frac{\sigma^{n}_{\max}}{\sigma_{y}}\right) \tag{5.1}$$

Here, $\Delta\gamma^{p}_{\max}/2$ is the maximum plastic shear strain range calculated over a cycle, K is a constant denoting the normal stress dependence, $\sigma^{n}_{\max}$ is the stress normal to the $\Delta\gamma^{p}_{\max}$ plane at peak loading, and σ_{y} is the yield strength of the material. The maximum plastic shear strain range (MPSS) accounts for the ratchet strain accumulated from previous cycles, as can be referenced in Equations 3.1 and 3.2. In addition to the Fatemi-Socie (FS) FIP, a modified FS FIP based on the total plastic shear strain has also been determined. This strain accumulation (SA) FIP can be expressed as the following:

$$P_{SA} = \gamma^{p}_{net}\left(1 + K\frac{\sigma^{n}_{\max}}{\sigma_{y}}\right) \tag{5.2}$$

where γ^{p}_{net} represents the maximum accumulated plastic shear strain and $\sigma^{n}_{\max}$ is the stress normal to the γ^{p}_{net} plane. Both of the FIP values are determined on a non-local area averaging basis with areas ranging from the size of a single element to grids of 7 x 7 elements. A schematic of the Fatemi-Socie FIP can be referenced in Figure 4.1(a). The parameter constant, *K*, is defined to be 1 for all of the FIP calculations.

Extreme Value Statistics

Once the maximum area-averaged FIPs have been sampled from several fatigue simulations, the FIP data are analyzed with extreme value statistics. The generated data have been fit to Gumbel (1958) (Type I) extreme value probability distributions, i.e.,

$$F_{Y_n}\left(y_n\right) = \exp\left[-e^{-\alpha_n\left(y_n - u_n\right)}\right] \tag{5.3}$$

where $F_{Y_n}\left(y_n\right)$ is the probability that the value of Y_n will be less than or equal to y_n, α_n is an inverse measure of dispersion, and u_n is the characteristic largest value of the sampled population. The α_n and u_n parameters can be directly determined through a linear regression fit to the linearized probability distribution for each of the maximum FIP sets from multiple simulations associated with particular microstructure statistics (cf. Eq. 4.9 – 4.12). Trends in the microstructure-sensitive fatigue performance can then be evaluated through the observed characteristics of the extreme value distributions.

Microstructure Representation

Microstructural characterization of the Ti-18 STA transverse face displayed a substantial amount of micro-textured regions of beta-phase (BCC) grains which are the dominate phase grains possessing 72% of the volume fraction. Investigation of the longitudinal phase showed that these sharp macrozones were significantly elongated into a band-like structure with many of the textured bands spanning the entire 200 μm scan length. A micrograph and matching texture colormap of the longitudinal is shown in Figure 5.1. These sharp textured bands pose a serious obstacle to simulating a 3D geometry due to the combination of extremely small grains (1 μm α-phase precipitates, 3.5μm β-phase grains) and very large macrozones containing hundreds of grains. An enormous number of elements would be required to generate a structure large enough to capture the long range effects of the microtexture while maintaining a mesh density fine

enough to model the individual alpha precipitates. Unfortunately, it is computationally infeasible to simulate 3D geometries possessing such a large number of elements with our crystal plasticity algorithms. Due to this restriction, 2D generalized plane strain elements (CPEG4R) are employed to model the longitudinal cross section of the Ti-18 STA material. Each of the instantiated ABAQUS models are a 140 μm square geometry and the texture bands are realized by utilizing a dendritic microstructure generator created by Padbidri (2013). The produced macrozones extend the length of the model and have an average width of 15 μm; their crystallographic orientation is sampled from a beta phase pole figure through utilization of MTEX (Bachmann et al., 2010), a free and open source MATLAB (2011) plug-in. Alpha precipitates have been super-imposed onto the layered structure by directly defining the precipitate phase and orientation for elements having centroids nearest to alpha phase EBSD scan points. The precipitate mapping is altered for each model by randomly placing a 140 μm box into the scanned area shown in Figure 5.1. An example statistical volume element (SVE) is presented in Figure 5.2.

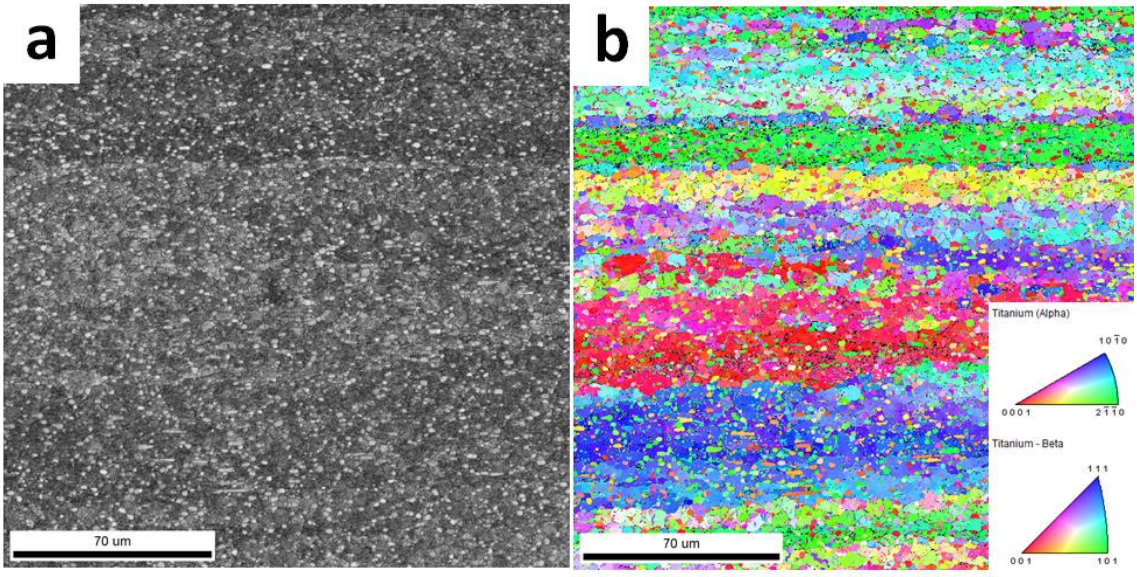

Figure 5.1. (a) Optical micrograph of the Ti-18 STA longitudinal face, and (b) matching texture color map acquired from an EBSD scan with a 0.2μm step size from EBSD Analytical Inc.

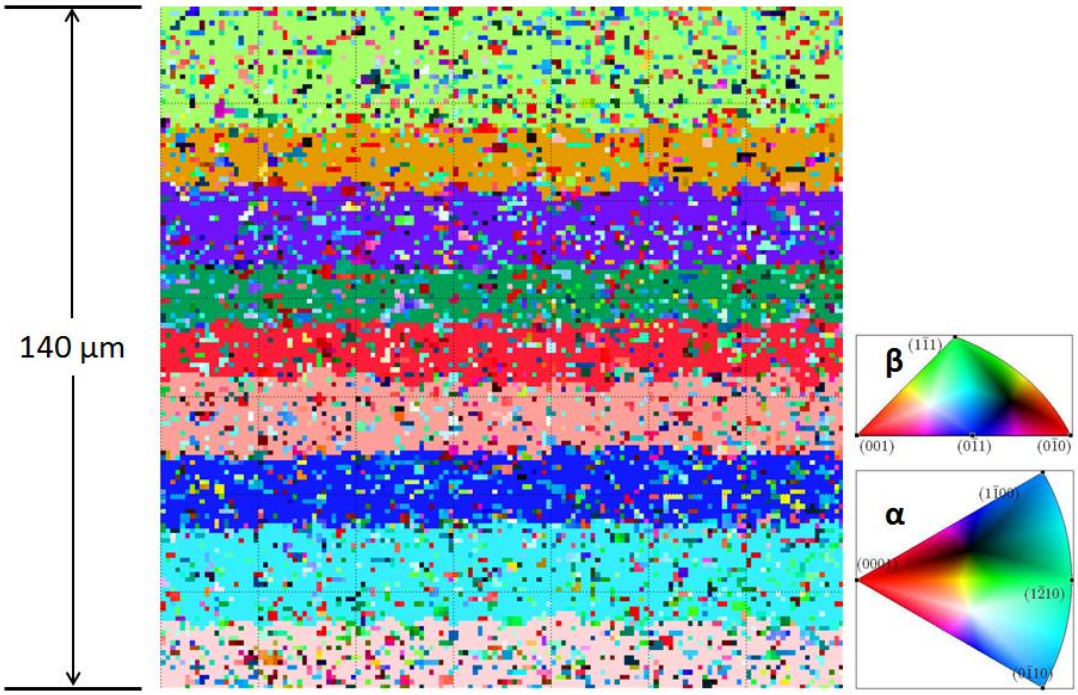

Figure 5.2. Example statistical volume generated with dendritic grains representing textured bands. EBSD Scan created with MTEX (Bachmann et al., 2010)

Simulated Orientation Dependence

The activation enthalpy crystal plasticity model was exercised to describe the deformation activity of the Ti-18 STA microstructure. The model framework details and calibration is included in Chapter 3. The dendritic structure generator was utilized to simulate the dependence of the calculated fatigue indicator parameters on the orientation of the applied macroscopic loading. Three different orientations of the texture bands were investigated with angles of 0^o, 45^o, and 90^o to the loading axis. Fifty realizations of both the parallel and 45^o structures were created to produce simulation data. Rather than creating completely new structures for the perpendicular simulations, these simulations were achieved by simply changing the load orientation of the parallel models. An example of a generated 45^o model is displayed in Figure 5.3. The instantiated models were loaded in fully reversed cycling with a strain amplitude of $\varepsilon_a = 0.8\%$ and strain rate of $\dot{\varepsilon} = 2\times10^{-3}\, s^{-1}$. This strain amplitude corresponds to 80% of the simulated yield strain,

i.e., $\varepsilon_y = 1.0\%$. These texture band structures were simulated to three cycles of loading before computing the FIP values. Periodic boundary conditions have been enforced on all faces of the simulation geometry. The maximum calculated FIP has been determined for fifty simulations of the three different oriented macrozones and they are plotted on a linearized Gumbel chart for each texture band orientation in Figure 5.4.

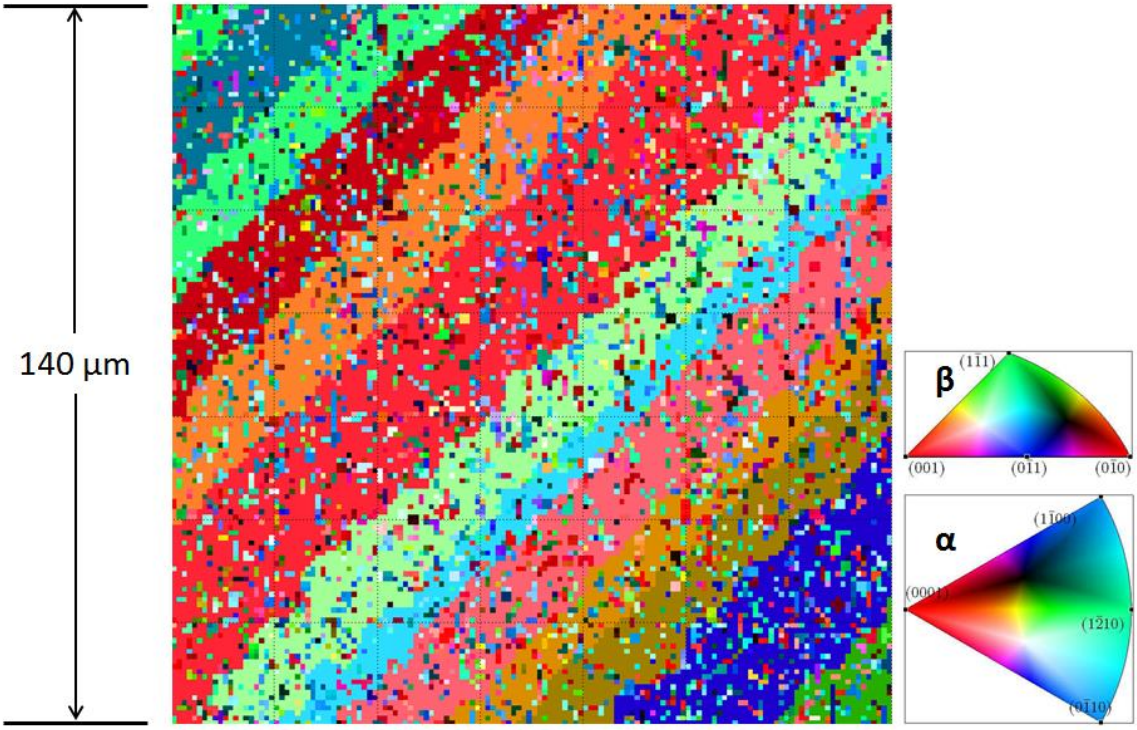

Figure 5.3. Example statistical volume generated with dendritic grains representing textured bands at a 45^o angle. EBSD Scan created with MTEX (Bachmann et al., 2010)

As can be seen in Figure 5.4, all of the FIP distributions exhibited a very distinct bi-linear behavior. This is thought to be an effect of the very small FIP values determined, since larger FIP values converge to a single Gumbel distribution with fewer sets of data. It is possible that the small FIPs are induced by the generalized plane strain assumption that all out of plane shear components are equated to zero. A direct comparison of the FIP distributions between the three orientations is depicted in Figure 5.5.

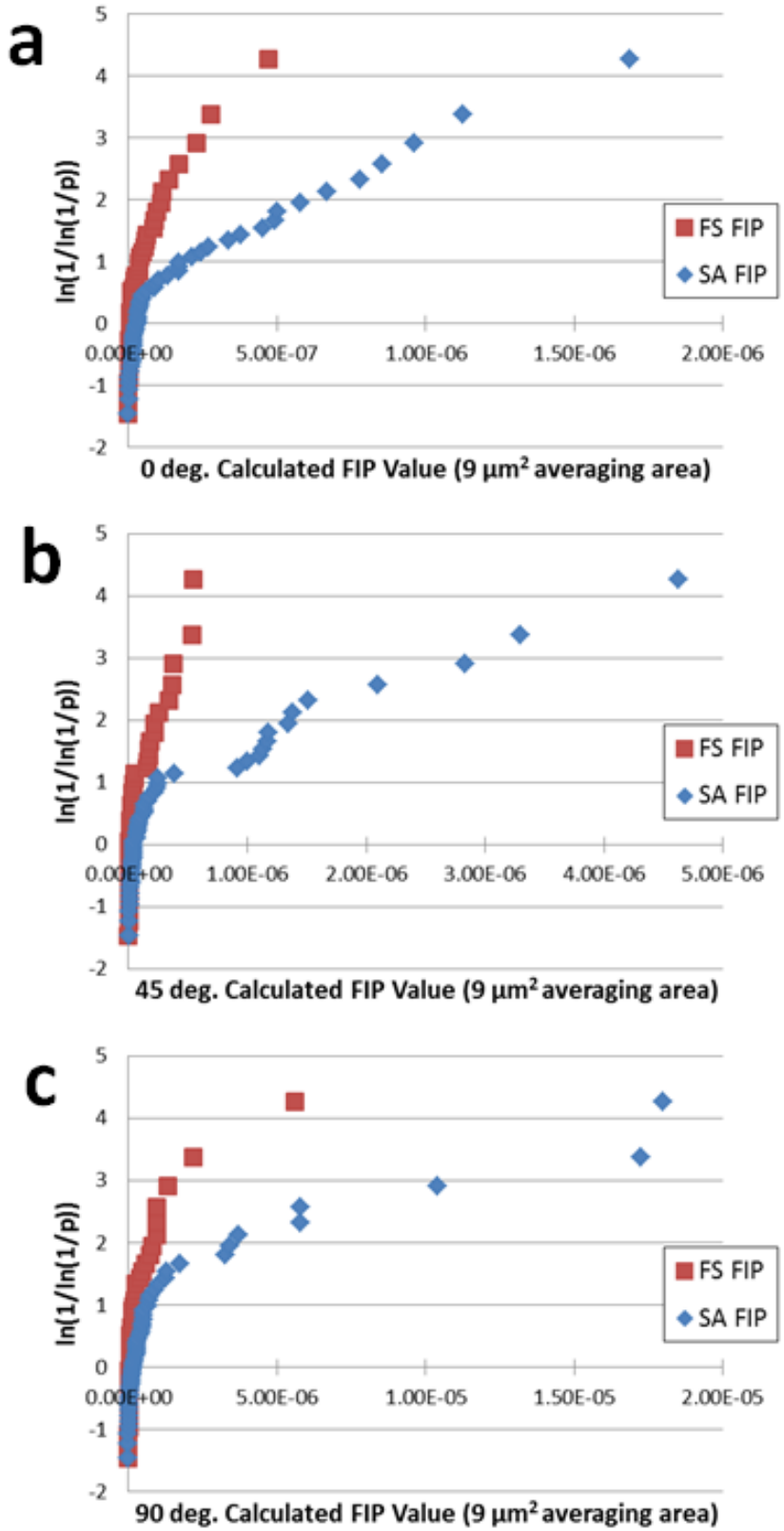

Figure 5.4. FIP distributions for the Fatemi-Socie (FS) FIP and the strain accumulation (SA) FIP for loading misalignment angles of (a) 0^o, (b) 45^o, and (c) 90^o.

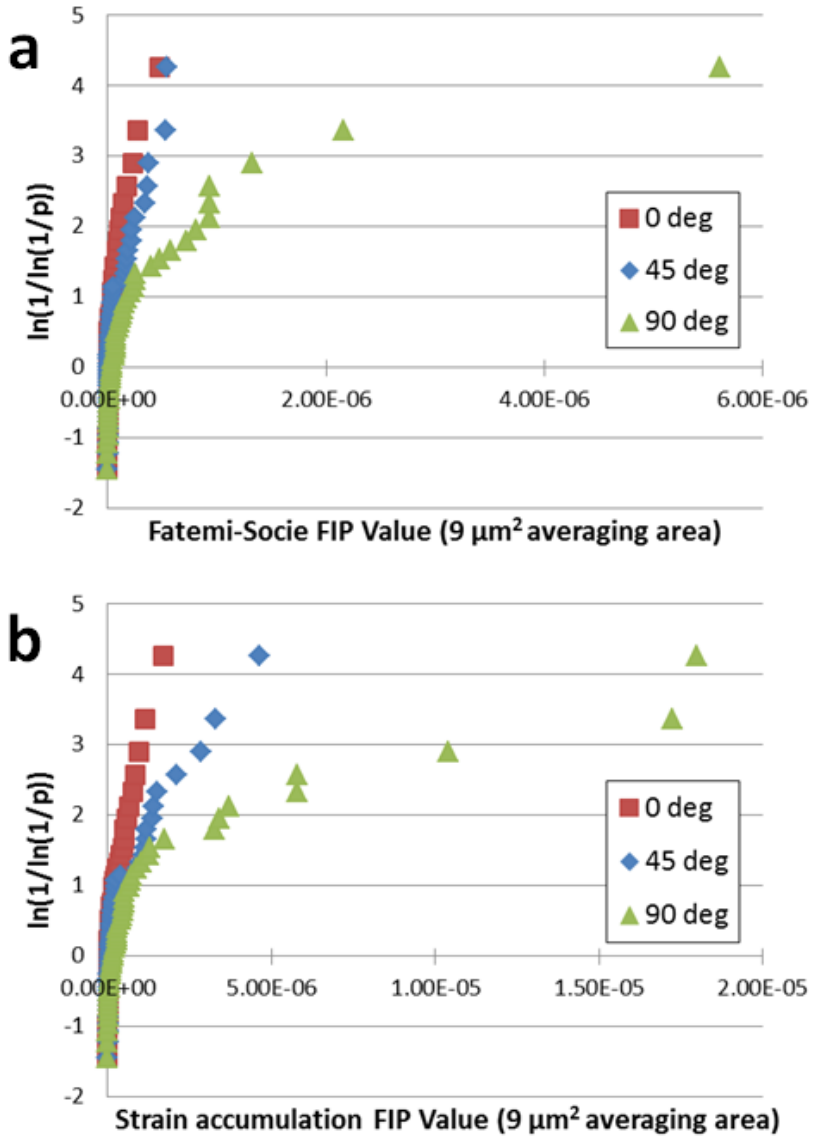

Figure 5.5. Comparison of the computed (a) Fatemi-Socie FIP distrubtions and (b) Strain accumulation FIP distributions for the three simulated orientations.

The FIP distributions suggest that larger driving forces for fatigue crack initiation and propagation are present with increasing misalignment between the loading and macrozone elongation direction. This result is a reasonable as it suggests that there is a greater possibility of material failure when the strongly textured regions are perpendicular to the applied loading. This finding is in agreement with numerous experimental results that state that the micro-textured zones debit the fatigue lives by providing faceted fracture locations at large regions of grains favorably oriented for

cleavage fracture (Sinha et al., 2006; Uta et al., 2009). Ideally, the presence of macrozones can be diminished or even eliminated through severe compression (Gey et al., 2012). However, in cases where the textured bands are present, our simulated results advocate that the forging process should be designed to induce macrozone bands aligned with the maximum loading direction to increase fatigue life.

Conclusions

A simulated fatigue study of a micro-textured Ti-18 STA alloy has been completed. The material deformation was informed by the activation enthalpy crystal plasticity model, which was implemented as an (ABAQUS, 2011) subroutine. A dendritic microstructure generator was utilized to instantiate several 2D generalized plane strain geometries having banded micro-textures with varying angles between the macrozones and the maximum principal stress direction. The simulation results suggest that higher misalignment angles between the textured bands and macroscopic applied loading are detrimental to fatigue performance. Therefore, it is proposed that forging processes should be tailored to produce textured bands parallel to the desired loading direction of the finished component if macrozones cannot be eliminated.

CHAPTER 6

SUMMARY AND CONCLUDING REMARKS

Summary

Cyclic deformation experiments with differing strain amplitudes, strain rates, and temperatures have been accomplished to inform the calibration of two crystal plasticity models to three distinct titanium alloy microstructures: β-annealed Ti-6Al-4V, Ti-18 in a solution-treated, age-hardened STA condition (Fanning, 2011), and Ti-18 with a beta-annealed, slow-cooled, age-hardened (BASCA) treatment. The experimental results suggest that superior mechanical properties are obtained through the STA processing of the Ti-18 material, which exhibited an increased uniaxial yield strength, ultimate strength, and tensile ductility when compared to the BASCA treated material. For the purpose of model calibration, polycrystalline finite element (ABAQUS) model realizations (i.e., Statistical Volume Elements) were instantiated using an ellipsoidal packing algorithm to fit microstructure statistics acquired from EBSD characterization. The constitutive framework for each of the models has been outlined. A number of the model parameters have been obtained from literature sources, while the remainder has been estimated to achieve agreement between the simulated and experimental stress-strain responses for all three microstructures. The calibrated models were then validated with additional experimental data.

The calibrated and validated models were utilized to simulate the fatigue performance trends of the Ti-64 β-annealed and Ti-18 BASCA alloys with variant microstructure statistics. The maximum computed fatigue indicator parameter (FIP) values obtained from several simulations have been fit to Gumbel (1958) extreme value distributions. The results suggest that finer grain sizes, a reduced volume fraction of

primary α-phase, and a transverse texture where the c-axis is oriented perpendicular to the applied loading direction promote improved fatigue resistance.

Marked radial correlation functions have been utilized to study spatial correlation between favorably oriented slip planes in adjacent grains/phases at the extreme value locations in the Ti-64 and Ti-18 BASCA microstructures. The results show that basal planes with large Schmid factors are typically present at the critical locations in the microstructures (Przybyla and McDowell, 2011). The only deviations from this result are induced by the applied texture. The radial correlation findings for the transverse textured polycrystals show that prismatic slip planes are favorably oriented for slip at the extreme value location; and the models fit to the EBSD scanned texture of the Ti-64 material displayed large Schmid factors for BCC slip planes at the critical FIP sites. In several cases, the radial correlation functions reveal that favorably oriented soft-slip basal planes are frequently situated nearby grains exhibiting large BCC Schmid factors, i.e., possessing a hard-slip orientation. The importance of this observed hard-soft grain combinations agrees with previous findings on duplex titanium microstructures (Przybyla and McDowell, 2011).

Finally, a simulated fatigue study of the Ti-18 STA material has been accomplished. The sharp beta phase texture bands of the longitudinal face have been approximated as dendritic grains in a 2D generalized plane strain ABAQUS model. The fatigue property trends for varying orientations of the banded microtexture have been investigated. The simulated results suggest that higher misalignment angles between the texture bands and macroscopic applied loading axis are detrimental to the material's fatigue performance.

Recommendations for Future Work

In the present work, solely macroscopic experimental data have been utilized to facilitate the calibration of the crystal plasticity models. At this scale, the experimental results lose sensitivity to the microstructural scale stress state heterogeneities, thereby

making it difficult to ascertain the precise combination of parametric values that cooperatively generate the macroscopic response. Many of the model parameters have been directly acquired from literature sources and several of the estimated values for the polycrystals can be compared to experimental works on single crystal alpha titanium. However, since experimental data for single lamellar colonies are not available, the Widmanstätten model parameters have been assumed to largely follow those of the primary alpha phase grains. To validate or refine the calibrated lamellar colony constants, it is possible to employ a combination of EBSD and nano-indentation techniques to measure the slip system strengths within the colony packets and ensure accuracy in the related parameters.

An attractive characteristic of critical plane approaches to fatigue is that they are often found to be more accurate for cases of combined loading. Therefore, a natural extension of the crystal plasticity models would be for application to multi-axial fatigue loading. Combined loading deformation experiments can be accomplished and the model parameters should then be altered to agree with both uniaxial and multi-axial stress-strain data. Following the experimentation and calibration, multi-axial fatigue simulations can be performed on numerous instantiated statistical volume elements and the results can be compared to the uniaxial findings of the present study.

Another potential experimental study building upon the current work would be to conduct several low-cycle fatigue experiments to failure. The fractured specimen surface could then be investigated to identify the critical crack initiation mechanisms. These observed damage mechanisms could then be compared to the simulated extreme value sites to validate the crystal plasticity model's ability to identify the critical microstructure attributes that lead to crack initiation. The fracture characteristics of interest would be the slip plane where the crack nucleated and the orientation of neighboring grains to identify a possible hard-soft grain combination, as suggested by the radial correlation function results. The proposed study could also validate the effectiveness of the computed FIPs in

correlating with fatigue cycle life via a Coffin-Manson type relationship as well as potentially identify new FIPs that could more accurately describe the damage accumulation physics leading to failure.

Due to the computational costs associated with the crystal plasticity formulations, it is not feasible to utilize the models for application to microtextured materials. The microtextured regions are typically on the order of hundreds of grains. This indicates that a prohibitively large number of elements would be required to capture both the long range effects associated with the macrozones and have a fine enough mesh to represent the individual grains. However, the newly developed methodology of the material knowledge systems (MKS) (Kalidindi et al., 2010) displays promising potential for simulating extremely large, complex microstructures. The MKS framework has been shown to be acceptably accurate for simulating small elastic loading of multi-phase materials while dramatically decreasing computational time (Fast and Kalidindi, 2011). This approach can potentially be extended and verified for application to fatigue loading, which includes small levels of localized plasticity within the matrix. This study would pave the way for simulating fatigue dependence of extreme large microstructures if the calculated FIP values determined with the MKS approach are closely aligned with those of the crystal plasticity models, or even if the microstructure-property trends are preserved. The MKS approach could then be utilized to simulate a 3D microtextured model, e.g., the Ti-18 STA microstructure, to help facilitate materials design.

APPENDIX A

TI-64 EBSD CHARACTERIZATION

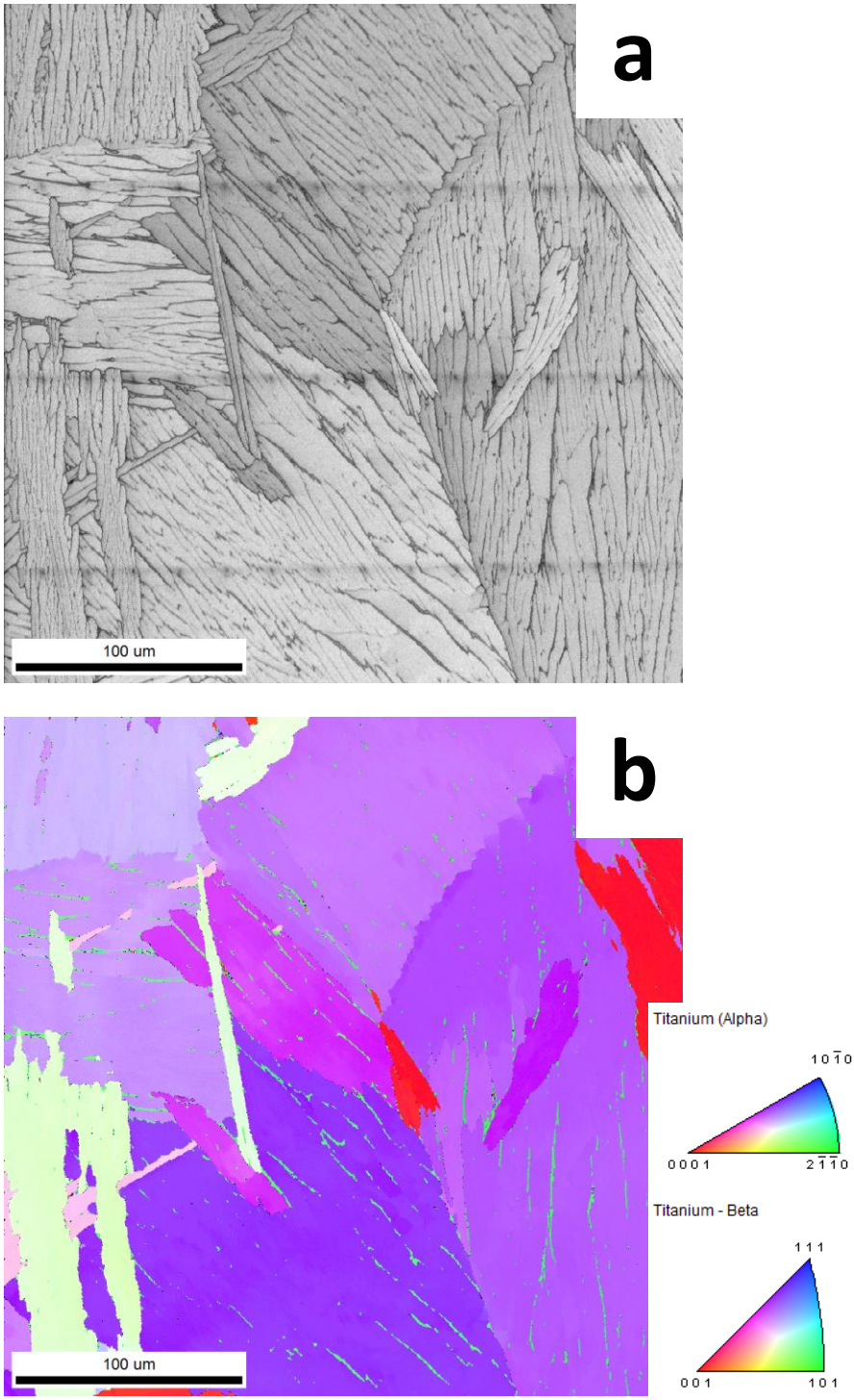

Figure A.1. Ti-64 β-annealed microstructure transverse high resolution (a) micrograph and (b) texture colormap with a 0.3 μm scan step size.

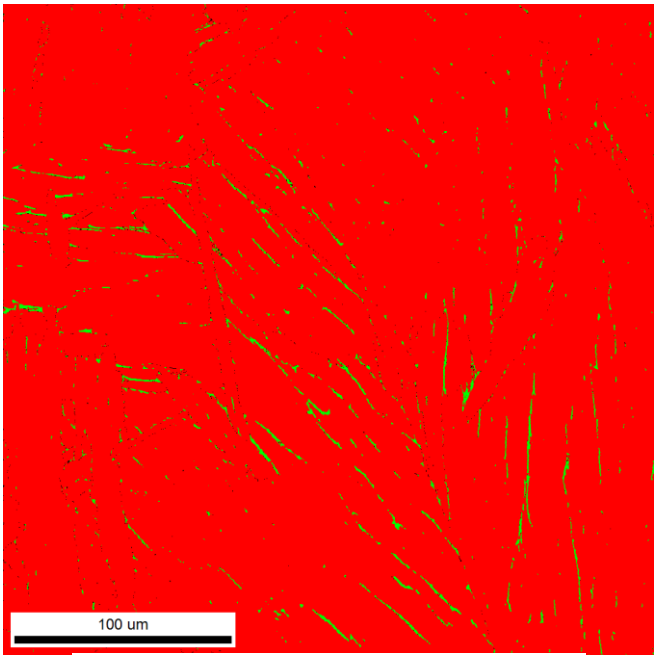

Figure A.2. Phase mapping of the high resolution Ti-64 transverse EBSD scan having a 0.3 μm step size.

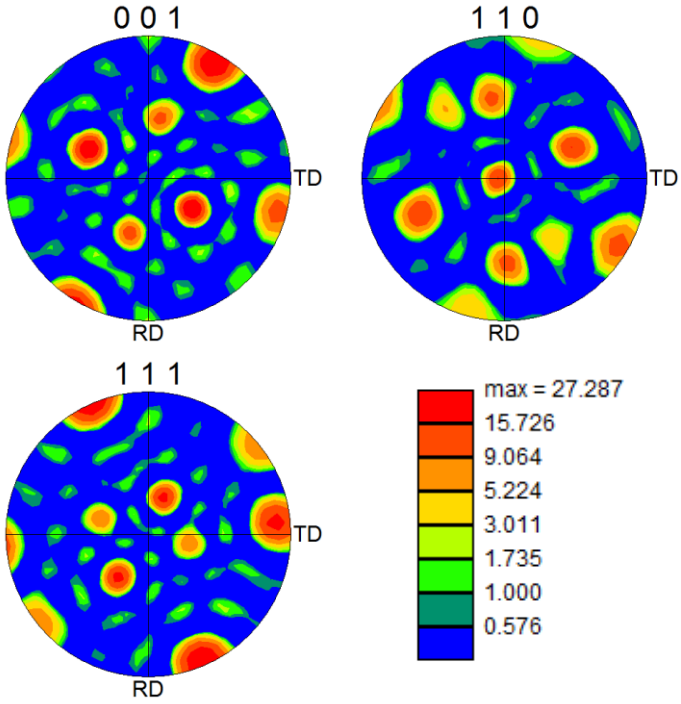

Figure A.3. Pole figures for the beta phase in the Ti-64 β-annealed microstructure transverse face.

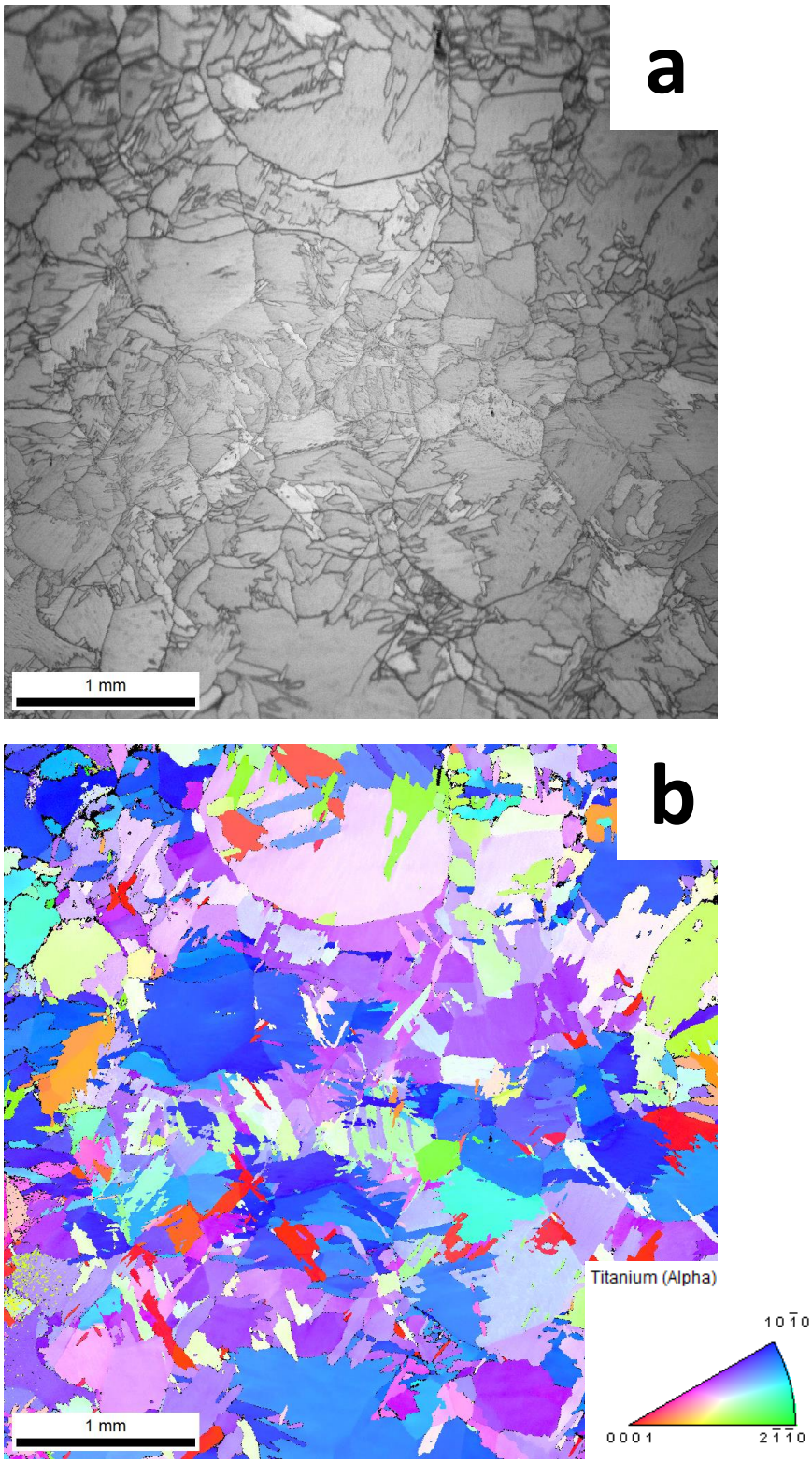

Figure A.4. Ti-64 β-annealed microstructure longitudinal face (a) micrograph and (b) texture colormap with a 4 μm scan step size.

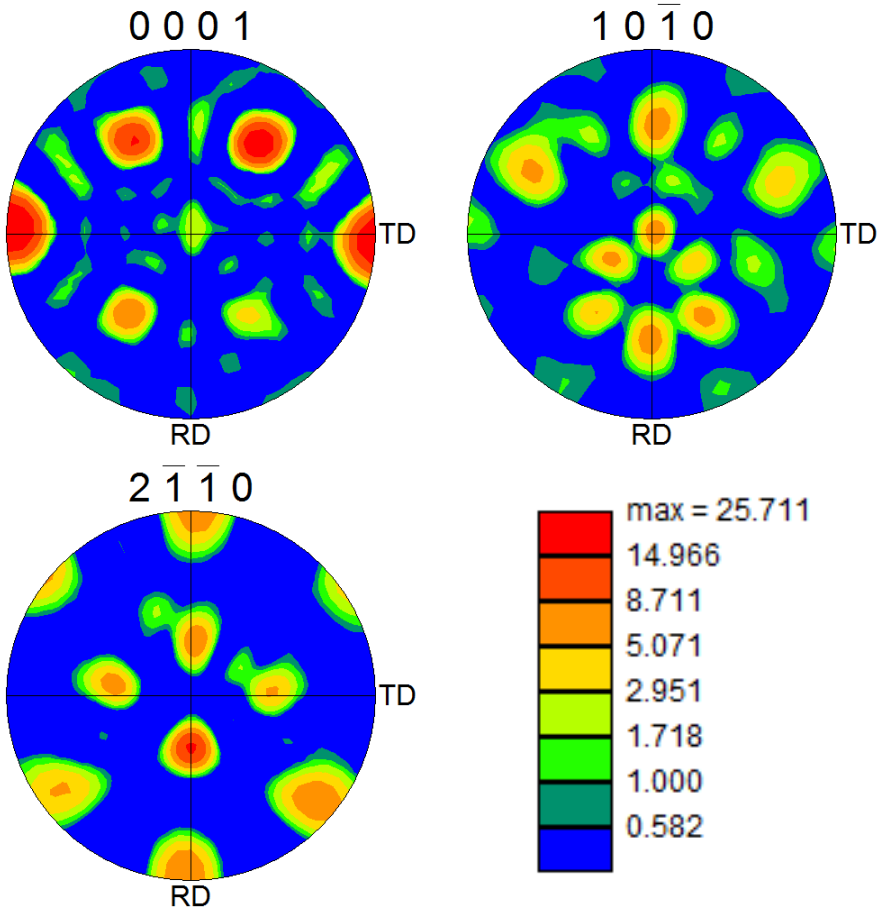

Figure A.5. Alpha phase pole figures for Ti-64 β-annealed microstructure longitudinal cross section face.

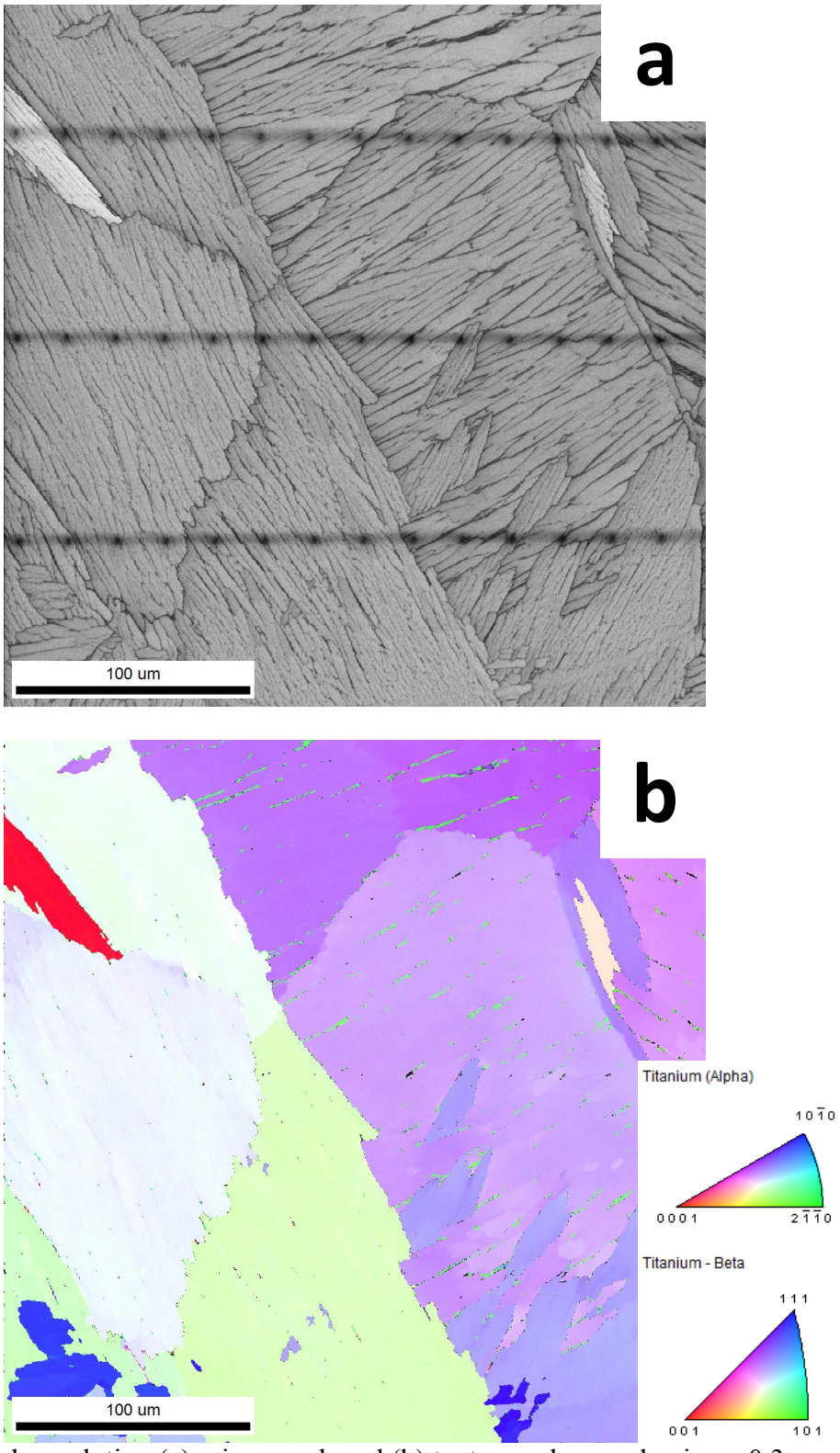

Figure A.6. High resolution (a) micrograph and (b) texture colormap having a 0.3 μm step size for the Ti-64 β-annealed microstructure longitudinal face.

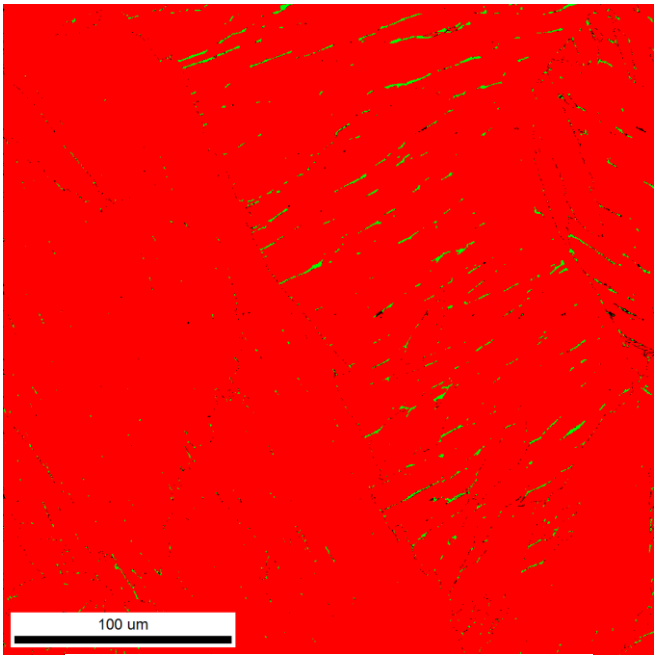

Phase	Total Fraction	Partition Fraction
Titanium (Alpha)	0.987	0.990
Titanium - Beta	0.010	0.010

Figure A.7. Phase map of high resolution Ti-64 longitudinal EBSD scan having a 0.3 μm step size.

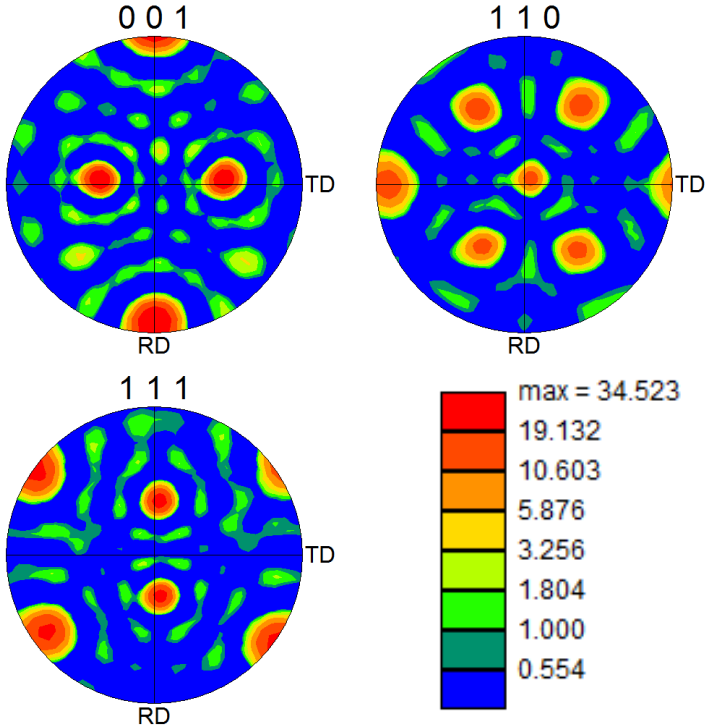

Figure A.8. Pole figures for the beta phase in the Ti-64 β-annealed microstructure longitudinal face.

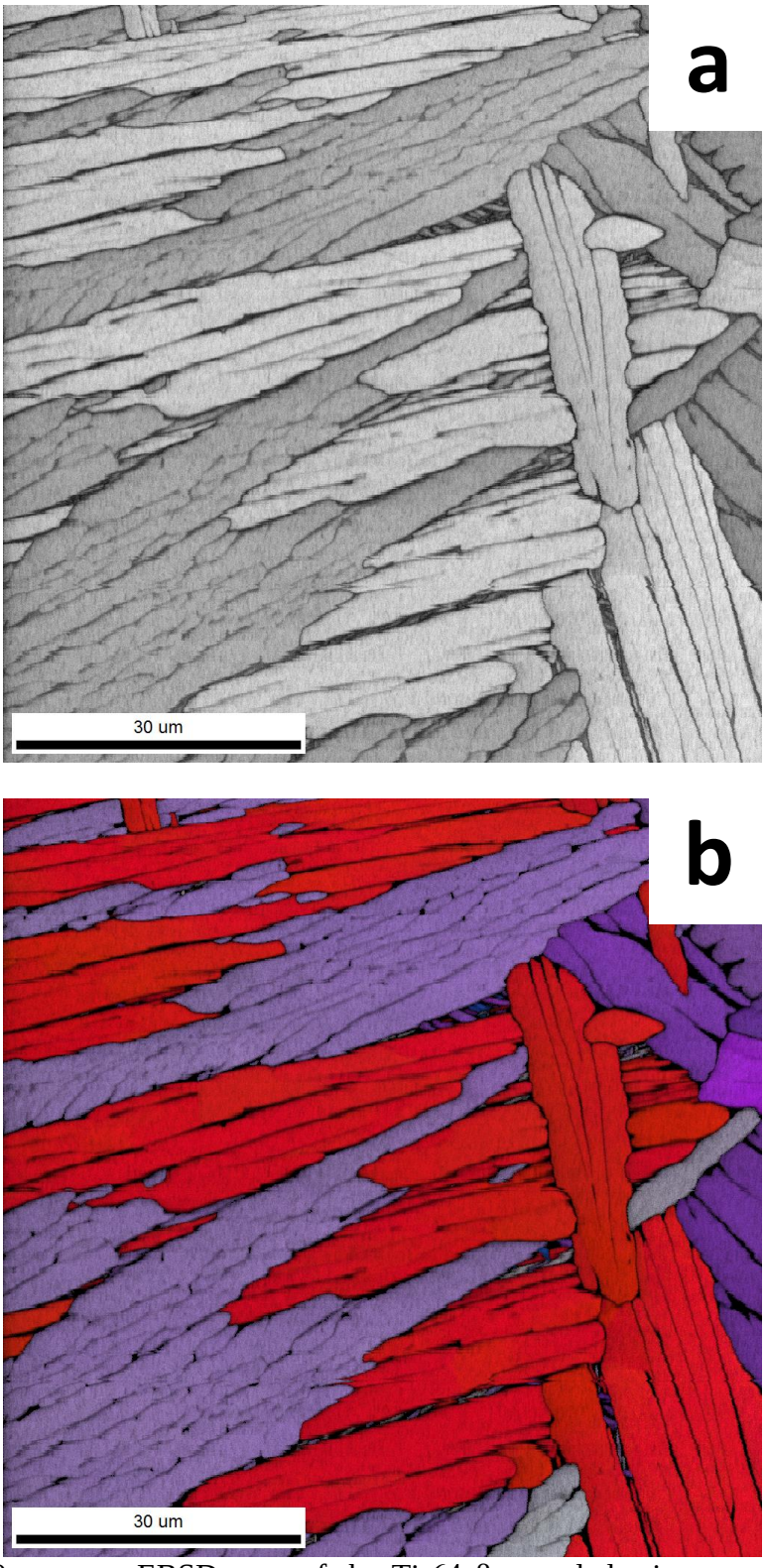

Figure A.9. 60 nm step EBSD scan of the Ti-64 β-annealed microstructure transverse face (a) micrograph and (b) texture colormap.

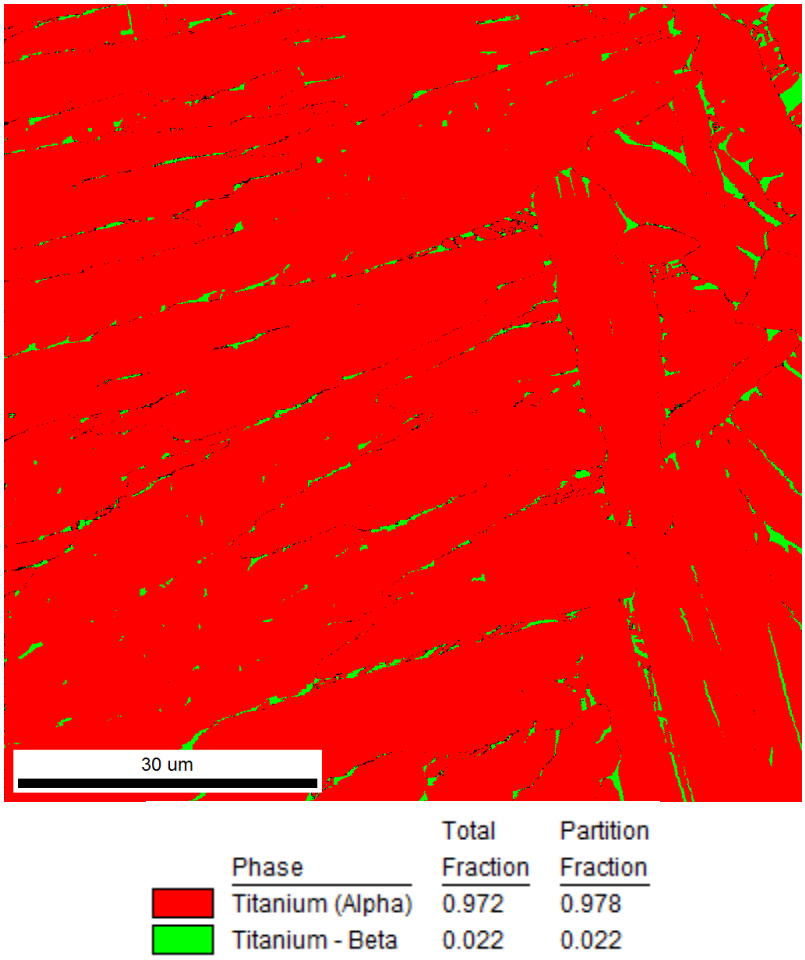

Figure A.10. Phase map for a very high resolution, 60 nm step size EBSD scan of the transverse section face of the Ti-64 β-annealed microstructure.

APPENDIX B

TI-18 STA EBSD CHARACTERIZATION

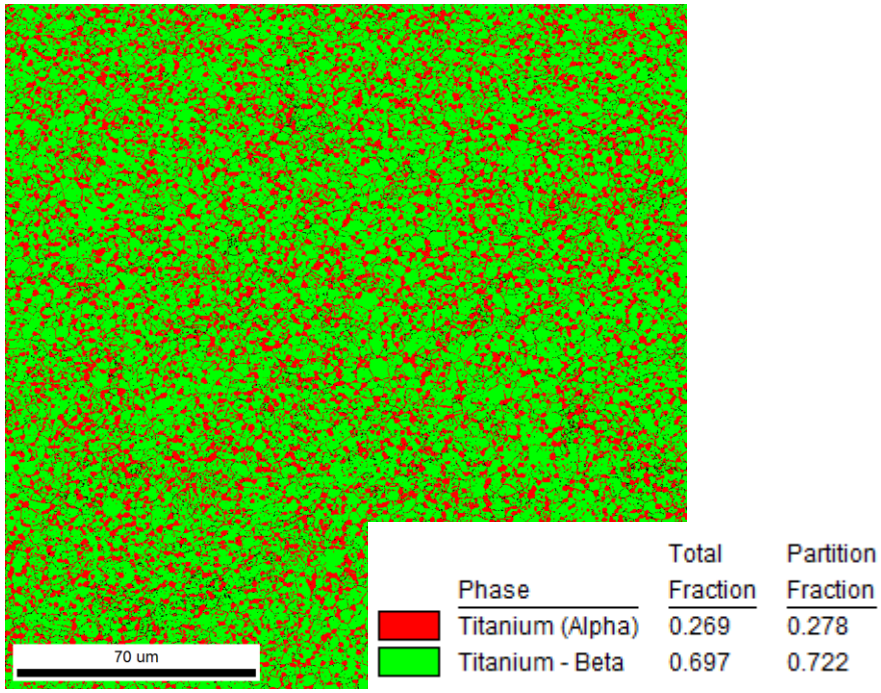

Figure B.1. Phase map for the Ti-18 STA microstructure transverse face for an EBSD scan with 0.2 μm step size.

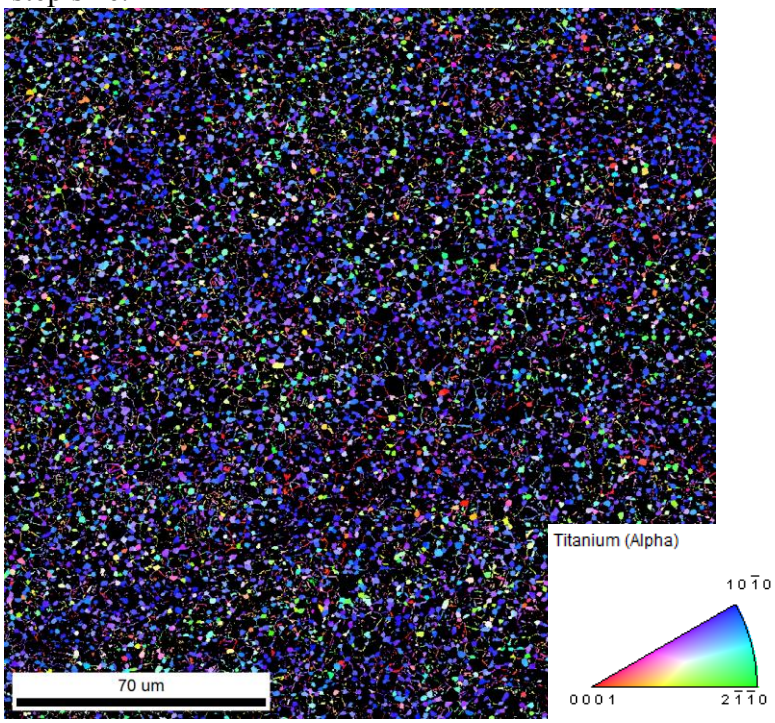

Figure B.2. α-phase texture colormap for the TI-18 STA microstructure transverse face scanned with a 0.2 μm step size.

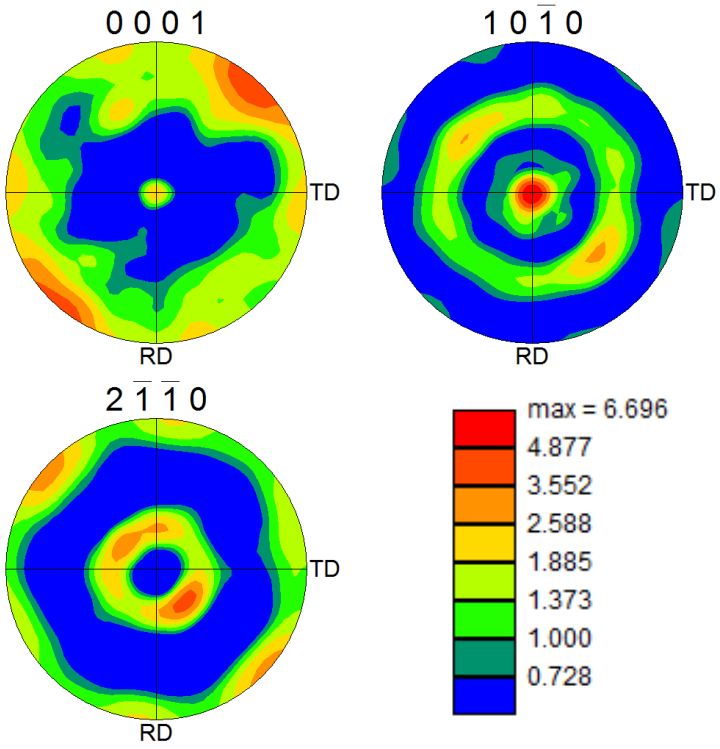

Figure B.3. Alpha phase pole figures for the Ti-18 STA transverse view.

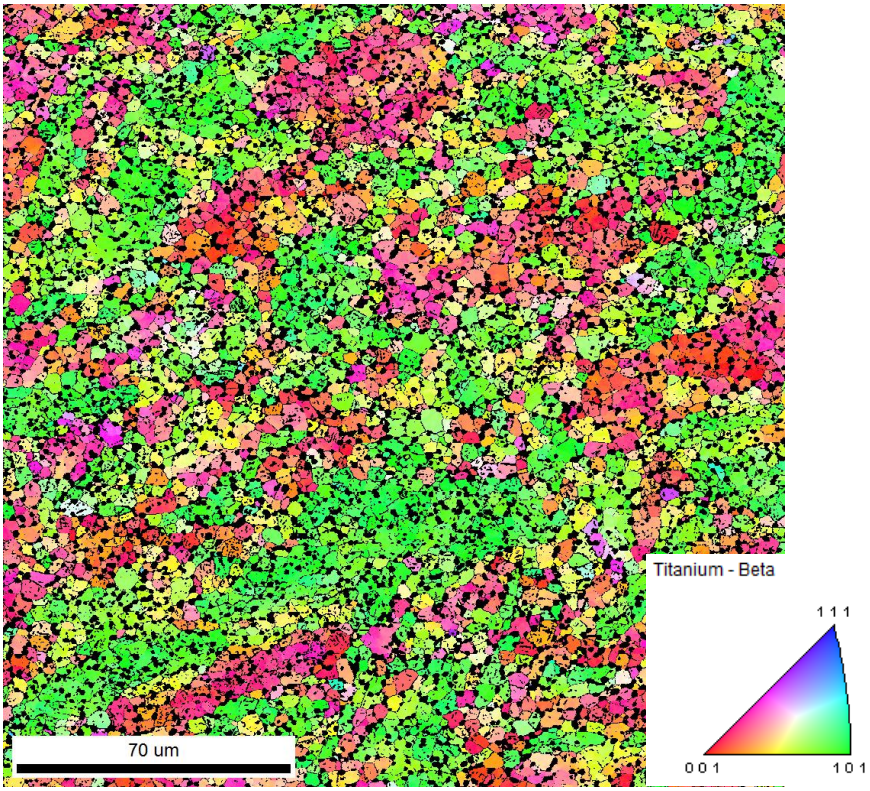

Figure B.4. Beta phase texture colormap for the Ti-18 STA transverse view collected with a 0.2 μm step size.

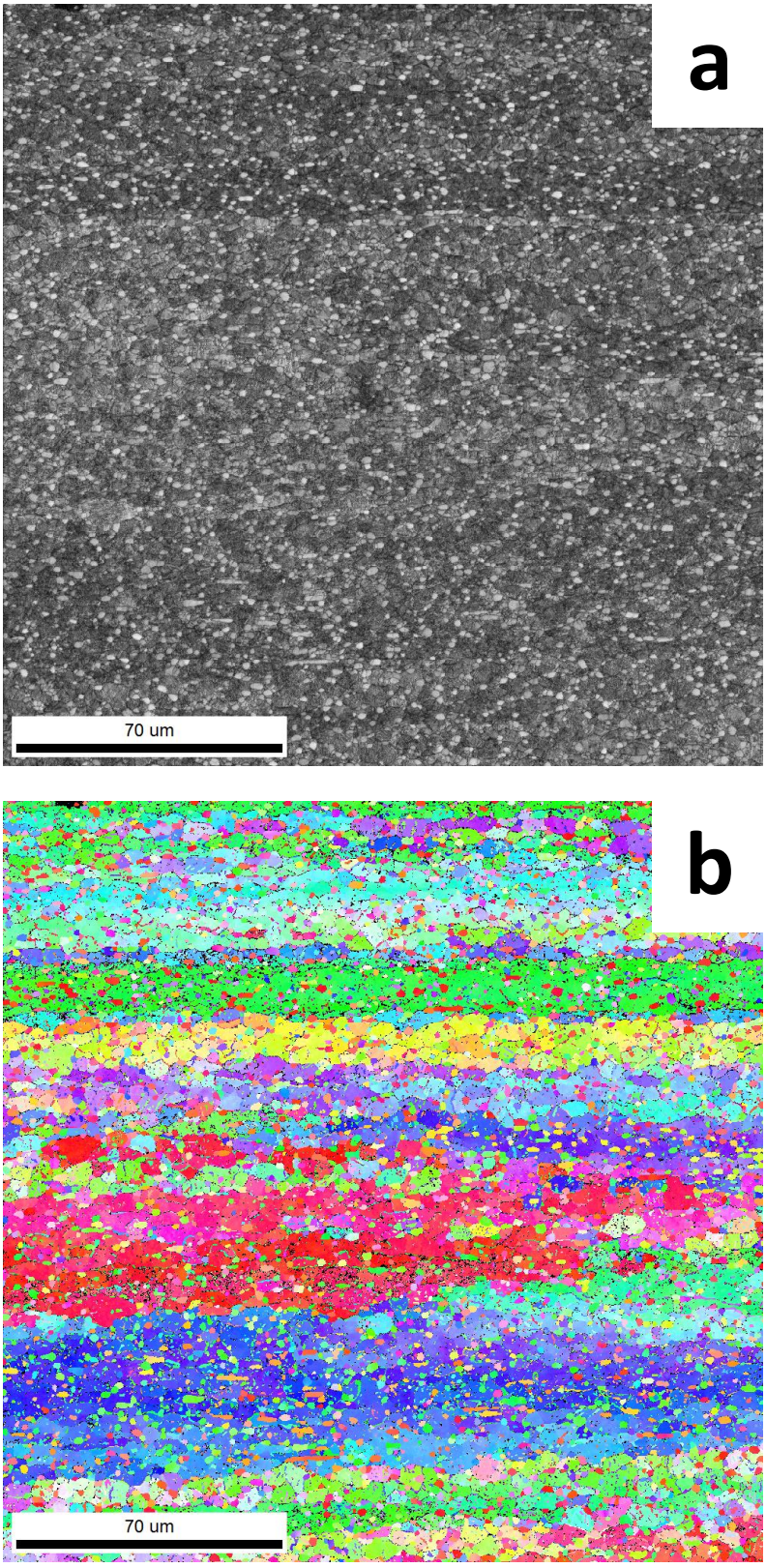

Figure B.5. EBSD scan of the Ti-64 β-annealed microstructure longitudinal cross-section face (a) micrograph and (b) texture colormap scanned with a 0.2 μm step size.

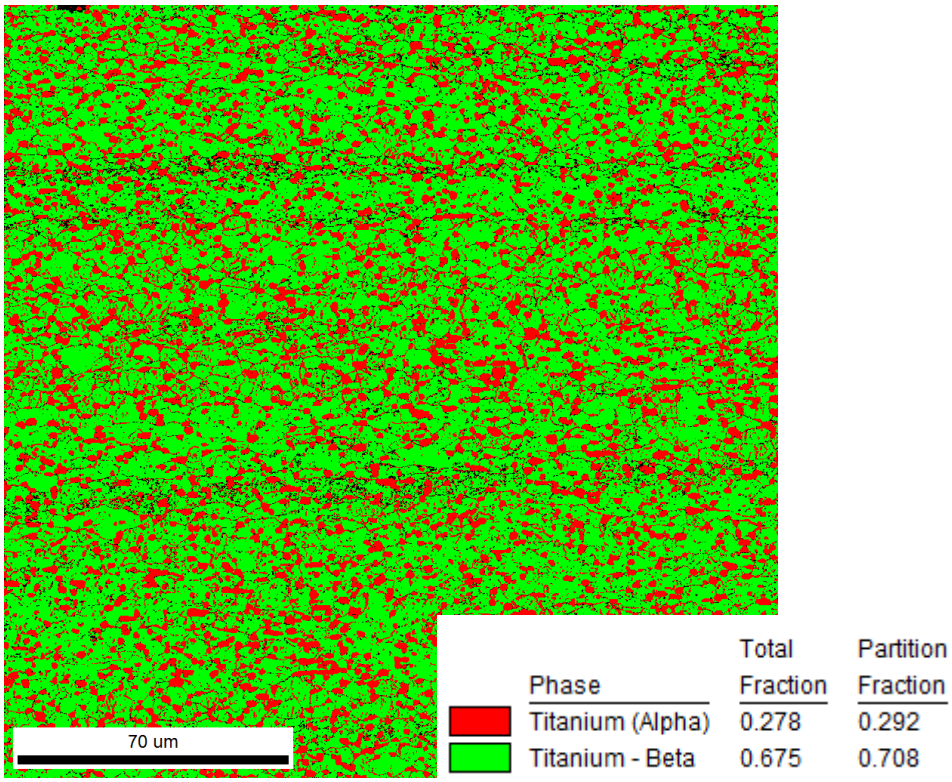

Figure B.6. Phase map for the longitudinal face of the Ti-18 STA microstructure.

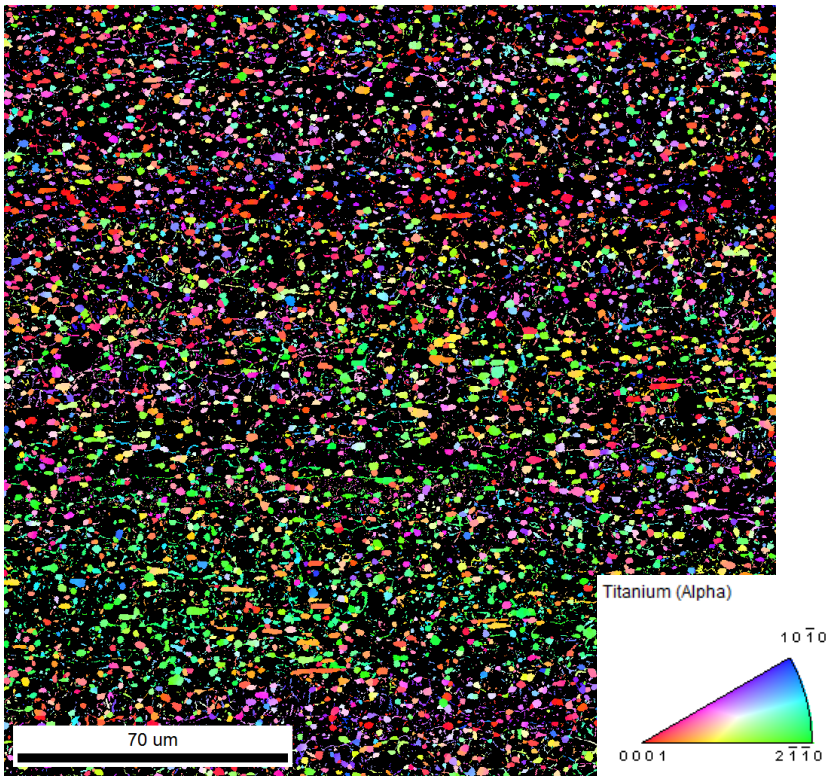

Figure B.7. A texture colormap of the alpha phase for the longitudinal face of the Ti-18 STA microstructure with an EBSD scan step size of 0.2 μm.

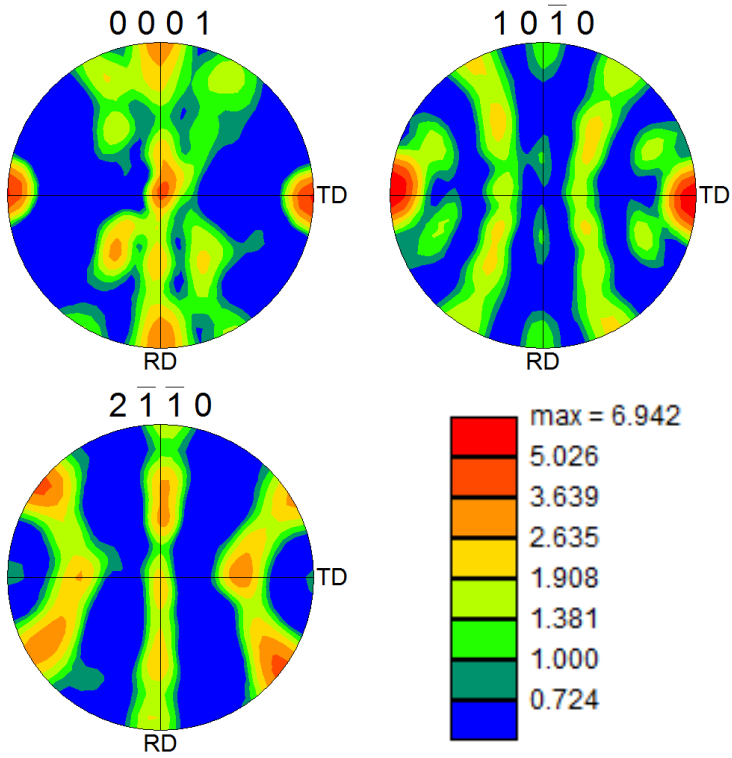

Figure B.8. Pole figures for the alpha phase of the longitudinal view of the Ti-18 STA microstructure.

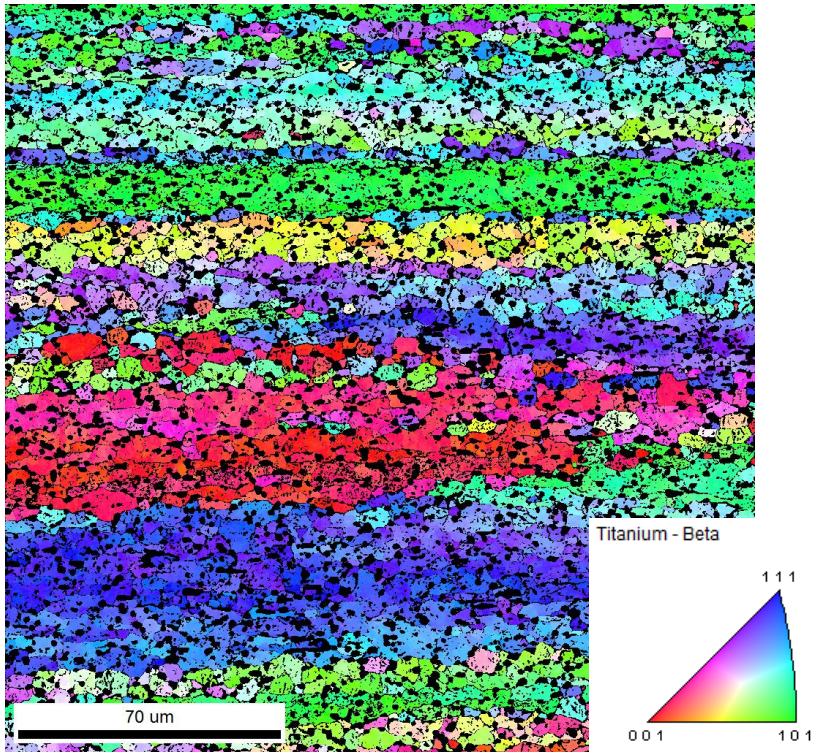

Figure B.9. Texture colormap for the beta phase in the Ti-18 STA microstructure longitudinal face scanned at a 0.2 μm step size.

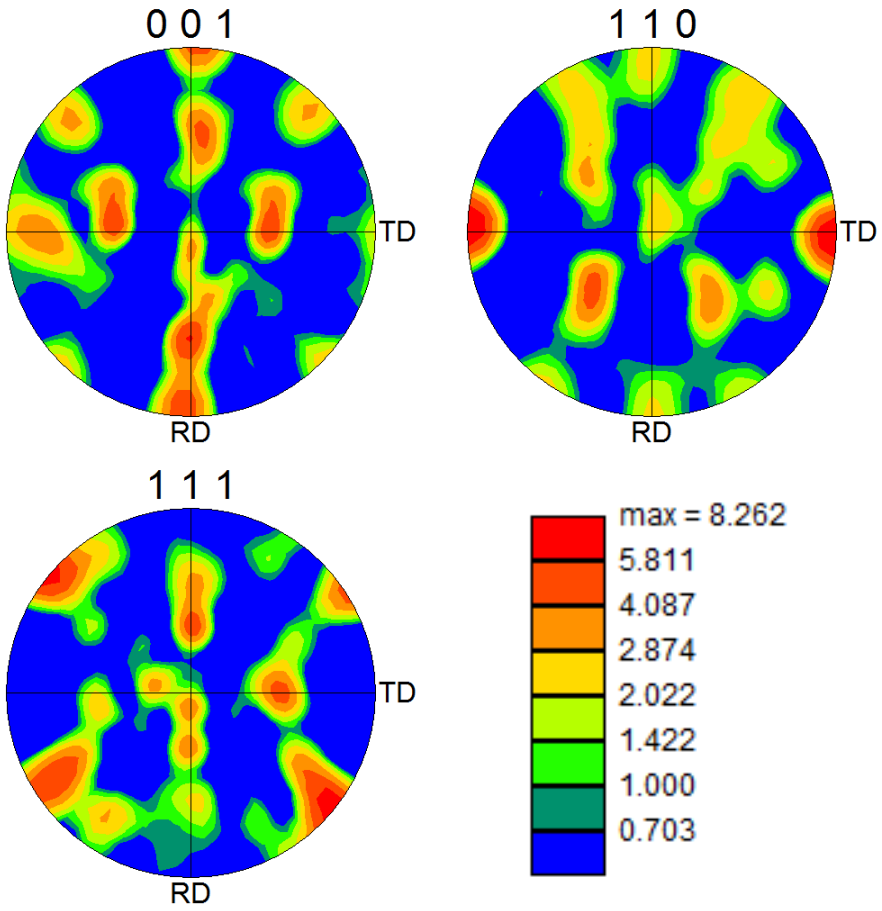

Figure B.10. Beta phase pole figures for the Ti-18 STA microstructure longitudinal face.

APPENDIX C

TI-18 BASCA EBSD CHARACTERIZATION

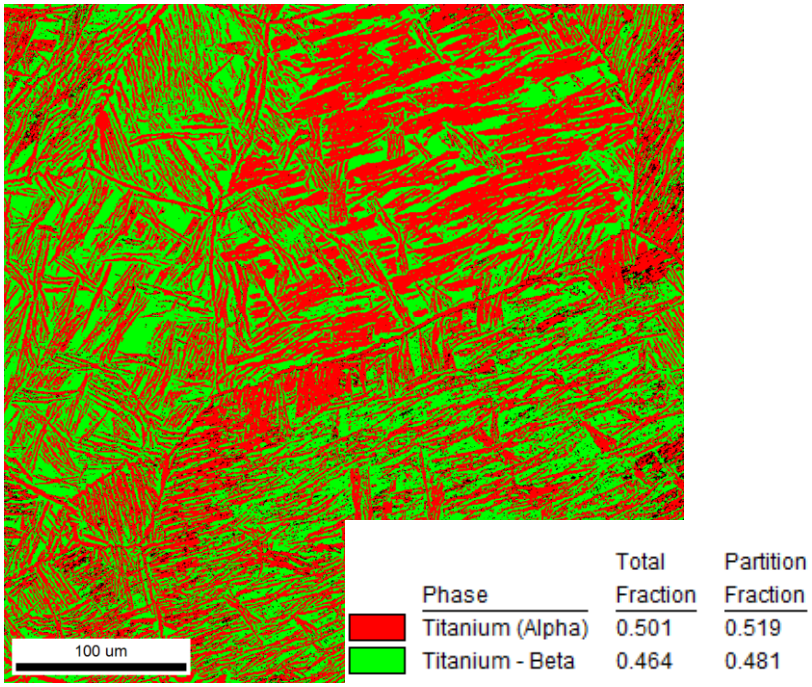

Figure C.1. Phase mapping for the transverse face of the Ti-18 BASCA microstructure scanned at a 0.4 μm step size.

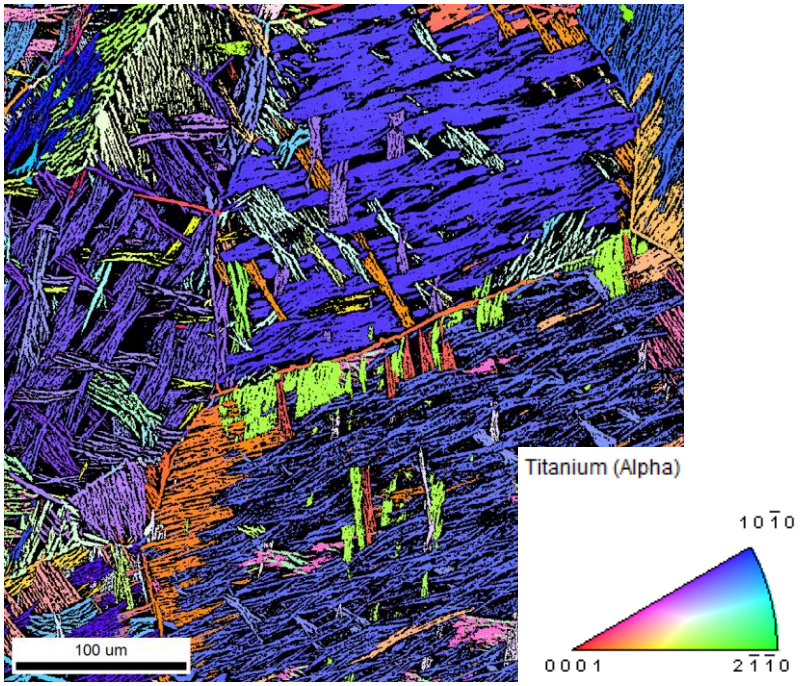

Figure C.2. Alpha phase texture colormap for the Ti-18 BASCA microstructure collected with a 0.4 μm step size.

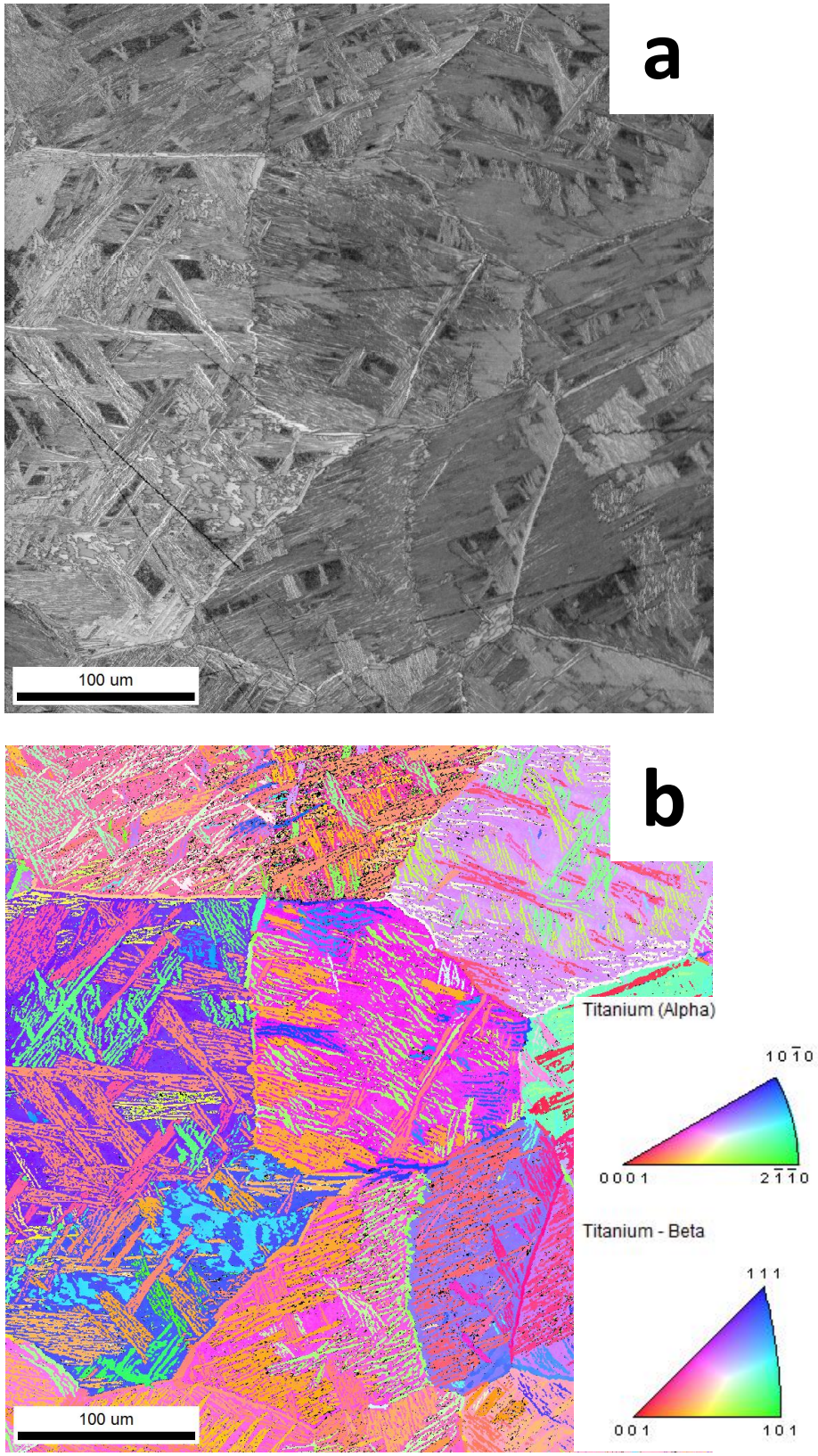

Figure C.3. Ti-18 BASCA microstructure longitudinal view (a) micrograph and (b) texture colormap scanned with a 0.4 μm step size.

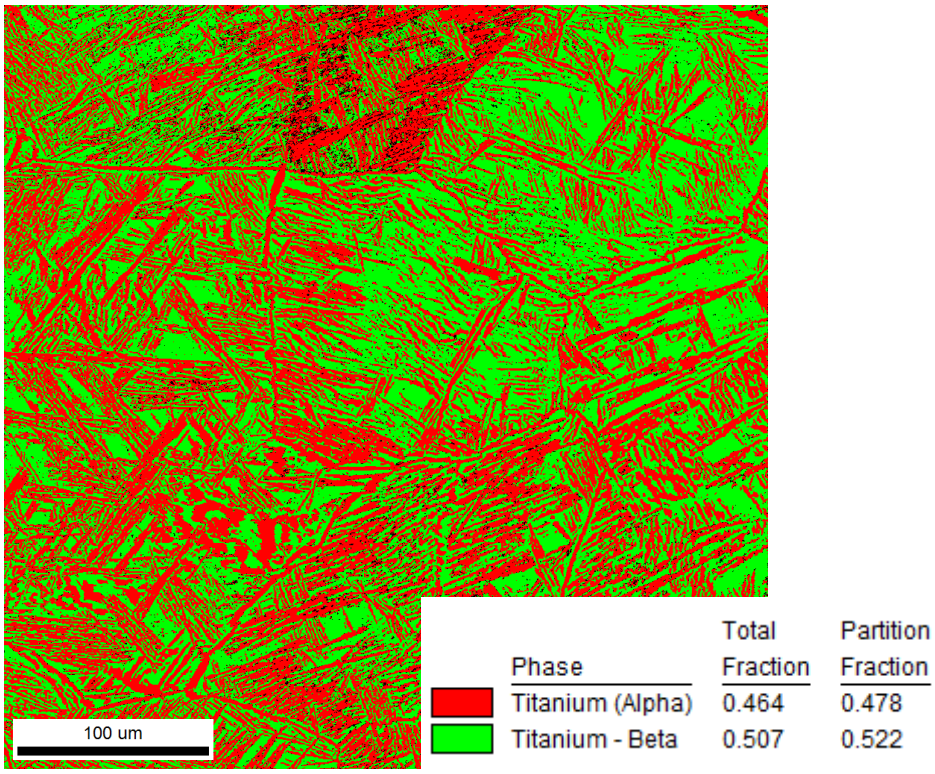

Figure C.4. Phase map for the longitudinal view of the Ti-18 BASCA microstructure scanned with a 0.4 μm step size.

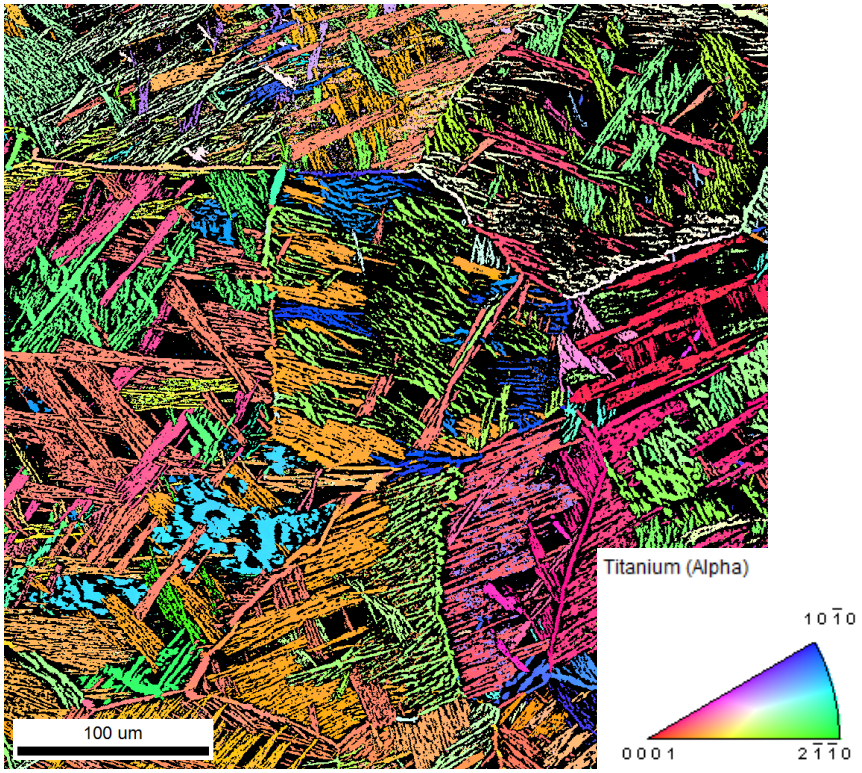

Figure C.5. Alpha phase texture colormap for the longitudinal section of the Ti-18 BASCA microstructure scanned with a 0.4 μm step size.

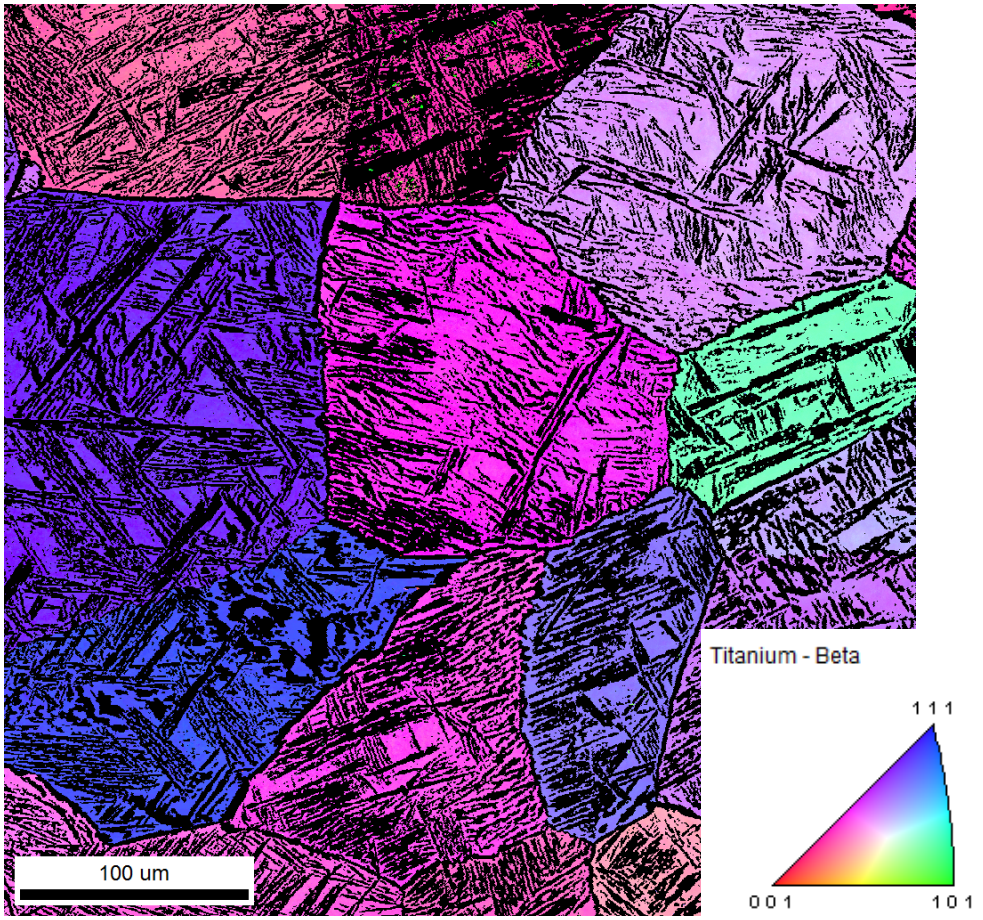

Figure C.6. Beta phase texture colormap for the longitudinal section of the Ti-18 BASCA microstructure collected with a 0.4 μm step size.

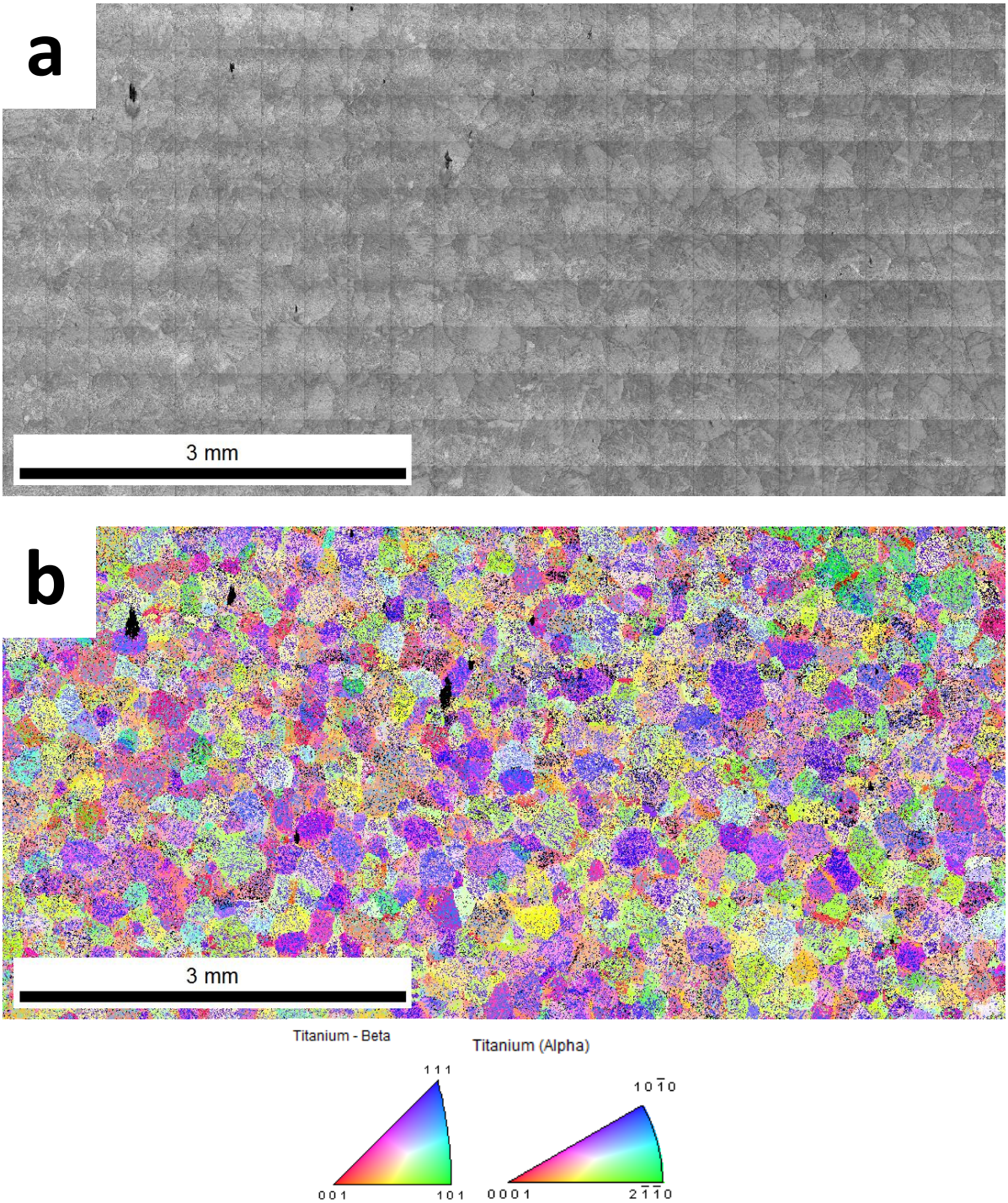

Figure C.7. A (a) micrograph and (b) texture color-map of a large area scan of the transverse cross-section of the Ti-18 BASCA microstructure with an EBSD scan size of 5 μm.

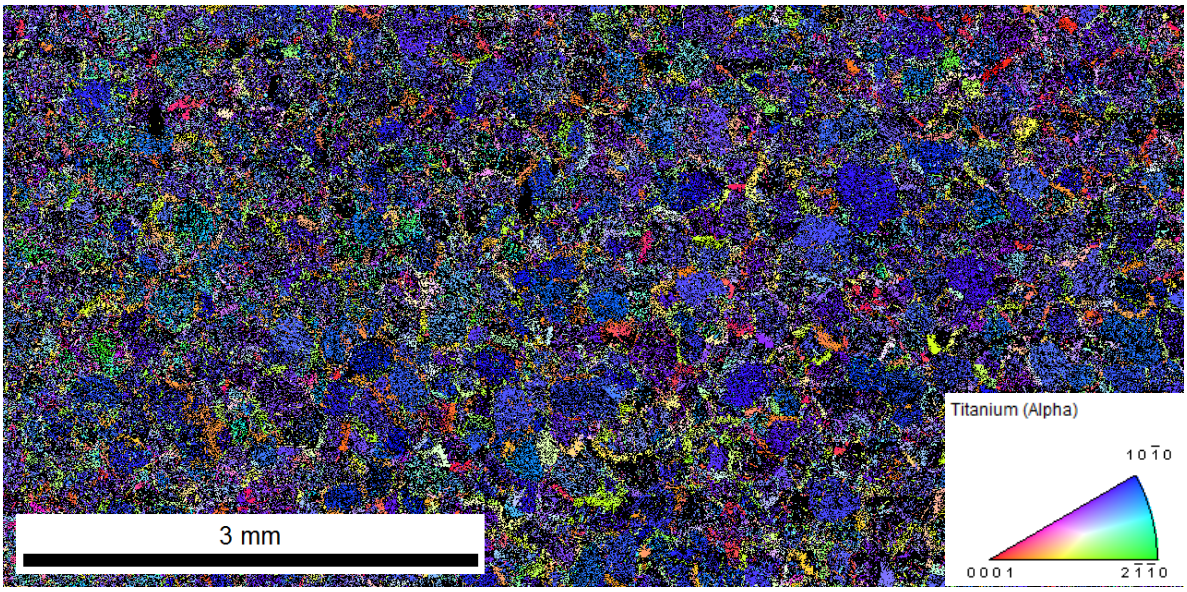

Figure C.8. An alpha phase texture colormap for the large area Ti-18 BASCA transverse EBSD scan with a 5 μm step size.

REFERENCES

ABAQUS. (2011), "FEM software V6.11, Simulia Corp., Providence, RI, USA".

Ankem, S. and Margolin, H. (1980), "The role of elastic interaction stresses on the onset of plastic flow for oriented two ductile phase structures", *Metallurgical Transactions A*, Vol. 11 No. 6, pp. 963–972.

Armstrong, P.J. and Frederick, C.O. (1966), "A mathematical representation of the multiaxial Bauschinger effect", *Central Electricity Generating Board*, Vol. Report RD/B/N, p. 731.

Asaro, R.J. (1983), "Micromechanics of Crystals and Polycrystals", in Hutchinson, J.W. and Wu, T.Y. (Eds.),*Advances in Applied Mechanics*, Elsevier, Vol. Volume 23, pp. 1–115.

ASTM-E606. (2004), "Standard Practice for Strain-Controlled Fatigue Testing", *ASTM International*.

Bache, M.R. and Evans, W.J. (2001), "Impact of texture on mechanical properties in an advanced titanium alloy", *Materials Science and Engineering: A*, Vol. 319-321, pp. 409–414.

Bachmann, F., Hielscher, R. and Schaeben, H. (2010), "Texture Analysis with MTEX - Free and Open Source Software Toolbox", *Solid State Phenomena*, Vol. 160, pp. 63–68.

Basquin, O.H. (1910), "The exponential law of endurance tests", *Proceedings of the American Society for Testing and Materials*, Vol. 10 No. 2.

Bassani, J.L., Ito, K. and Vitek, V. (2001), "Complex macroscopic plastic flow arising from non-planar dislocation core structures", *Materials Science and Engineering: A*, Vol. 319–321, pp. 97–101.

Begley, J.A. and Landes, J.D. (1972), "The J-Integral as a fracture criterion", *American Society for Testing and Materials*, Vol. STP No. 514, pp. 1–20.

Le Biavant, K., Pommier, S. and Prioul, C. (2002), "Local texture and fatigue crack initiation in a Ti-6Al-4V titanium alloy", *Fatigue & Fracture of Engineering Materials & Structures*, Vol. 25 No. 6, pp. 527–545.

Bocher, P., Jahazi, M., Germain, L., Wanjara, P., Gey, N. and Humbert, M. (2005), "β Microtexture Analysis in Correlation with HCP Textured Regions Observed in a Forged Near Alpha Titanium Alloy", *Solid State Phenomena*, Vol. 105, pp. 127–132.

Boyer, R. and Briggs, R. (2005), "The use of β titanium alloys in the aerospace industry", *Journal of Materials Engineering and Performance*, Vol. 14, pp. 681–685.

Boyer, R.R. (1996), "An overview on the use of titanium in the aerospace industry", *Materials Science and Engineering: A*, Vol. 213 No. 1–2, pp. 103–114.

Bridier, F., McDowell, D.L., Villechaise, P. and Mendez, J. (2009), "Crystal plasticity modeling of slip activity in Ti–6Al–4V under high cycle fatigue loading", *International Journal of Plasticity*, Vol. 25, pp. 1066–1082.

Bridier, F., Villechaise, P. and Mendez, J. (2008), "Slip and fatigue crack formation processes in an α/β titanium alloy in relation to crystallographic texture on different scales", *Acta Materialia*, Vol. 56 No. 15, pp. 3951–3962.

Britt, S., McDowell, D. and Garmestani, H. (2011), *Internal communication*.

Brown, M.W. and Miller, K.J. (1973), "A Theory for Fatigue Under Multiaxial Stress-Strain Conditions", *Proceedings of the Institute of Mechanical Engineers*, Vol. 187, p. 1988.

Castelluccio, G.M. and McDowell, D.L. (2012), "Assessment of small fatigue crack growth driving forces in single crystals with and without slip bands", *International Journal of Fracture*, Vol. 176 No. 1, pp. 49–64.

Chesnutt, J.C., Thompson, A.W. and Williams, J.C. (1980), "Fatigue Crack Propagation and Fracture of Titanium Alloys", *Titanium '80 Science and Technology*, Vol. 3, pp. 1875–1882.

Coffin, L.F. (1954), "A study of the Effects of Cyclic Thermal Stresses on a Ductile Metal", *Trans ASME*, Vol. 76, pp. 931–950.

Cottrell, A.H. and Hull, D. (1957), "Extrusion and Intrusion by Cyclic Slip in Copper", *Proceedings of the Royal Society of London. Series A. Mathematical and Physical Sciences*, Vol. 242 No. 1229, pp. 211–213.

Dunne, F.P.E. and Rugg, D. (2008), "On the mechanisms of fatigue facet nucleation in titanium alloys", *Fatigue & Fracture of Engineering Materials & Structures*, Vol. 31 No. 11, pp. 949–958.

Dunne, F.P.E., Rugg, D. and Walker, A. (2007), "Lengthscale-dependent, elastically anisotropic, physically-based hcp crystal plasticity: Application to cold-dwell fatigue in Ti alloys", *International Journal of Plasticity*, Vol. 23 No. 6, pp. 1061–1083.

Dunne, F.P.E., Wilkinson, A.J. and Allen, R. (2007), "Experimental and computational studies of low cycle fatigue crack nucleation in a polycrystal", *International Journal of Plasticity*, Vol. 23 No. 2, pp. 273–295.

Evans, W.J. (1987), "Dwell-sensitive fatigue in a near alpha-titanium alloy", *Journal of Materials Science Letters*, Vol. 6 No. 5, pp. 571–574.

Evans, W.J. and Gostelow, C.R. (1979), "The effect of hold time on the fatigue properties of a β-processed titanium alloy", *Metallurgical Transactions A*, Vol. 10 No. 12, pp. 1837–1846.

Ewing, J.A. and Humfrey, J.C.W. (1903), "The Fracture of Metals under Repeated Alternations of Stress", *Philosophical Transactions of the Royal Society of London. Series A, Containing Papers of a Mathematical or Physical Character*, Vol. 200, pp. 241–250.

Eylon, D. (1979), "Faceted fracture in beta annealed titanium alloys", *Metallurgical Transactions A,* Vol. 10 No. 3, pp. 311–317.

Eylon, D. and Bania, P.J. (1978), "Fatigue cracking characteristics of β-annealed large colony Ti-11 alloy", *Metallurgical Transactions A,* Vol. 9 No. 9, pp. 1273–1279.

Eylon, D. and Hall, J. (1977), "Fatigue behavior of beta processed titanium alloy IMI 685", *Metallurgical and Materials Transactions A,* Vol. 8 No. 6, pp. 981–990.

Eylon, D., Hall, J.A., Pierce, C.M. and Ruckle, D.L. (1976), "Microstructure and mechanical properties relationships in the Ti-11 alloy at room and elevated temperatures", *Metallurgical Transactions A,* Vol. 7 No. 12, pp. 1817–1826.

Eylon, D. and Pierce, C.M. (1976), "Effect of microstructure on notch fatigue properties of Ti-6Al-4V", *Metallurgical Transactions A,* Vol. 7 No. 1, pp. 111–121.

Fanning, J. (2011), "Recent Developments in High-Strength Near-Beta Titanium Alloys", Presented at the Titanium 2011 Conference, San Diego, California.

Fast, T. and Kalidindi, S.R. (2011), "Formulation and calibration of higher-order elastic localization relationships using the MKS approach", *Acta Materialia,* Vol. 59 No. 11, pp. 4595–4605.

Fatemi, A. and Kurath, P. (1988), "Multiaxial Fatigue Life Predictions Under the Influence of Mean-Stresses", *Journal of Engineering Materials and Technology-Transactions of the ASME,* Vol. 110 No. 4, p. 380.

Fatemi, A. and Socie, D. (1988), "A Critical Plane Approach to Multiaxial Fatigue Damage Including Out-of-Phase Loading", *Fatigue & Fracture of Engineering Materials & Structures,* Vol. 11, pp. 149–165.

Fernandez-Zelaia, P. (2012), *Thermomechanical Fatigue Crack Formation in Nickel-Base Superalloys at Notches* (Master's Thesis), Georgia Institute of Technology, Atlanta, GA.

Filip, R., Kubiak, K., Ziaja, W. and Sieniawski, J. (2003), "The effect of microstructure on the mechanical properties of two-phase titanium alloys", *Journal of Materials Processing Technology,* Vol. 133 No. 1–2, pp. 84–89.

Findley, W.N. (1959), "A Theory for the Effect for Mean Stress on Fatigue of Metals Under Combined Torsion and Axial Load or Bending", *Journal of Engineering for Industry-Transactions of the ASME,* Transactions of the ASME, Vol. 81, pp. 301–306.

Forsyth, P.J. (1962), "A two stage process of fatigue crack growth", *Crack Propagation: Proceedings of Cranfield Symposium,* London, pp. 76–94.

Forsyth, P.J.E. (1953), "Exudation of Material from Slip Bands at the Surface of Fatigued Crystals of an Aluminium–Copper Alloy", *Nature,* Vol. 171 No. 4343, pp. 172–173.

Forsyth, P.J.E. and Ryder, D.A. (1960), "Fatigue Fracture: Some Results Derived from the Microscopic Examination of Crack Surfaces", *Aircraft Engineering and Aerospace Technology,* Vol. 32 No. 4, pp. 96–99.

Forsyth, P.J.E. and Stubbington, C.A. (1955), "The Influence of Sub-Structure on the Slip Observed in Pure Aluminium and Some Aluminium Alloys When Subjected to Fatigue Stresses", *Journal of the Institute of Metals*, Vol. 84, pp. 173–175.

Fowler, D.B. (1989), "A method of determining the interlamellar spacing of pearlite using digital image analysis", *Microstructural science*, Presented at the International Metallographic Society Annual technical meeting. 21, Elsevier, Toronto, Canada, Vol. 17, pp. 81–90.

Gallagher, J., Nicholas, T., Gunderson, A., Ruschau, J., Miedlar, P., Hutson, A., Hardy, G., et al. (2004), *Advanced High Cycle Fatigue (HCF) Life Assurance Methodologies* (No. AFRL-ML-WP-TR-2005-4102).

Gerber, H. (1874), "Bestimmung der zulassigen Spannungen in Eisen-konstructionen", *Zeitschrift des Bayerischen Architeckten und Ingenieur-Vereins*, Vol. 6, pp. 101–110.

Germain, L., Gey, N., Humbert, M., Bocher, P. and Jahazi, M. (2005), "Analysis of sharp microtexture heterogeneities in a bimodal IMI 834 billet", *Acta Materialia*, Vol. 53 No. 13, pp. 3535–3543.

Germain, L., Gey, N., Humbert, M., Vo, P., Jahazi, M. and Bocher, P. (2008), "Texture heterogeneities induced by subtransus processing of near α titanium alloys", *Acta Materialia*, Vol. 56 No. 16, pp. 4298–4308.

Gey, N., Bocher, P., Uta, E., Germain, L. and Humbert, M. (2012), "Texture and microtexture variations in a near-α titanium forged disk of bimodal microstructure", *Acta Materialia*, Vol. 60 No. 6–7, pp. 2647–2655.

Glavicic, M.G., Bartha, B.B., Jha, S.K. and Szczepanski, C.J. (2009), "The origins of microtexture in duplex Ti alloys", *Materials Science and Engineering: A*, Vol. 513–514, pp. 325–328.

Goh, C.-H. (2002), *Crystallographic plasticity in fretting of Ti-6Al-4V* (Ph.D. Thesis), Georgia Institute of Technology, Atlanta, GA.

Goh, C.-H., Neu, R.W. and McDowell, D.L. (2003), "Crystallographic plasticity in fretting of Ti–6AL–4V", *International Journal of Plasticity*, Vol. 19, pp. 1627–1650.

Goh, C.-H., Wallace, J.M., Neu, R.W. and McDowell, D.L. (2001), "Polycrystal plasticity simulations of fretting fatigue", *International Journal of Fatigue*, Vol. 23 No. 1, pp. 423–435.

Goodman, J. (1899), *Mechanics Applied to Engineering*, Longmans Green, London.

Griffith, A.A. (1921), "The Phenomena of Rupture and Flow in Solids", *Philosophical Transactions of the Royal Society of London. Series A, Containing Papers of a Mathematical or Physical Character*, Vol. 221, pp. 163–198.

Gumbel, E.J. (1958), *Statistics of extremes*, Columbia University Press, New York.

Gysler, A. and Lütjering, G. (1982), "Influence of test temperature and microstructure on the tensile properties of titanium alloys", *Metallurgical Transactions A*, Vol. 13 No. 8, pp. 1435–1443.

Haldar, A. (2000), *Probability, reliability, and statistical methods in engineering design*, John Wiley, New York :

Hasija, V., Ghosh, S., Mills, M.J. and Joseph, D.S. (2003), "Deformation and creep modeling in polycrystalline Ti–6Al alloys", *Acta Materialia*, Vol. 51 No. 15, pp. 4533–4549.

Hollomon, J.H. and Zener, C. (1946), "Problems in Fracture of Metals", *Journal of Applied Physics*, Vol. 17 No. 2, pp. 82–90.

Horálek, V. (1990), "ASTM grain-size model and related random tessellation models", *Materials Characterization*, Vol. 25 No. 3, pp. 263–284.

Huang, J., Wang, Z. and Xue, K. (2011), "Cyclic deformation response and micromechanisms of Ti alloy Ti–5Al–5V–5Mo–3Cr–0.5Fe", *Materials Science and Engineering: A*, Vol. 528, pp. 8723–8732.

Inglis, C.E. (1913), "Stresses in a Plate Due to the Presence of Cracks and Sharp Corners", *Transactions of the Institute of Naval Architects*, Vol. 55, pp. 219–241.

Irwin, G.R. (1948), "Fracture dynamics", *Fracturing of metals*, Vol. 147, p. 166.

Irwin, G.R. (1956), "Onset of Fast Crack Propagation in High Strength Steel and Aluminum Alloys", *Sagamore Research Conference Proceedings*, Vol. 2, pp. 289–305.

Irwin, G.R. (1957), "Analysis of stresses and strains near the end of a crack traversing a plate", *Journal of Applied Mechanics*, Vol. 24.

Ivasishin, O.M., Markovsky, P.E., Matviychuk, Y.V., Semiatin, S.L., Ward, C.H. and Fox, S. (2008), "A comparative study of the mechanical properties of high-strength β-titanium alloys", *Journal of Alloys and Compounds*, Vol. 457 No. 1–2, pp. 296–309.

Juvinall, R.C. and Marshek, K.M. (1991), *Fundamentals of Machine Component Design*, John Wiley and Sons, New York, 2nded.

Kalidindi, S.R. (1998), "Incorporation of deformation twinning in crystal plasticity models", *Journal of the Mechanics and Physics of Solids*, Vol. 46 No. 2, pp. 267–290.

Kalidindi, S.R., Niezgoda, S.R., Landi, G., Vachhani, S. and Fast, T. (2010), "A Novel Framework for Building Materials Knowledge Systems", *Computers, Materials, & Continua*, Vol. 17 No. 2, pp. 103–125.

Kim, S.M., Kim, J., Shin, D.H., Ko, Y.G., Lee, C.S. and Semiatin, S.L. (2004), "Microstructure development and segment formation during ECA pressing of Ti–6Al–4V alloy", *Scripta Materialia*, Vol. 50 No. 7, pp. 927–930.

Kirane, K. and Ghosh, S. (2008), "A cold dwell fatigue crack nucleation criterion for polycrystalline Ti-6242 using grain-level crystal plasticity FE Model", *International Journal of Fatigue*, Vol. 30 No. 12, pp. 2127–2139.

Kocks, U.F., Argon, A.S. and Ashby, M.F. (1975), "Thermodynamics and kinetics of slip", *Progress in Materials Science*, Vol. 19.

Kung, C.Y. and Fine, M.E. (1979), "Fatigue Crack initiation and microcrack growth in 2024-T4 and 2124-T4 aluminum alloys", *Metallurgical Transactions A*, Vol. 10 No. 5, pp. 603–610.

Kurath, P. (1999), *Final Report: Biaxial fatigue of Ti-6-4 at 20 deg C.* (No. UIUC #1-5-521170).

Laird, C. (1967), "The influence of metallurgical structure on the mechanisms of fatigue crack propagation", *Fatigue Crack Propagation*, The American Society for Testing and Materials, Philadelphia, Vol. Special Technical Publication 415, pp. 131–168.

Lankford, J. and Kusenberger, F.N. (1973), "Initiation of fatigue cracks in 4340 steel", *Metallurgical Transactions*, Vol. 4 No. 2, pp. 553–559.

Lederich, R.J., Sastry, S.M.L., O'Neal, J.E. and Rath, B.B. (1978), "The effect of grain size on yield stress and work hardening of polycrystalline titanium at 295 K and 575 K", *Materials Science and Engineering*, Vol. 33 No. 2, pp. 183–188.

Lee, D.-G., Lee, S., Lee, C. and Hur, S. (2003), "Effects of microstructural factors on quasi-static and dynamic deformation behaviors of Ti-6Al-4V alloys with widmanstätten structures", *Metallurgical and Materials Transactions A*, Vol. 34 No. 11, pp. 2541–2548.

Lehr, P. (1980), "Microscopic Features of Fractures and Crack Propagation of Titanium Alloys", *Titanium '80 Science and Technology*, Vol. 3, pp. 1617–1626.

Lin, F.S., Starke, E.A., Chakrabortty, S.B. and Gysler, A. (1984), "The effect of microstructure on the deformation modes and mechanical properties of Ti-6Al-2Nb-1Ta-0.8Mo: Part I. Widmanstätten structures", *Metallurgical Transactions A*, Vol. 15 No. 6, pp. 1229–1246.

Lloyd, D.J. (1991), "Aspects of fracture in particulate reinforced metal matrix composites", *Acta Metallurgica et Materialia*, Vol. 39 No. 1, pp. 59–71.

Lütjering, G. (1998), "Influence of processing on microstructure and mechanical properties of (α+β) titanium alloys", *Materials Science and Engineering: A*, Vol. 243, pp. 32–45.

Lütjering, G. (1999), "Property optimization through microstructural control in titanium and aluminum alloys", *Materials Science and Engineering: A*, Vol. 263 No. 2, pp. 117–126.

Lütjering, G. (2003), *Titanium*, Springer, Berlin; New York, 2nded.

Lütjering, G. and Gysler, A. (1995), "Critical Review", *Titanium '95 Science and Technology*, Vol. 4, pp. 2065–2084.

Ma, B.-T. and Laird, C. (1989), "Overview of fatigue behavior in copper single crystals—I. Surface morphology and stage I crack initiation sites for tests at constant strain amplitude", *Acta Metallurgica,* Vol. 37 No. 2, pp. 325–336.

Manson, S.S. (1954), *Behavior of materials under connditions of thermal stress* (No. 1170), Cleveland: Lewis Flight Propulsion Laboratory: National Advisory Commision on Aeronautics.

Maruyama, K., Suzuki, G., Kim, H.Y., Suzuki, M. and Sato, H. (2002), "Saturation of yield stress and embrittlement in fine lamellar TiAl alloy", *Materials Science and Engineering: A,* Vol. 329–331 No. 0, pp. 190–195.

MATLAB. (2011), "R2011a, The Mathworks, Inc., Natick, MA, USA".

Mayeur, J.R. (2004), *Three dimensional modeling of Ti-Al alloys with application to attachment fatigue* (Ph.D. Thesis), Georgia Institute of Technology, Atlanta, GA.

Mayeur, J.R. and McDowell, D.L. (2007), "A three-dimensional crystal plasticity model for duplex Ti–6Al–4V", *International Journal of Plasticity,* Vol. 23 No. 9, pp. 1457–1485.

McDowell, D.L. (1996), "Basic issues in the mechanics of high cycle metal fatigue", *International Journal of Fracture,* Vol. 80, pp. 103–145.

McDowell, D.L. (2007), "Simulation-based strategies for microstructure-sensitive fatigue modeling", *Materials Science and Engineering: A,* Vol. 468-470, pp. 4–14.

McDowell, D.L. (2008), "Viscoplasticity of heterogeneous metallic materials", *Materials Science and Engineering: R: Reports,* Vol. 62 No. 3, pp. 67–123.

McDowell, D.L. (2009), "Microstructure-Sensitive Computational Modeling of Fatigue Crack Formation", *ASM Handbook on Fundamentals of Modeling for Metals Processing, Handbook Vol. 22A,* ASM International.

McDowell, D.L. and Berard, J.-Y. (1992), "A δJ-Based Approach to Biaxial Fatigue", *Fatigue & Fracture of Engineering Materials & Structures,* Vol. 15 No. 8, pp. 719–741.

McDowell, D.L. and Dunne, F.P.E. (2010), "Microstructure-sensitive computational modeling of fatigue crack formation", *International Journal of Fatigue,* Vol. 32, pp. 1521–1542.

McDowell, D.L. and Olson, G.B. (2008), "Concurrent design of hierarchical materials and structures", *Scientific Modeling and Simulation SMNS,* Vol. 15 No. 1-3, pp. 207–240.

McGinty, R.D. (2001), *Multiscale representation of polycrystalline inelasticity* (Ph.D. Thesis), Georgia Institute of Technology, Atlanta, GA.

Mecking, H. and Kocks, U. (1981), "Kinetics of flow and strain-hardening", *Acta Mettallurgica,* Vol. 29, pp. 1865–1875.

Miller, K.J. (1993), "Materials science perspective of metal fatigue resistance", *Materials Science and Technology,* Vol. 9, pp. 453–462.

Morrissey, R.J., McDowell, D.L. and Nicholas, T. (2001), "Microplasticity in HCF of Ti–6Al–4V", *International Journal of Fatigue*, Vol. 23 No. 1, pp. 55–64.

Naka, S., Lasalmonie, A., Costa, P. and Kubin, L.P. (1988), "The low-temperature plastic deformation of α-titanium and the core structure of a-type screw dislocations", *Philosophical Magazine A*, Vol. 57 No. 5, pp. 717–740.

Neeraj, T. and Mills, M.J. (2001), "Short-range order (SRO) and its effect on the primary creep behavior of a Ti-6wt.%Al alloy.", *Materials Science and Engineering: A*, Vol. 319-321, pp. 415–419.

Neumann, P. (1969), "Coarse slip model of fatigue", *Acta Metallurgica*, Vol. 17 No. 9, pp. 1219–1225.

Nyakana, S.L., Fanning, J.C. and Boyer, R.R. (2005), "Quick reference guide for β titanium alloys in the 00s", *Journal of Materials Engineering and Performance*, Vol. 14 No. 6, pp. 799–811.

Orowan, E. (1948), "Fracture and Strengths of Solids", *Reports on Progress in Physics*, Vol. 12, pp. 185–232.

Padbidri, J. (2013), "Internal Communication", *Georgia Institute of Technology*.

Paris, P. and Erdogan, F. (1963), "A Critical Analysis of Crack Propagation Laws", *Journal of Fluids Engineering*, Vol. 85 No. 4, pp. 528–533.

Paris, P., Gomez, M. and Anderson, W. (1961), "A rational analytic theory of fatigue", *The Trend in Engineering*, Vol. 13, pp. 9–14.

Park, J. and Nelson, D. (2000), "Evaluation of an energy-based approach and a critical plane approach for predicting constant amplitude multiaxial fatigue life", *International Journal of Fatigue*, Vol. 22 No. 1, pp. 23–39.

Peirce, D., Asaro, R.J. and Needleman, A. (1982), "An analysis of nonuniform and localized deformation in ductile single crystals", *Acta Metallurgica*, Vol. 30 No. 6, pp. 1087–1119.

Perdrix, F., Trichet, M.F., Bonnentien, J.L., Cornet, M. and Bigot, J. (1999), "Influence of cooling rate on microstructure and mechanical properties of a Ti–48Al alloy", *Intermetallics*, Vol. 7 No. 12, pp. 1323–1328.

Peters, M., Gysler, A. and Luetjering, G. (1980), "Influence of Microstructure on the Fatigue Behavior of Ti-1Al-4V", *Proceedings of the Fourth International Conference on Titanium*, Presented at the Titanium '80 Science and Technology, The Metallurgical Society of AIME, Kyoto, Japan, Vol. 3, pp. 1777–1786.

Peters, M., Gysler, A. and Lütjering, G. (1984), "Influence of texture on fatigue properties of Ti-6Al-4V", *Metallurgical and Materials Transactions A*, Vol. 15, pp. 1597–1605.

Picu, R.C. and Majorell, A. (2002), "Mechanical behavior of Ti–6Al–4V at high and moderate temperatures—Part II: constitutive modeling", *Materials Science and Engineering A*, Vol. 326, pp. 306–316.

Plumbridge, W.J. and Stanley, M. (1986), "Low cycle fatigue of a titanium 829 alloy", *International Journal of Fatigue*, Vol. 8 No. 4, pp. 209–216.

Pollock, T.M., Allison, J.E., Backman, D.G., Boyce, M.C., Gersh, M., Holm, E.A., LeSar, R., et al. (2008), *Integrated Computational materials Engineering: A Transformational Discipline for Improved Competitiveness and National Security* (No. ISBN-10: 0-309-11999-5), National Materials Advisory Board, NAE, National Academic Press.

Poncelet, J.V. (1839), *Introduction a la Mecanique Industrielle*, Brussells.

Prasannavenkatesan, R., Przybyla, C.P., Salajegheh, N. and McDowell, D.L. (2011), "Simulated extreme value fatigue sensitivity to inclusions and pores in martensitic gear steels", *Engineering Fracture Mechanics*, Vol. 78 No. 6, pp. 1140–1155.

Przybyla, C. (2010), *Microstructure-sensitive extreme value probabilities of fatigue in advanced engineering alloys* (Ph.D. Thesis), Georgia Institute of Technology, Atlanta, GA.

Przybyla, C., Prasannavenkatesan, R., Salajegheh, N. and McDowell, D.L. (2010), "Microstructure-sensitive modeling of high cycle fatigue", *International Journal of Fatigue*, Vol. 32, pp. 512–525.

Przybyla, C.P. and McDowell, D.L. (2010), "Microstructure-sensitive extreme value probabilities for high cycle fatigue of Ni-base superalloy IN100", *International Journal of Plasticity*, Vol. 26, pp. 372–394.

Przybyla, C.P. and McDowell, D.L. (2011), "Simulated microstructure-sensitive extreme value probabilities for high cycle fatigue of duplex Ti–6Al–4V", *International Journal of Plasticity*, Vol. 27, pp. 1871–1895.

Przybyla, C.P., Musinski, W.D., Castelluccio, G.M. and McDowell, D.L. (2012), "Microstructure-sensitive HCF and VHCF simulations", *International Journal of Fatigue*.

Qin, Q. and Bassani, J.L. (1992), "Non-schmid yield behavior in single crystals", *Journal of the Mechanics and Physics of Solids*, Vol. 40 No. 4, pp. 813–833.

Reed, R.P., Smith, J.H. and Christ, B.W. (1983), *Economic Effects of Fracture in the United States. Part 1. a Synopsis of the September 30, 1982 Report to Nbs by Battelle Columbus Laboratories* (No. DOE/ER/10741-T1-Pt.1; NBS-SP-647-1), National Measurement Lab., Washington, DC (USA). Center for Materials Science.

Rice, J.R. (1968), "A Path Independent Integral and the Approximate Analysis of Strain Concentration by Notches and Cracks", *Journal of Applied Mechanics*, Vol. 35, pp. 379–386.

Roters, F., Eisenlohr, P., Hantcherli, L., Tjahjanto, D.D., Bieler, T.R. and Raabe, D. (2010), "Overview of constitutive laws, kinematics, homogenization and multiscale methods in crystal plasticity finite-element modeling: Theory, experiments, applications", *Acta Materialia*, Vol. 58 No. 4, pp. 1152–1211.

Salem, A.A., Kalidindi, S.R. and Semiatin, S.L. (2005), "Strain hardening due to deformation twinning in α-titanium: Constitutive relations and crystal-plasticity modeling", *Acta Materialia*, Vol. 53 No. 12, pp. 3495–3502.

Shechtman, D. and Eylon, D. (1978), "On the unstable shear in fatigued β-annealed Ti-11 and IMI-685 alloys", *Metallurgical Transactions A*, Vol. 9 No. 7, pp. 1018–1020.

Shenoy, M., Zhang, J. and McDowell, D.L. (2007), "Estimating fatigue sensitivity to polycrystalline Ni-base superalloy microstructures using a computational approach", *Fatigue & Fracture of Engineering Materials & Structures*, Vol. 30 No. 10, pp. 889–904.

Simmons, G. and Wang, H. (1971), *Single crystal elastic constants and calculated aggregate properties: a handbook*, M.I.T. Press, Cambridge, Mass.

Sinha, V., Mills, M.J., Williams, J.C. and Spowart, J.E. (2006), "Observations on the faceted initiation site in the dwell-fatigue tested ti-6242 alloy: Crystallographic orientation and size effects", *Metallurgical and Materials Transactions A*, Vol. 37 No. 5, pp. 1507–1518.

Smith, R., Watson, P. and Topper, T. (1970), "A stress strain parameter for the fatigue of materials", *Journal of Fatigue*, Vol. 5, pp. 767–778.

Stephens, R.I., Fatemi, A., Stephens, R.R. and Fuchs, H.O. (2000), *Metal Fatigue in Engineering*, Wiley.

Stubbington, C.A. and Bowen, A.W. (1974), "Improvements in the fatigue strength of Ti-6Al-4V through microstructure control", *Journal of Materials Science*, Vol. 9 No. 6, pp. 941–947.

Suresh, S. (1992), *Fatigue of materials*, Cambridge University Press, Cambridge, England.

Suri, S., Viswanathan, G.B., Neeraj, T., Hou, D.H. and Mills, M.J. (1998), "Room temperature deformation and mechanisms of slip transmission in oriented single-colony crystals of an α/β titanium alloy", *Acta Materialia*, Vol. 47, pp. 1019–1034.

Tanaka, K. and Akiniwa, Y. (1989), "Propagation and non-propagation of small fatigue cracks", *Advances in Fracture Mechanics, Proceedings ICF7*, Houston, TX, Vol. 2, pp. 869–887.

Thompson, N., Wadsworth, N. and Louat, N. (1956), "The origin of fatigue fracture in copper", *Philosophical Magazine*, Vol. 1 No. 2, pp. 113–126.

Torquato, S. (2002), *Random heterogeneous materials : microstructure and macroscopic properties*, Springer, New York :

Uta, E., Gey, N., Bocher, P., Humbert, M. and Gilgert, J. (2009), "Texture heterogeneities in αp/αs titanium forging analysed by EBSD-Relation to fatigue crack propagation", *Journal of Microscopy*, Vol. 233 No. 3, pp. 451–459.

Varshni, Y.P. (1970), "Temperature Dependence of the Elastic Constants", *Physical Review B*, Vol. 2 No. 10, pp. 3952–3958.

Venkataramani, G., Deka, D. and Ghosh, S. (2006), "Crystal Plasticity Based Fe Model for Understanding Microstructural Effects on Creep and Dwell Fatigue Ti-6242", *Journal of Engineering Materials and Technology*, Transactions of the ASME, Vol. 128, pp. 356–365.

Weibull, W. (1939), "A statistical theory of the strength of materials", *Proceedings 151*, Presented at the Royal Swedish Academy of Engineering Sciences, Stockholm.

Welsch, G., Boyer, R. and Collings, E.W. (1994), *Materials properties handbook: titanium alloys*, ASM International, Materials Park, OH.

Westergaard, H.M. (1939), "Bearing Pressures and Cracks", *Journal of Applied Mechanics*, Vol. 6, pp. 49–53.

Williams, J.C., Baggerly, R.G. and Paton, N.E. (2002), "Deformation behavior of HCP Ti-Al alloy single crystals", *Metallurgical and Materials Transactions A*, Vol. 33 No. 13, pp. 837–850.

Williams, M.L. and Ellinger, G.A. (1953), "Investigation of Structural Failures of Welded Ships", *Welding Journal*, Vol. 32 No. 10.

Wöhler, A. (1860), "Versuche über die Festigkeit der Eisenbahnwagenachsen", *Zeitschrift für Bauwesen*, Vol. 10, pp. 160–161.

Wojcik, C.C., Chan, K.S. and Koss, D.A. (1988), "Stage I fatigue crack propagation in a titanium alloy", *Acta Metallurgica*, Vol. 36 No. 5, pp. 1261–1270.

Woodfield, A.P., Gorman, M.D., Corderman, R.R., Sutliff, J.A. and Yamrom, B. (1995), "Effect of Microstructure on Dwell Fatigue Behavior of Ti-6242", *Proceedings of the Eighth World Conference on Titanium*, Presented at the Titanium '95: Science and Technology, The Institute of Materials, Birmingham, UK, Vol. 2, pp. 1116–1123.

Yoder, G., Cooley, L. and Crooker, T. (1977), "Observations on microstructurally sensitive fatigue crack growth in a widmanstätten Ti-6Al-4V alloy", *Metallurgical and Materials Transactions A*, Vol. 8 No. 11, pp. 1737–1743.

Yoder, G. and Eylon, D. (1979), "On the effect of colony size on fatigue crack growth in Widmanstätten structure α+β titanium alloys", *Metallurgical and Materials Transactions A*, Vol. 10 No. 11, pp. 1808–1810.

Yoder, G.R., Cooley, L.A. and Crooker, T.W. (1980), "Observations on the Generality of the Grain-Size Effect on Fatigue Crack Growth in alpha + beta Titanium Alloys", *Titanium '80 Science and Technology*, Vol. 3, pp. 1865–1874.

Zapffe, C.A. and Worden, C.O. (1951), "Fractographic registrations of fatigue", *Transactions of the American Society for Metals*, Vol. 43, pp. 55–65.

Zhang, M. (2008), *Crystal plasticity modeling of Ti-6Al-4V alloy and its application in cyclic and fretting fatigue analysis* (Ph.D.), Georgia Institute of Technology, Atlanta, GA.

Zhang, M., Zhang, J. and McDowell, D.L. (2007), “Microstructure-based crystal plasticity modeling of cyclic deformation of Ti–6Al–4V”, *International Journal of Plasticity*, Vol. 23, pp. 1328–1348.